



HAL
open science

Experimental investigation for local structures of IVb transition metal elements in minerals and glasses formed under extreme conditions

Tsubasa Tobase

► **To cite this version:**

Tsubasa Tobase. Experimental investigation for local structures of IVb transition metal elements in minerals and glasses formed under extreme conditions. Earth Sciences. Université de Lorraine; Graduate School of Science and Technology (Kumamoto, Japon), 2018. English. NNT : 2018LORR0200 . tel-02001223

HAL Id: tel-02001223

<https://theses.hal.science/tel-02001223>

Submitted on 31 Jan 2019

HAL is a multi-disciplinary open access archive for the deposit and dissemination of scientific research documents, whether they are published or not. The documents may come from teaching and research institutions in France or abroad, or from public or private research centers.

L'archive ouverte pluridisciplinaire **HAL**, est destinée au dépôt et à la diffusion de documents scientifiques de niveau recherche, publiés ou non, émanant des établissements d'enseignement et de recherche français ou étrangers, des laboratoires publics ou privés.



AVERTISSEMENT

Ce document est le fruit d'un long travail approuvé par le jury de soutenance et mis à disposition de l'ensemble de la communauté universitaire élargie.

Il est soumis à la propriété intellectuelle de l'auteur. Ceci implique une obligation de citation et de référencement lors de l'utilisation de ce document.

D'autre part, toute contrefaçon, plagiat, reproduction illicite encourt une poursuite pénale.

Contact : ddoc-theses-contact@univ-lorraine.fr

LIENS

Code de la Propriété Intellectuelle. articles L 122. 4

Code de la Propriété Intellectuelle. articles L 335.2- L 335.10

http://www.cfcopies.com/V2/leg/leg_droi.php

<http://www.culture.gouv.fr/culture/infos-pratiques/droits/protection.htm>



UNIVERSITÉ
DE LORRAINE



C2MP



Experimental investigation for local structures of IVb transition metal elements in minerals and glasses formed under extreme conditions

Doctral Thesis

To btain the degree of doctor in Earth Sciences from Kumamoto University
on the authority of the Dean of the Graduate School of Science and Technology, professor Jun Otani

and to obtain the degree of doctor in Chemistry from Université de Lorraine
on the authority of the President, professor Pierre Mutzenhardt

to be defended in public on Wednesday, December 19, 2018 at 16:00

by Tsubasa Tobase

born on December 28, 1989 in Amakusa (Japan)

Doctoral Thesis Committee

Prof. Dr. Akira Yoshiasa, Kumamoto University (supervisor)

Prof. Dr. Massimo Nespolo, Université de Lorraine (supervisor)

Prof. Dr. Mitsuo Machida, Sojo University (referee)

Prof. Dr. Takeshi Ikeda, Kyushu University (referee)



UNIVERSITÉ
DE LORRAINE



C2MP



Étude théorique et expérimentale de l'ordre à courte et longue distance dans les matériaux naturels désordonnés : minéraux et verres formés dans des conditions extrêmes

Thèse de doctorat

en vue de l'obtention du titre de docteur en Sciences de la Terre de l'Université de Kumamoto
sous l'autorité du doyen de l'école doctorale de Sciences et Technologies,
professeur Jun Otani

et en vue de l'obtention du titre de docteur en Chimie de l'Université de Lorraine
sous l'autorité du Président, professeur Pierre Mutzenhardt

soutenance publique le mercredi 19 décembre 19, 2018 à 16h00

par Tsubasa Tobase

né le 28 décembre 1989 à Amakusa (Japon)

Jury

Prof. Dr. Akira Yoshiasa, Kumamoto University (directeur de thèse)

Prof. Dr. Massimo Nespolo, Université de Lorraine (co-directeur de thèse)

Prof. Dr. Mitsuo Machida, Sojo University (rapporteur)

Prof. Dr. Takeshi Ikeda, Kyushu University (rapporteur)

Abstract

Elucidation of the formation mechanism of various natural glasses can help to understand the dynamics of the Earth because these materials record the formation condition in their structures. However, glasses are amorphous materials which cannot be studied by the diffraction techniques used for crystalline materials. Indirect information can be obtained by spectroscopic methods revealing the average coordination environment of metal atoms, which are known as local structures. In particular, X-ray absorption fine structure (XAFS) method is powerful tool to investigate the local structure of amorphous materials and the microcrystalline materials co-existing with meteoric glass; from the information it provides, it is possible to estimate the impact conditions.

In this Ph.D thesis, the local structure analysis of IVb transition metal elements (Ti, Zr) in natural minerals and glasses was performed by K-edge X-ray absorption near edge structure (XANES) and extended X-ray absorption fine structure (EXAFS). High temperature laser heating and gas flow experiments on zircon were also performed to observe structural changes at high temperature in the crystalline phases that accompany the meteoric glass.

Our previous research of Zr local structure analysis in meteorite impact-related glasses has shown that the local structure of Zr in these materials is similar to that of Zr in K-Pg sediments (sediments from the Cretaceous–Paleogene boundary). The latter does not show any influence from diagenesis and weathering, which suggests that K-Pg sediments maintains the thermal quenching history of the meteorite impact. The local structure analysis of Zr may therefore become a key factor for checking the possibility of the meteorite impact in sedimentary rock. However, abundance of Zr in sediments is not always sufficient to obtain reliable information about the local structure of Zr. The higher Clarke of titanium, which belongs to the same group as Zr, makes it a more likely marker in sedimentary rocks. Based on the local structure similarities of local structure of Ti in K-Pg sediments and that in impact glass, that in K-Pg sediments also maintains the glass-like local structure formed by meteorite impact. Consequently, the local structure analysis of Ti may also become a key factor to evaluate meteorite impact events. Combination of the information about the local structures of Ti and Zr allows a higher reliability for the estimation of meteorite impact event.

Local structure analysis of Zr in Martian meteorite of Tissint shows that local structure of Zr in the fusion crust of this meteorite is similar to that in tektite and accompanying impact glass; on the other hand, the local structure in the inner glassy part of Tissint is similar to that in baddeleyite and fulgurite. Based on the formation temperature of fulgurite and the $\text{ZrO}_2\text{-SiO}_2$ phase diagram, the formation temperature of the inner glass part of Tissint is estimated to be 1680-2000 °C. Since local structure of fusion crust is similar to that in tektite and in impact glass, we conclude that the baddeleyite-like part of Tissint was vitrified to glass-like part during the passage through the atmosphere. This comparison suggests that the condition of meteorite impact on Mars and the passage of meteorites through the atmosphere can be estimated through the analysis of the local structure of Zr in the glass part of meteorites, such as fusion crust and inner glass part.

In order to confirm structural change of Zr at high temperature, heating experiments of zircon were performed by gas flow and laser heating. During heating, powder X-ray diffraction experiment was performed for ZrSiO_4 and ZrO_2 to confirm their structure changes. Before phase transition of ZrO_2 from tetragonal to cubic, precursor phenomena were observed above around 2200 °C. Chemical composition analysis of quenched sample performed in SEM confirmed the evaporation of the SiO_2 component because of the existence of a SiO_2 -rich region around rim nearest the surface of the sample at temperatures above 2230 °C. On the other hand, the liquid-immiscible region proposed by Buttermann and Foster (1967) was not observed in the sample quenched from temperature range of 2250-2450 °C. Local structural analysis of zircon quenched from high temperature shows energy shifts of main peak position of XANES spectrum.

In order to confirm the detailed changes of XANES spectrum, middle temperature XAFS experiments are performed. We propose that quantitative comparisons for the XANES spectra can be investigated by using the absorption intensity invariant point normalization. There are two types of temperature dependence of pre-edge peak intensity; the rutile-type and the anatase-type. The true temperature dependence of transition to each orbit is obtained from the difference spectrum. Investigation of pre-edge intensity can provide detailed structure information such as the thermal vibration by middle temperature XAFS experiment.

XAFS applied to natural meteorite related glasses provides information about the local structural changes in Zr and Ti. By performing high-accuracy XAFS analyses for

transition elements and their local structure in sedimentary rocks, in the glass phase of meteorites and in the meteorite impact-related glasses such as tektite and impact glass, information on the formation condition of these materials can be obtained.

Keywords: XAFS, XANES, meteorite impact, local structure, zirconium, titanium

Résumé

L'élucidation du mécanisme de formation de divers verres naturels peut aider à comprendre la dynamique de la Terre car ces matériaux retiennent l'état de formation dans leurs structures. Cependant, les verres sont des matériaux amorphes qui ne peuvent pas être étudiés par les techniques de diffraction utilisées pour les matériaux cristallins. Des informations indirectes peuvent être obtenues par des méthodes spectroscopiques révélant l'environnement de coordination moyen des atomes métalliques, appelés structures locales. En particulier, la spectroscopie d'absorption des Rayons X (XAFS) est un outil particulièrement adapté à l'étude de la structure locale des matériaux amorphes et des matériaux microcristallins coexistant avec le verre météoritique; les informations qu'elle fournit permet d'estimer les conditions d'impact.

Dans cette thèse, l'analyse de la structure locale d'éléments de transition (Ti, Zr) dans les minéraux et les verres naturels a été réalisée par la spectroscopie de structure près du front d'absorption de rayons X (XANES) et la spectroscopie d'absorption des rayons X structure fine d'absorption des rayons structure fine étendue (EXAFS). Des expériences de chauffage au laser à haute température et de flux gazeux sur zircon ont également été effectuées pour observer les changements structuraux à haute température dans les phases cristallines qui accompagnent le verre météoritique.

Nos recherches antérieures sur l'analyse de la structure locale du Zr dans les matériaux naturels issus d'impacts de météorites ont montré que la structure locale de ces matériaux est semblable à celle du Zr dans les sédiments K-Pg (sédiments de la limite Crétacé – Paléogène). Ce dernier ne montre aucune influence de diagenèse ou d'altération, ce qui suggère que les sédiments K-Pg conservent trace de l'histoire de la trempe thermique provenant de l'impact de la météorite. L'analyse de la structure locale du Zr peut ainsi devenir un facteur clé pour vérifier la possibilité de l'impact de météorites sur les roches sédimentaires. Cependant, l'abondance de Zr dans les sédiments n'est pas toujours suffisante pour obtenir des informations fiables sur la structure locale du Zr. Le plus haut Clarke du titane, qui appartient au même groupe que le Zr, en fait un marqueur plus probable dans les roches sédimentaires. Sur la base des similitudes de structure locale dans les sédiments K-Pg et dans le verre d'impact, nous suggérons que la structure locale de Ti dans les sédiments de K-Pg retient également la structure locale typique du verre formée par l'impact des météorites. Par conséquent, l'analyse de la structure locale de Ti peut également devenir un facteur clé pour évaluer

les événements d'impact météoritiques. La combinaison des informations sur les structures locales du Ti et du Zr permet ainsi une plus grande fiabilité pour l'estimation de l'impact météoritique.

L'analyse de la structure locale du Zr dans la météorite martienne de Tissint montre que la structure locale du Zr dans la croûte de fusion de cette météorite est semblable à celle des tectites et du verre d'impact qui les accompagne; d'autre part, la structure locale dans la partie intérieure vitreuse de Tissint est similaire à celle de la baddeleyite et de la fulgurite. Sur la base de la température de formation de la fulgurite et du diagramme de phase ZrO_2-SiO_2 , la température de formation de la partie intérieure en verre de Tissint est estimée à 1680-2000°C. Puisque la structure locale de la croûte de fusion est semblable à celle des tectites et du verre d'impact, nous concluons que la partie de la météorite de Tissint qui est proche de la baddeleyite a subi une vitrification pendant le passage à travers l'atmosphère. Cette comparaison suggère que les conditions d'impact des météorites sur Mars et du passage des météorites à travers l'atmosphère peuvent être estimées par l'analyse de la structure locale de Zr dans la partie vitrifiée des météorites, tels que la croûte de fusion et de la partie intérieure en verre.

Afin de confirmer le changement structurel de Zr à haute température, des expériences de chauffage du zircon ont été effectuées sous un flux de gaz et par chauffage au laser. Pendant le chauffage, une expérience de diffraction des rayons X sur poudre a été effectuée sur $ZrSiO_4$ et ZrO_2 pour confirmer leurs changements de structure. Avant la transition de phase de ZrO_2 de tétragonale à cubique, des phénomènes précurseurs ont été observés au-dessus d'environ 2200°C. L'analyse chimique dans le MEB de la composition de l'échantillon trempé a confirmé l'évaporation de la composante SiO_2 comme montré par l'existence d'une région riche en SiO_2 autour de la bordure la plus proche de la surface de l'échantillon à des températures supérieures à 2230°C. D'autre part, la région d'immiscibilité liquide proposée par Buttier et Foster (1967) n'a pas été confirmée dans l'échantillon trempé dans un intervalle de température allant de 2250 à 2450°C. L'analyse de la structure locale du zircon trempé de haute température montre des changements d'énergie de la position du pic principal du spectre XANES.

Afin de confirmer les changements fins du spectre XANES, des expériences XAFS à température moyenne ont enfin été effectuées. Nous proposons que des comparaisons

quantitatives des spectres XANES puissent être effectuées à l'aide de la normalisation du point invariant d'intensité d'absorption. Il y a deux types de dépendance de température de l'intensité de pic « pre-edge »; le type rutile et le type anatase. La véritable dépendance de la température de transition sur chaque orbite est obtenue à partir du spectre différence. L'étude de l'intensité « pre-edge » peut fournir des informations détaillées sur la structure, telles que la vibration thermique par des expérience XAFS de température moyenne.

La technique XAFS appliquée aux matériaux amorphes issue des météorites fournit des informations sur les changements structuraux locaux du Zr et du Ti. En effectuant des analyses XAFS de haute précision pour les éléments trace et leur structure locale dans les roches sédimentaires, dans la phase de verre des météorites et dans les verres issus de l'impact météoritiques telles que les tectites et le verre d'impact, des informations sur les conditions de formation des ces matériaux peuvent être obtenues.

Mots-clès: XAFS, XANES, impact météoritique, structure locale, zirconium, titanium

Contents

Abstract

Chapter 1 General Introduction 11

- 1.1. Natural glasses
- 1.2. Impact events
- 1.3. Importance for study of impact glasses
- 1.4. Necessity of study for the amorphous component of K-Pg boundary sediments
- 1.5. Meteorite related materials
- 1.6. X-ray absorption fine structure as a method to quantitatively analyze amorphous phases
- 1.7. Local structures of Zr
- 1.8. Motivation of this study and outline

Chapter 2 Experiment of XAFS 35

- 2.1. X-ray Absorption Fine Structure (XAFS)
- 2.2. Experimental arrangement

Chapter 3 Local structures of Zr in K-Pg boundary sediments 46

- 3.1 Introduction
- 3.2 Sample and experiments
- 3.3 Results and discussion

Chapter 4 Local structures of Zr in K-Pg boundary sediments 52

- 4.1. Introduction
- 4.2. Sample
- 4.3. Results
- 4.4. Discussion

Chapter 5 Local structures of Ca, Fe, Ti and Zr in Fusion crust of Tissint meteorite 64

- 5.1. Introduction
- 5.2. Sample
- 5.3. Results and discussion

Chapter 6 High temperature diffraction experiments and phase diagram in the system ZrO_2-SiO_2

73

6.1. Introduction

6.2. Samples and Experiments

6.3. Results and Discussion

Chapter 7 Temperature dependence pre-edge peak intensities in XANES spectra

88

7.1. Introduction

7.2. Experimental methods

7.3. Results and Discussion

Chapter 8 General Conclusions

101

Chapter 1
General Introduction

1. 1. NATURAL GLASSES

Natural glasses are produced by Earth's activity and classified by their formation processes such as volcanic activity, lightning, crustal deformation and meteorite impact.

1.1.1. Volcanic glasses

Volcanic glasses such as obsidian, pitch stone and perlite are produced by rapid cooling of magma and classified by formation process or chemical composition. Obsidian, which is produced by rapid cooling of felsic magma, is commonly found within the margins of rhyolitic lava flows known as obsidian flows (Fink, 1983; Tuffen et al., 2013). Perlite has relatively high water content and is formed by the hydration of obsidian (Ross and Smith, 1955; Friedman et al., 1966; Lofgren, 1971). Pitchstone is coarser than obsidian; it is a volcanic rock with conchoidal fracture (like ordinary glass), a resinous luster and a variable composition. Water content of pitchstone is generally 4-10%, because of absorption from ocean and wet sediments (Dickin and Jones, 1983; Thorpe and Thorpe, 1984).

1.1.2. Fault rock

Pseudotachylite is a kind of fracture rock, which is closely related to fault system in crust. It is mainly produced by two types of geological events: one is impact event (Reimold, 1995), the other seismic shock (Prices et al., 2012). It is generally considered it forms by frictional melting of parent rock, which is caused by high speed fault movement (displacement).

1.1.3. Fulgurite

Fulgurite is formed by lightning strikes on the rocks which undergo melting (Sheffer et al., 2006; Saikia et al., 2008; Elizabeth et al., 2010). Fulgurite has experienced ultra-high temperature in short time and rapid cooling. Saikia et al. (2008) estimated the formation temperature of fulgurite to be in the range of 1600-2000 °C.

1. 2. IMPACT EVENTS

An impact event is the collision of an asteroid, comet or other celestial object with a planet (Alvarez et al., 1980). As a meteoroid impacts the Earth's surface, because of super velocity and temperature attained, parts of the targets are melted instantly, and then splatter around the crater or splash to outer space, where they finally solidify and fall back to the Earth; this series of processes is what formed tektites. The impact theory proclaims that tektites are derived from meteorite impact event (Glass, 1984; Chao, 1993; Koeberl, 1986).

1.2.1. Tektites

Most tektites are several centimeters in diameter and are black, brownish or grey in color. Tektites are hundred times lower in moisture content than volcanic glasses (Beran and Koeberl, 1997). Tektites are found over wide areas. Four strewn fields (figure 1.1) are known: the European strewn field (Nördlinger Ries impact crater, Germany; age: 15 million years), the Australian strewn field (no associated crater identified; age: 0.77-0.78 million years), the North American strewn field (Chesapeake Bay impact crater, USA; age: 34 million years), and the Ivory Coast strewn field (Lake Bosumtwi impact crater, Ghana; age: 1 million years).

Tektites can be classified by structure and shape into 4 categories: Muong Nong, or layered tektite; microtektites, glassy or crystalline bodies less than 1 mm in diameter; splash-form tektites, including spheres, ellipsoids, tori, and dumbbells; and ablated tektites. Splash-form tektite is the most common one. Tektites were formed by meteorite impact on rocks and sand at the surface of the Earth; the melted rocks and soils and the meteorite bodies were ejected to the sky and the impact melt eventually quenched during flying (Glass 1984, 1990; Koeberl, 1986, 1990; Chao, 1993). Analyzed statistic data (Stauffer and Butler, 2010), hypotheses (Reinhart, 1985) and laboratory model experiments (Elkins-tanton et al., 2003) suggested that the size and shape are controlled by flying route, surface tension and rotational speed of tektite's body.



Figure 1.1. Location of the sampling site and crater site.

1.2.2 Impact glasses

Impact glasses are defined as the glass produced by meteorite impact. Suevite, köfelsite, Darwin glass and Libyan dessert glass (LDG) are considered impact glasses; they are found in the craters and are affected by a momentary high temperature and high pressure (Brett, 1967; Stähle, 1972; Störzer, 1971; Bogard et al., 1988; Engelhardt, 1997; El Goresy et al., 2001; Osinski et al., 2004; Medkeff and Rundkvist, 2008).

1. 3. IMPORTANCE OF THE STUDY OF IMPACT GLASSES

The elucidation of the formation mechanism of various natural glasses can contribute to understand the dynamics of the Earth (Koeberl et al., 1986; Engelhardt et al., 1987; Izett et al., 1991; Engelhardt, 1997; Artemieva et al., 2002; Howard, 2011). The literature on the subject show that the atomic coordination environments in natural glass can be exploited as a record of the formation conditions (Stebbins and McMillan, 1989; Paris et al., 1994; Mysen and Neuville, 1995; Yarger et al., 1995). A link can therefore presumably be established between the local structures of natural glasses and the events that have characterized the history of our planet.

The glass materials formed by meteorite impact on the Earth are termed

impact-related glasses and classified by the formation process and location. Impact glasses and tektites were described in section 1.2. Several studies have been performed to estimate the meteorite impact conditions from impact-related glasses; however, accurate interatomic distances and coordination numbers like those obtained for crystalline materials by conventional X-ray diffraction or neutron diffraction are not available because of the amorphous nature of glass; only an indirect estimation of the average distance can be obtained (McPherson et al., 1984; Wright et al., 1984). By exploiting the local structure information of microcrystalline materials formed by impact and accompanying the bulky glass, as well as local structural information about the amorphous materials, we believe that it is possible to estimate the meteorite impact conditions.

1. 4. NECESSITY OF STUDYING OF THE AMORPHOUS COMPONENT OF K-PG BOUNDARY SEDIMENTS

Cretaceous-Paleogene (K-Pg) boundary is the boundary between Cretaceous and Paleogene periods. During five major extinction events occurred until 65 million years ago (Ma) in the Earth's history, 60-90% of terrestrial and marine organism such as dinosaurs and ammonites have been extinct (Raup and Sepkoski 1982). Alvarez et al. (1980) proposed that K-Pg mass extinction was due to global environmental change following meteorite impacts, using as evidence, the abnormal concentration of Ir in Stevns Klint, Denmark, and Gubbio, Italy. Boher et al. (1987) and Kring and Boynton (1991) reported that meteorite impact related materials such as shocked quartz, tektites and spherules were found from the K-Pg boundary layer around the world. In addition, since Chicxulub crater was discovered in Yucatan Peninsula, North East part of Mexico, meteorite impact theory is supported by many researchers (Hildebrand et al., 1991; Sigurdsson et al., 1991a, b; Swisher et al., 1992; Izett 1991; Sharpton et al., 1992; Dalrymple et al, 1993; Blum et al., 1993; Koeberl et al., 1994). Moreover, additional information on evidence for meteorite impact such as chemical composition and inclusion of sedimentary rocks strengthening the hypothesis of an impact event would

come from the local structures of the non-crystalline materials, which would certainly be affected as well by such an impact. The investigation of non-crystalline components in the K-Pg boundary sediments is expected to help elucidating the causes of mass extinction and the environments left after a meteorite impact (Izett, 1991; Kring and Boynton, 1991; Sigurdsson et al., 1991a, b; Koeberl, 1992; Koeberl and Sigurdsson, 1992; Martínez-Ruiz et al., 2001; Belza et al., 2015). Statistical analysis suggests a strong correlation between the scale of meteorite impact, which is estimated from the size of Chicxulub crater, and K-Pg mass extinction (White and Saunders, 2005). In addition, the discovery of shocked-quartz from the K-Pg boundary sediments also strengthens the meteorite impact theory (Bohor et al., 1987). The crystalline phases in the boundary sediments have been the subject of a large number of studies (Bohor et al., 1984; Bohor et al., 1987; Martinez-Ruiz et al., 2001; Belza et al., 2017) and are widely used for dating and estimating the environments after meteorite impact (Bralower et al., 1998; Smit et al., 1992). Important information about the meteorite impact conditions and sedimentation conditions after meteorite impact can also be provided by non-crystalline materials, as it can be expected from the fact that they compose half of the soils or more (Rampino and Reynolds, 1983; Tsukimura and Nakazawa, 1994).

1. 5. METEORITE RELATED MATERIALS

SNC (shergottites, nahklites and chassignites) meteorites from Mars are a kind of achondrite. Achondrite is defined as a kind of stony meteorite which does not contain spherules. The first suggestions of SNC meteorites ejected from Mars by meteorite impact are based on the crystallization age of SNC meteorites. The duration of volcanic activity on a body is related to planetary size because large celestial bodies have low surface-to-volume ratios and so lose internal heat more slowly than small bodies. Volcanic activity on the SNC parent body demands that these meteorites were driven from a large planetary body (McSween et al., 1979; Walker et al., 1979; Wasson and Wetherill, 1979). As stronger evidence, the isotopic

composition of noble gas such as Ar in the meteorite impact-shocked glasses is in good agreement with that in the atmosphere of Mars (Bogard 1984; Becker and Pepin, 1984; Swindle et al., 1986; Wiens et al., 1988). The isotopic compositions and abundance of noble gases in melted-glass are shown figure 1.2. Furthermore, in order to accumulate crystals in the meteorite, the size of the celestial body needs to be larger than that of the moon (Grimm and McSween, 1982). Martian meteorites are classified as shergottites, nakhlites, chassignites and ALH84001 by their mineral inclusion (table 1.1-1.4). Previous studies have shown that the physico-chemical conditions of the planet Mars, such as Martian magma composition (Stolper and McSween, 1979; Treiman and Sutton, 1992 ; Longhi and Pan, 1987; Harvey and McSween, 1992) and the shock scale of meteorite impact on the surface of Mars (Stöffler et al., 1986, 1991; El Goresy et al., 1997; Head et al., 2002; Baziotis et al. 2013) can be estimated from SNC meteorites. In particular, mineral inclusions of shergottites give information about the shock scale. Tissint meteorite, which is the newest shergottite (Irving et al., 2012; Balta et al., 2013, 2015), contains very large ringwoodite grains ($75 \times 140 \mu\text{m}^2$), which is an indicator of the shock scale of meteorite impact (Baziotis et al., 2013). Mineral inclusions of Tissint meteorite have brought new clue to estimate the meteorite impact on Mars. In addition, Tissint meteorites are not affected by diagenesis because of the short timescale between their arrival on Earth and the analysis in laboratories.

During the passage through the atmosphere, fusion crusts are formed on the surface of meteorites. Fusion crust records useful information about the temperature and quenching conditions. The comparison between fusion crust and bulk of meteorite suggests that the bulk in low-temperature and high-pressure phase changed to fusion crust in high-temperature and low-pressure phase during passage in the atmosphere (Kimura et al., 2003). The sequence of events that occurred in the fusion crust of the meteorite is: (1) loss of and reaction of immiscible Fe-rich liquids, (2) mixing between substrate partial melts and bulk of melted crust, and (3) loss of volatile components by evaporation and degassing (Genge and Grady,

1999; Toppani et al., 2003; Genge, 2006; Thaisen and Taylor, 2009). The core and the fusion crust of the meteorite present a glass content. A number of studies have elucidated the environment of Mars from mineral inclusion of Martian meteorites. This knowledge can and should be complemented with information about the meteorite impact event and the conditions of passage in the atmosphere that can be obtained from glass phases.

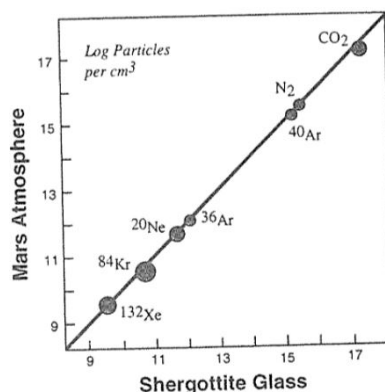


Figure 1.2. The abundance of N₂, CO₂ and various noble gas isotopes trapped in impact-melt glass from the EETA79001 shergottite match measurements of the Martian atmosphere by Viking spacecraft (modified from Pepin and Carr, 1992). Uncertainties in the analyses are encompassed within the circles.

Table 1.1-4. Representative mineral compositions in SNC meteorites. The following tables contain electron microprobe analyses of pyroxene (table 1.1), feldspars (or maskelynite) (table 1.2), olivines (table 1.3) and oxides (table 1.4) in basaltic and lherzolitic shergotties, nahklites, Chassigny and ALH84001. In table 1.1, Pig is pigeonite, Aug is augite, Opx is orthopyroxene. In table 1.2, Mask is maskelynite, Plag is plagioclase, Sanid is sanidine.

Table 1.1. Pyroxenes.

Shergottie				EETA79001			
Pig	Pig	Aug	Aug	Pig	Pig	Aug	Aug
Core	Rim	Core	Rim	Core	Rim	Core	Rim

	Smith & Hervig (1979)				McSween & Jarosewich (1983)			
SiO ₂	54.6	49.7	53.6	50.5	53.8	49.9	52.1	50.7
Al ₂ O ₃	0.74	0.66	0.96	0.87	0.70	0.83	1.50	1.21
TiO ₂	0.08	0.40	0.20	0.52	0.11	0.59	0.26	0.66
Cr ₂ O ₃	0.43	0.10	0.70	0.17	0.45	0.27	0.62	0.44
FeO	16.9	31.1	11.9	25.8	16.7	27.5	15.0	16.9
MnO	0.53	0.78	0.41	0.68	0.63	0.84	0.52	0.59
MgO	21.8	11.0	16.9	9.62	23.0	12.6	17.6	13.6
CaO	6.11	6.64	16.7	12.2	4.38	7.41	11.8	14.5
Na ₂ O	0.07	0.09	0.15	0.11	0.08	0.11	0.20	0.19
Total	101.28	100.3	101.42	100.51	99.85	100.05	99.60	98.79

Table 1.1. Pyroxenes.

	Nakhla			Chassigny			ALH84001	
	Pig	Aug Core	Aug Rim	Aug	Pig	Opx	Aug	Opx
	Treiman (1989)			Wadhula & Crozaz (1996)			Treiman (1995)	
SiO ₂	49.64	52.68	49.82	53.11	53.74	53.50	53.72	54.41
Al ₂ O ₃	0.69	1.03	1.45	1.03	0.61	0.72	0.56	0.56
TiO ₂	0.37	0.34	0.44	0.28	0.14	0.19	0.30	0.18
Cr ₂ O ₃	0.01	0.47	0.03	0.77	0.41	0.30	0.49	0.29
FeO	36.17	14.18	25.57	9.33	15.90	17.89	7.48	17.50
MnO	1.03	0.44	0.71	0.34	0.50	0.59	0.27	0.51
MgO	7.73	12.97	7.27	16.71	22.98	24.35	15.94	25.59
CaO	5.15	18.35	14.86	17.87	5.21	1.87	21.01	1.52
Na ₂ O	0.12	0.22	0.23	0.32	0.11	0.05	0.37	0.02
Total	100.91	100.67	100.38	99.77	99.60	99.47	100.14	100.58

Table 1.2. Maskelynite and feldspar.

	EETA 79001		Nakhla	Chassigny		ALH84001
	Mask Core	Mask Rim	Plag	Plag	Sanid	Mask
	McSween & Jarosewich (1983)		Wineke (1978)	Floran et al., (1978)		Mittlefehl dt (1994)
SiO ₂	52.5	55.8	60.14	62.6	64.7	61.9
Al ₂ O ₃	29.8	27.5	23.78	24.1	20.5	24.7
FeO	0.72	0.61	0.92	0.51	0.61	0.29
MgO	nd	nd	0.06	nd	nd	0.05
CaO	12.7	10.5	6.44	6.3	0.95	6.29
Na ₂ O	4.38	5.16	7.37	7.0	5.0	7.07
K ₂ O	0.15	0.32	0.91	0.61	7.5	0.97
Total	100.25	99.89	99.62	101.1	99.17	101.27

Table 1.3. Olivine.

	EETA 79001	Nakhla	Chassigny
	McSween & Jarosewich (1983)	Treiman (1993)	Floran et al., (1978)
SiO ₂	38.3	33.46	37.1
Al ₂ O ₃	0.02	0.05	0.08
FeO	24.0	48.42	27.6
MgO	36.8	17.36	34.0
MnO	0.55	0.95	0.53
Cr ₂ O ₃	0.07	0.02	0.04
CaO	0.26	0.37	0.19
Total	100.00	100.63	99.54

Table 1.4. Oxides.

	EETA 79001			Nakhla		Chassigny		ALH84 001
	Ulvospi nel	Ilmeni te	Chromi te	Magnetit e	Ilmenite	Chro mite	Ilmenit e	Chromi te
	McSween & Jarosewich (1983)			Treiman (1993)	Boctor et al., (1978)	Floran et al., (1978)		Mittllef ehldt (1994)
TiO ₂	30.7	41.1	0.81	14.81	51.3	3.6	51.2	2.23
Al ₂ O ₃	1.72	0.19	7.11	6.83	0.24	6.6	0.70	8.53
Cr ₂ O ₃	0.04	0.34	57.8	0.34	0.12	45.8	0.29	47.7
FeO	67.0	45.4	32.3	75.0	44.56	37.3	39.6	36.0
MgO	0.26	1.76	2.35	0.48	0.86	3.8	5.5	3.85
MnO	0.66	0.74	0.53	0.41	0.62	0.61	1.56	0.39
Total	100.38	99.53	100.90	97.87	97.70	97.71	98.85	98.70

1. 6. X-RAY ABSORPTION FINE STRUCTURE AS A METHOD TO QUANTITATIVELY ANALYZE AMORPHOUS PHASES.

In crystalline materials, we can define a coordination polyhedron around each crystallographically independent (symmetry unrelated) atom or ion and assign to that atom or ion a coordination number, which corresponds to the number of chemical bonds it forms. For uniform polyhedra (i.e. polyhedra in which the centre-to-vertex distances are all identical) the coordination number is uniquely defined, whereas for non-uniform polyhedra, its definition becomes more ambiguous to the point that it has been called an “inorganic chameleon” (Hoppe, 1970) and a weighted average called the Effective Coordination Number, ECoN (Hoppe, 1979), has been introduced. The larger the difference between ECoN and the classical coordination number, the more distorted is the coordination polyhedron, a typical example being that of alkali metals. The structure solution obtained from an X-ray diffraction (XRD) pattern gives the individual bond distances, from which the (effective)

coordination number is easily computed. Due to the nature of the radiation-matter interaction itself, the result is a space-average over the sample volume.

Each element in non-crystalline materials and glasses has a specific local coordination environments according to the atomic size, chemical bonding characters and formation conditions. A specific element has a specific average bond distance to the first nearest neighbours and an average coordination number. The average coordination number decreases with temperature and increases with pressure.

A meteorite impact develops instantaneously high temperature and high pressure conditions under which the crystallinity of the minerals is destroyed and the result is non-crystalline material which can be compared to natural glasses, normally formed by rapid cooling from high temperature, rather than by a sudden energy release due to a shock. In both cases, the regular and periodic arrangement typical of a crystalline structure is missing, the XRD pattern does not present sharp Bragg peaks and the information on the individual bond distances is not easily accessible. X-ray absorption fine structure (XAFS) spectroscopy is an ideal technique for disordered structures and can distinguish different chemical environments (atomic species and oxidation states around the emitted photoelectron). The transition from a core-level to an unoccupied orbital or band reflects the electronic unoccupied state. (Inverse) Fourier Transform of the XAFS amplitude provides information about the average bonding distance, this average being dominated by the local and dynamic behavior of the interaction. In case of high symmetry crystalline material, the result about the bond lengths obtained by XRD or XAFS should be identical within error. When the same chemical type of atom occupies different polyhedra, the information brought by the XAFS spectra is an average over these. By comparison of XAFS spectra of crystalline and non-crystalline materials containing the same atoms, we can assign a likely average coordination number in the non-crystalline materials based on the similarity of average bond distances with the crystalline phase, for which the coordination number is known. The result obtained in this way

makes sense if the coordination polyhedron in the crystalline phase is not too distorted: in other words, if the difference between ECoN and the classical coordination number is not too large. From the information about the coordination environments obtained by XAFS we will concentrate our attention to the average coordination number and the average bond distance around the atom undergoing the transition, hereafter termed the coordination environments of that atom.

The importance of investigation of glass phase has been described in the previous chapter. XAFS method is a powerful tool for investigation of non-crystalline materials. XAFS spectrum is divided into two regimes: XANES (X-ray absorption near edge structure) and EXAFS (extended X-ray absorption fine structure). Experimental XAFS analysis is described in chapter 2. Local structure analysis of several atoms in tektites, impact glasses and K-Pg boundary sediments have been performed to estimate the formation conditions related to meteorites (Guili et al., 2003, 2005, 2008; Sakai et al., 2007; Wang et al., 2011, 2013a, b; Okube et al., 2012, Tobase et al., 2013; Miyano et al., 2016; Hongu et al., submitted). Sakai et al. (2007) and Hongu et al. (submitted) reported that local structures of As and Sb in K-Pg sediments are similar to those in ferrihydrite-schwertmannite (figure 1.3 and 1.4), therefore As and Sb ions in K-Pg sediments are estimated to co-precipitate with Fe ion. This result is consistent with natural precipitation mechanism of As and Sb ions (Bigham et al., 1994). Main crystalline constituents of K-Pg sediments are smectite, quartz, goethite and calcite, as probed by XRD (figure 1.6). Local structures of Fe in K-Pg sediments is estimated to be similar to that in goethite based on the XRD investigation. However, Miyano et al. (2016) showed that local structures of Fe in K-Pg sediments is similar to those in schwertmannite, rather than that in goethite, and that in K-Pg sediments is intermediate between that in goethite and hematite (figure 1.5). Most of the information in XRD is about quartz because of the amount of SiO₂ in K-Pg sediments; therefore, we cannot obtain enough information of the Fe component in K-Pg sediments. On the other hand, XAFS analysis can provide more detailed information of Fe local structures. Therefore, XAFS

analysis for local structures of target atoms should be able to provide information about formation conditions of the sediments.

Figure 1.7 shows that XANES spectra of Ca in tektites and natural glasses. The shoulder features, which is located at 4 ± 1 eV before the first peak, in Ca XANES spectra are affected by SiO₂ content (Neuville et al., 2004). The pre-edge peak, which is located at 10 ± 1 eV before the first peak, gives information on the site geometry. Each Ca XANES spectrum of tektites has similar shape and differs from other natural glasses. Local structure analyses for Ca can be exploited to classify tektite and impact glass, based on characteristic Ca local structures in tektites (Tobase et al., 2013).

In Fe XANES spectra, peak position and threshold energy (figure 1.8a) are affected by the oxidation state of Fe atom (Okudera et al., 2012) and have positive correlation with Fe valence state. In order to evaluate Fe valence state from XANES, we use differentiation of XANES (dXANES) to provide detailed changes of peak position and threshold energy of XANES (figure 1.9b). From Fe XANES spectra (figure 1.9), the oxidation state of tektites and impact glasses can be estimated, as shown in table 1.5 (Guili et al., 2003, 2005; Wang et al., 2013b). Oxidation states of Fe ion in tektites were estimated to be 2-2.5 from the $\text{Fe}^{3+}/\Sigma \text{Fe}$ ratio of 0.04-0.13, as shown in figure 1.10 (Wang et al., 2013b). Wang et al. (2013b) proposed that tektites were quenched in the low oxidation state typical of high altitude of the Earth's atmosphere because the thresholded energy of Fe XANES spectra in all tektites are lower than those in volcanic glasses and impact glasses.

XANES spectra of Ti are sensitive to coordination environments, which are affected by the formation conditions (Farges et al., 1996a, b, c, 1997). Therefore, local structure analyses of Ti can provide information about the formation condition of each material. Tektites can be classified into groups by the shape of Ti XANES spectra (figure 1.11) (Wang et al., 2011, 2013a). Detailed comparison of local structures of Ti in moldavite-tektites showed difference in color and those in hainanite-tektite showed difference in analytical position; therefore, local structure analyses of Ti

revealed that local structures of Ti changes in detail by color and position of target material. On the basis of the valence state of Fe atoms, which is estimated by local structure analyses of Fe in yellow impact glasses obtained from K-Pg boundary sediments, the oxygen fugacity condition in melt formation can be estimated (Guili et al., 2008). Local structures of As, Zn, Fe, Ca, Ni and Mn in non-crystalline part of K-Pg sediments provide a clue to estimate the sediment environments (Sakai et al., 2007; Okube et al., 2012; Miyano et al., 2015). The results of previous studies of tektites, impact glasses and K-Pg sediments show that local structure analyses in glass phase reflects the formation conditions; therefore, local structure analyses in glass phase is an effective tool to estimate the formation conditions.

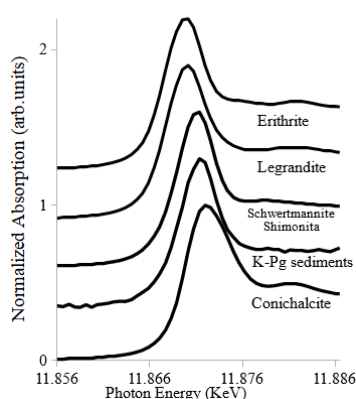


Figure 1.3. XANES spectra of As K-edge in K-Pg sediments and other reference (Sakai et al., 2007).

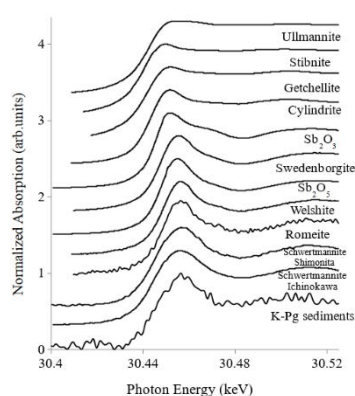


Figure 1.4. XANES spectra of Sb K-edge in K-Pg sediments (Hongu et al., unpublished data).

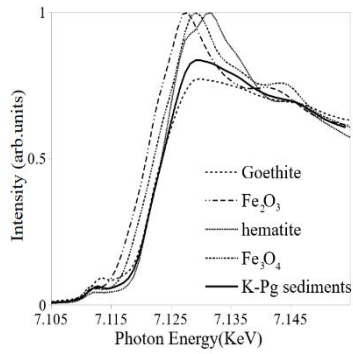


Figure 1.5. XANES spectra of Fe K-edge in K-Pg sediments (Miyano et al., 2016).

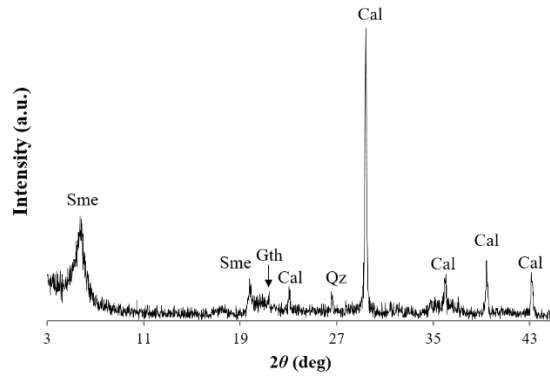
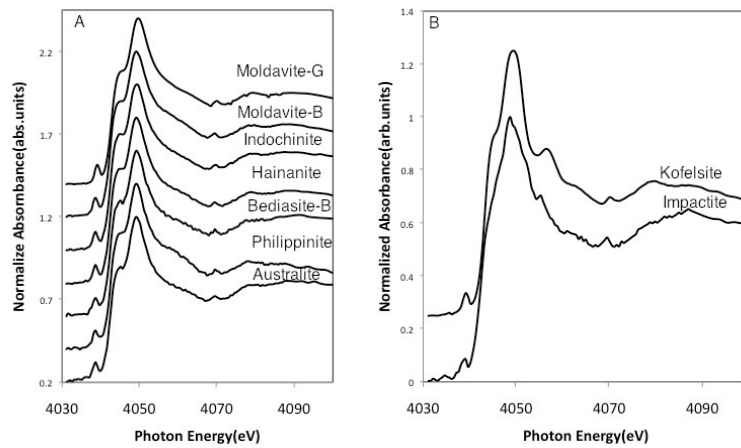


Figure 1.6. X-ray diffraction patterns of bulk part of K-Pg sediments. Cal, calcite; Qz, quartz; Gth, goethite; Sme, smectite.



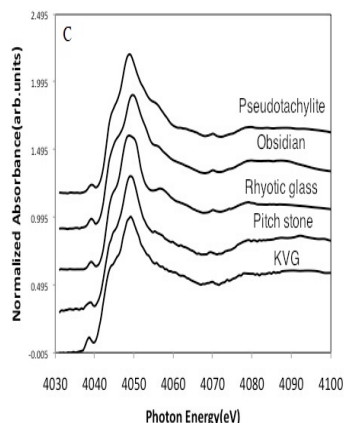


Figure 1.7. XANES spectra of Ca K-edge in tektites (A), impact glasses (B), volcanic glasses and pseudotachylite (C) (Tobase et al., 2013).

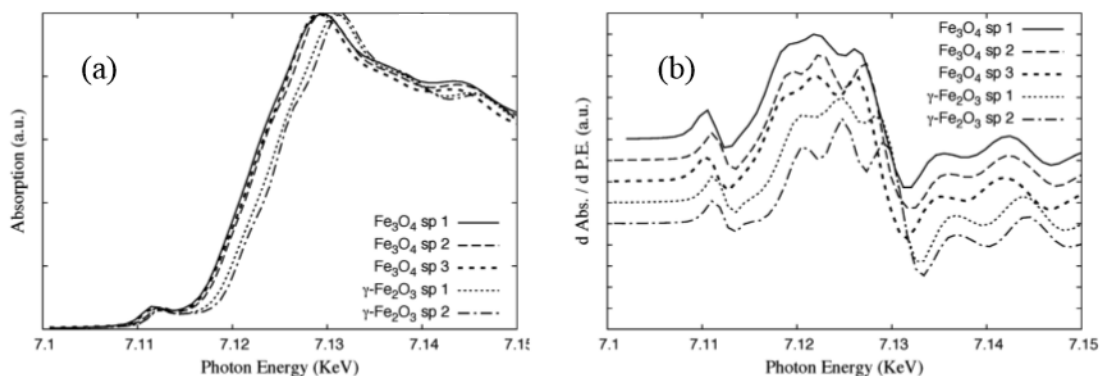


Figure 1.8. Experimental XANES spectra of Fe K-edge in various kind of Fe_3O_4 magnetite and $\gamma\text{-Fe}_2\text{O}_3$ maghemite (A), the differentiation of XANES spectra (dXANES) (B) (Okudera et al., 2012).

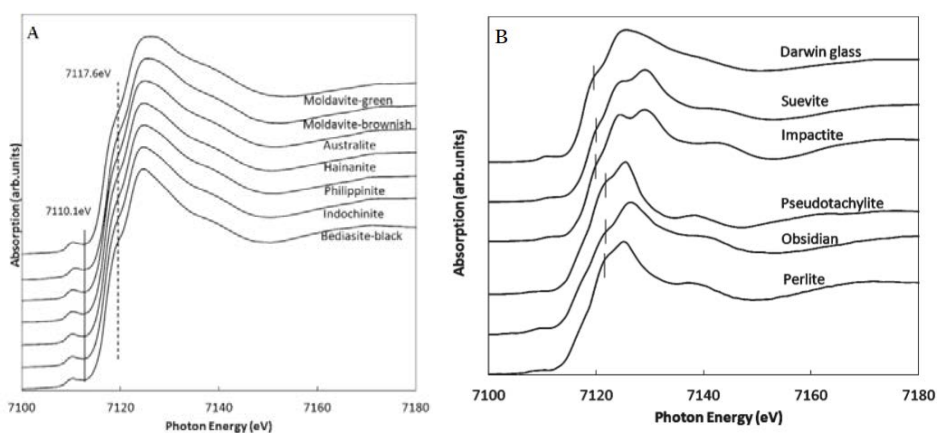


Figure 1.9. XANES spectra of Fe K-edge in tektites (A), impact glasses and volcanic glasses (B) (Wang et al., 2013b).

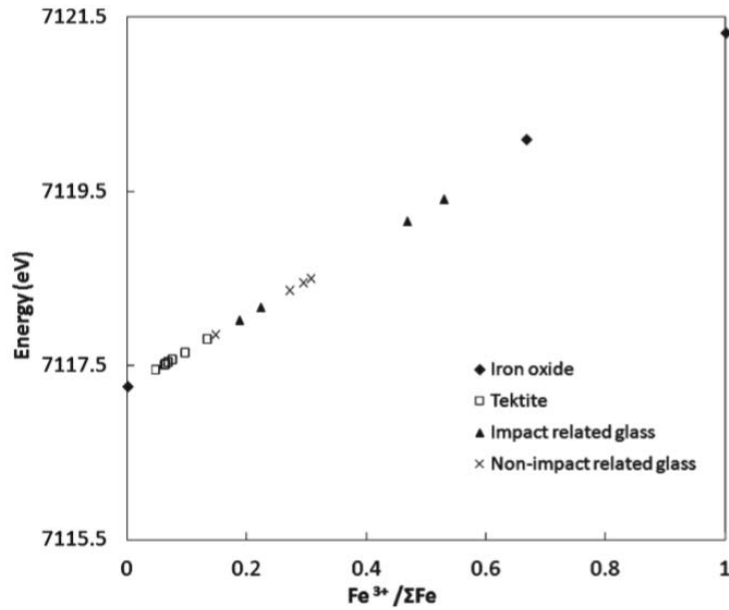


Figure 1.10. Correlation between $\text{Fe}^{3+}/\Sigma\text{Fe}$ (x) and threshold energy (y) represented by an equation $y=4.084x + 7117.299$ ($R^2=0.999$) (Wang et al., 2013b).

Table 1.5. Energies of fitted Fe K-edge XANES in tektites, impact glasses, and non-impact related glasses (Wang et al., 2013b).

Sample name		Energy (eV)			Estimated $\text{Fe}^{3+}/\Sigma\text{Fe}$ ratio
		Pre-edge	Threshold	Edge crest	
Tektite	Australite	7110.14(1)	7117.57(1)	7124.75(1)	0.06 (1)
	Moldavite-brownish	7111.00(1)	7117.81(0)	7125.61(1)	0.13 (1)
	Indochinite	7111.00(1)	7117.52(1)	7124.75(1)	0.05 (1)
	Moldavite-green	7110.14(1)	7117.46(1)	7125.61(1)	0.04 (1)
	Philippinite	7110.14(1)	7117.54(1)	7124.75(1)	0.06 (1)
	Bediasite-black	7110.14(1)	7117.66(1)	7124.75(1)	0.09 (1)
	Hainanite	7110.14(1)	7117.53(1)	7124.75(1)	0.06 (1)
Impact-related glass	Darwin glass-black	7111.00(1)	7118.17(1)	7125.61(1)	0.21 (1)
	Darwin glass-green	7111.00(1)	7118.03(1)	7125.61(1)	0.18 (1)
	Suevite	7110.14(1)	7119.42(1)	7129.05(1)	0.52 (1)
	Impactite	7110.14(1)	7119.17(1)	7129.05(1)	0.46 (1)
Non-impactrelated glass	Pseudotachylite	Shoulder	7118.46(1)	7125.61(1)	0.29 (1)
	Obsidian	7110.14(1)	7118.37(1)	7126.47(1)	0.26 (1)
	Perlite	7110.14(1)	7118.51(0)	7124.75(1)	0.30 (1)

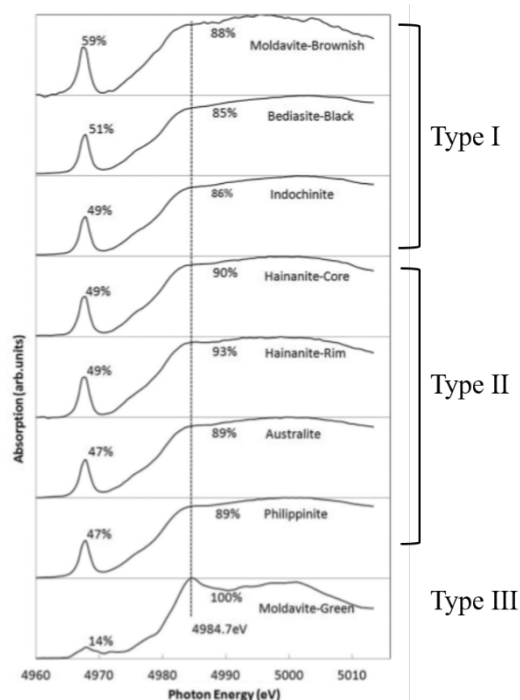


Figure 1.11. XANES spectra of Ti K-edge in tektites (Wang et al., 2011).

1.7. LOCAL STRUCTURES OF ZR

Zirconium is a typical high field strength element (HFSE). In petrology and geochemistry, incompatible elements are defined as those that are unsuitable in size and/or charge to fit the cation sites of the minerals in which they should be included. HFSE belongs to incompatible elements and have large ionic valence. Zircon ($ZrSiO_4$) is a well-known rock forming mineral containing zirconium, found as micro-crystals in igneous rocks. Zircon is the oldest mineral reported on Earth (Bowring and Priscoan, 1999; Froud et al., 1983; Compston and Pidgeon, 1986; Wilde and Pedgeon, 1990; Kober et al., 1989; Amelin, 1998; Amelin et al., 1999; Myers, 1995). Zircon records the changes due to temperature, pressure and shock in crystal structure (Butterman and Foster, 1967; Liu, 1979; Mashimo et al., 1983; Kusaba et al., 1983; Subbarao et al., 1990; Murgic et al., 1992; Kaiser et al., 2008; Yoshiasa et al., 2009) and is used for dating (Compston and Pidgeon 1986; Maas et al., 1991). Local structure analyses for Zr by XAFS method were performed by McKeown et al. (1999), Mountjoy et al. (2000), Okube et al. (2005) and Yoshiasa et

al. (2009). Main peak position of XANES spectra of Zr shows temperature and pressure dependence (Okube et al., 2005; Yoshiasa et al., 2009). Differences of local structures of Zr in each material appear in the shape of XANES spectra; local structures of Zr in glass materials also reflect thermal structure changes in the shape of XANES spectra (McKeown et al., 1999; Mountjoy et al., 2000). On the basis of the previous investigations, we know that local structure analyses of Zr in the crystalline as well as the glass phase can provide useful information to estimate the formation process and conditions of these phases.

In our master thesis, we performed local structure analyses of Zr in natural glasses such as tektites (australite, hainanite, indochinite, philippinite, moldavite-green and -brownish), impact glasses (köfelsite, Darwin glass, suevite and Libyan desert glass (LDG)), volcanic glasses (obsidian and pitchstone) and fulgurite (Tobase et al., 2015b) and we showed that local structures of Zr record information about the formation conditions in ancient times. Local structures of Zr in natural glasses were found to be different in XANES spectra, EXAFS spectra (figure 1.12) and Zr-O distance (table 1.5). Local structures of Zr in natural glasses were classified as SrZrO_3 -type, baddeleyite-type, zircon-type and glass-type, based on the similarity of XANES spectra. Similarity of XANES spectra was investigated by shape of first peak at 18.002 KeV and the second peak at 18.014 KeV. Zircon-type local structures of Zr were found in köfelsite and suevite. On the other hand, baddeleyite-type was found in fulgurite. Volcanic glasses were classified as SrZrO_3 -type. Zr XANES spectra of all of tektites were slightly different from SrZrO_3 -type, especially in shape of the second peak, on the basis of which tektites were classified as glass-type. Although shapes of the second peak of Zr XANES spectra of Darwin glass and LDG were similar to glass-type, these spectra only had pre-edge peak. Therefore, Darwin glass and LDG were classified as special glass-type. The formation temperature of natural glasses was estimated based on the phase diagram of ZrO_2 - SiO_2 proposed by Buttermann and Foster (1967) and Kaiser et al. (2008) (figure 1.13): formation temperature of zircon-type was below 1680 °C, that of baddeleyite-type was between 1680 and

2800 °C and that of glass-type was above 2800 °C. Formation temperature of glassy-suevite was estimated to be in the range of 900-1300 °C and 45-60 GPa by Engelhardt (1997). Local structures of Zr in suevite was of zircon-type, so that the formation temperature of suevite was estimated to be below 1680°C. This estimation by XAFS was consistent with that by Engelhardt (1997). On the other hand, formation temperature of köfelsite was estimated to be higher than 1680 °C (Storzer et al., 1971). According to Storzer et al. (1971), history of annealing is observed in rim of köfelsite. On the basis of similarity of local structures of Zr between köfelsite and zircon, we suggest that local structures of Zr in köfelsite changed to that in zircon-type by annealing. Estimation of formation temperature of suevite and köfelsite by Storzer et al. (1971) were consistent with the estimation from XAFS. Melosh and Ivanov (1999) proposed that tektites have experienced instantaneous ultra high temperature. Local structures of Zr in tektite was found to be glass-type; thus, estimated formation temperature of tektites was higher than 2800 °C based on XAFS results and ZrO₂-SiO₂ phase diagram. Because the local structures of Zr in fulgurite were similar to that in baddeleyite, the formation temperature of fulgurite was estimated in the range 1680-2800 °C by XAFS and ZrO₂-SiO₂ phase diagram. Saikia et al. (2008) proposed that formation temperature of fulgurite is 1600-2000 °C. This suggestion was consistent with estimation by Zr local structure analyses. Consistency between previous study of each natural glass and estimation by XAFS confirms that the formation conditions of natural glass can be estimated by Zr local structure analyses.

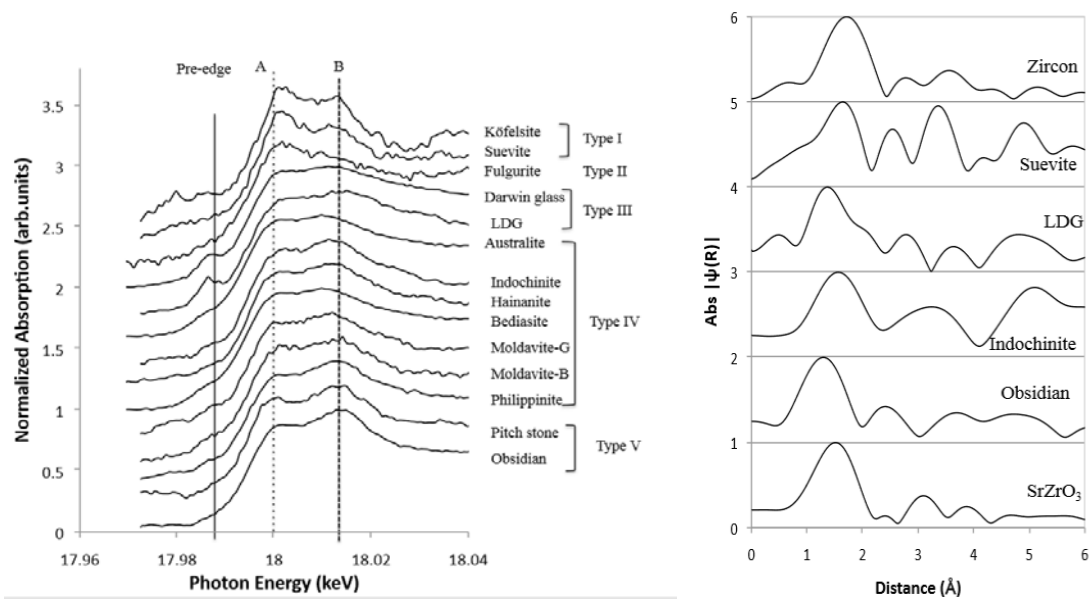


Figure 1.12. XANES spectra of Zr k-edge in tektite, impact glasses and volcanic glasses (left). EXAFS spectra of Zr in tektite, impact glasses, volcanic glass, SrZrO₃ and zircon (right).

Table 1.5. Interatomic distance between Zr and O and estimated coordination number of Zr probed by EXAFS.

Sample name	Estimated coordination number	Zr-O distance (Å)	R-factor (%)
Zircon	8	2.23 (6)	0.3
Suevite	7 and 8	2.22 (4)	3.6
LDG	7 and 8	2.21 (4)	0.8
Australite	7 and 8	2.22 (5)	0.1
Indochinite	7	2.20 (3)	0.7
Obsidian	6 and 7	2.17 (2)	0.5
SrZrO ₃	6	2.14 (3)	0.3

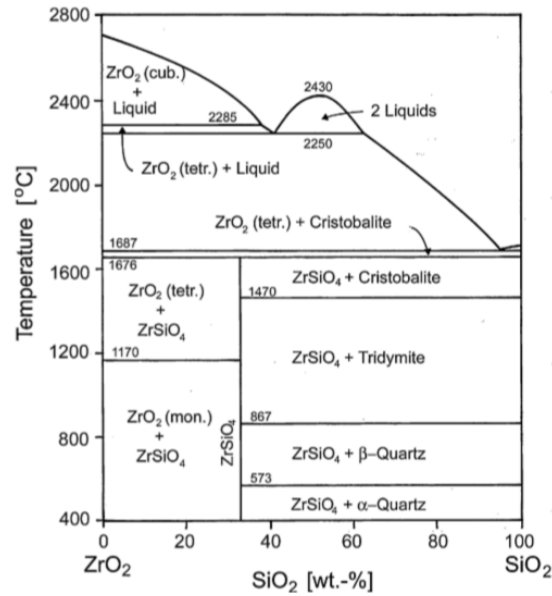


Figure 1.13. $\text{ZrO}_2\text{-SiO}_2$ phase diagram (Butterman and Foster, 1967; Kaiser et al., 2008).

1.8. MOTIVATION OF THIS STUDY AND OUTLINE

Meteorites contain glass components which are formed by collision of asteroids at the beginning of the solar system and by shock deformation after glass component formation. The glass component of meteorites, tektites, impact glasses and K-Pg boundary sediments may record complicated formation conditions. There have been, so far, only few studies focusing on glass component because it is difficult to study the coordination environments in glass component. Local structure analyses by XAFS method is used in various studies and XAFS can reveal the local structure changes of various target atoms. Therefore, XAFS method is suitable for estimating temperature and pressure conditions during formation from local structural analyses of each atom in meteorite impact-related material. We tried to estimate the formation conditions by performing local structure analyses of glass phase in meteorite impact-related materials. In this doctoral thesis, Zr and Ti local structure analyses in K-Pg boundary sediments (chapter 3, 4) and Ca, Ti, Fe and Zr local structure analyses in Tissint Martian meteorite (chapter 5) were performed to estimate the formation process of meteorite impact-related materials.

High temperature heating experiment of zircon was performed to obtain in situ observations of structural changes in high temperature environment by X-ray diffraction powder analyses. Quenched samples from high temperature were analyzed for chemical composition. XAFS analyses was performed to compare the local structures of Zr of natural glasses such as impact glasses and volcanic glasses (chapter 6). In order to obtain accurate analysis of XANES spectra, high temperature XAFS study were performed in several metal oxides (chapter 7). Transition metal oxides have pre-edge feature which is affected by temperature. Detailed comparison of pre-edge features can provide information about the local structure.

Chapter 2
Experiment of XAFS

2.1. X-RAY ABSORPTION FINE STRUCTURE (XAFS)

X-ray absorption fine structure (XAFS) refers to the details of how X-rays are absorbed by an atom at energies near the core-level binding energies of that atom. XAFS is the modulation of an atom's X-ray absorption due to the chemical and physical state of the atom. XAFS spectra are especially sensitive to local structures of atoms such as coordination environments and the interatomic distances between target atom and surrounding atoms. XAFS provides a practical and relatively simple way to determine the chemical state and local atomic structures around selected elements with various sample conditions like non-crystalline and highly disordered materials. XAFS measurements can provide a unique and direct measurement of chemical and physical state of dilute species in a variety of systems. Application of XAFS to geological research is growing.

Figure 2.1 shows a scheme of the X-ray absorption by sample of thickness x (cm). The incident X-ray beam has energy $E = h\nu = hc/\lambda = 12.39/\lambda$ (E is in KeV, h is Plank's constant, ν is the frequency, c is the velocity of light, and λ is wavelength in \AA) and intensity I_0 . Attenuation of incident beam intensity I_0 is described by an equation of the form $I = I_0 \exp(-\mu x)$, whereas μ is defined as the linear absorption coefficient.

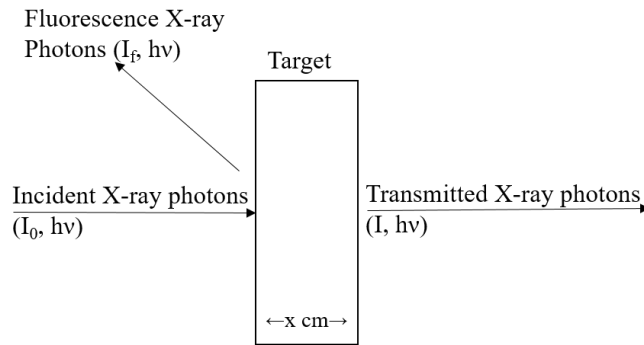


Figure 2.1. Schematic illustration of X-ray absorption.

XAFS measurement requires X-ray sources that have enough intensity and energy. The X-ray sources typically used for the XAFS measurement are synchrotron radiation facilities. Two most commonly used method for XAFS are transmission and fluorescence measurements. The transmission

method directly measures absorption by the sample with high concentration ($>2\%$) of the absorber. For lower concentrations the fluorescence method is used instead. Beam line settings of XAFS in BL9C and BL-NW10A in KEK, PF, Tsukuba are shown in figure 2.2 and 2.3. The schematic experimental arrangements of transmission and fluorescence methods are shown in figure 2.4. Using double crystal monochromator, quasi-parallel beam transforms into a convergent beam with a spatial distribution of photons of various energies. The first ion chamber is filled with an appropriate gas mixture to absorb about 20% of the incident beam. In the second ion chamber, the gas mixture is chosen to absorb all of the beams transmitted by the sample. N_2 , Ne, Ar and He are commonly used in these ion chambers. We normally used one copper pre-edge peak to calibrate X-ray energy. In XAFS experiments, errors are included in determining the absolute value of the observed energy coming from the d-space value of the monochromator crystal and the setting conditions. The X-ray energy resolution is also different for each device. Each pre-edge peak corresponds to the superposition of transitions to several electron orbitals with slightly different energy values.

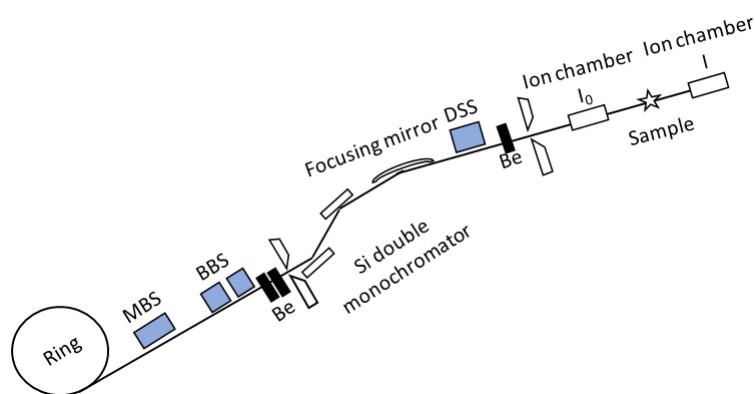
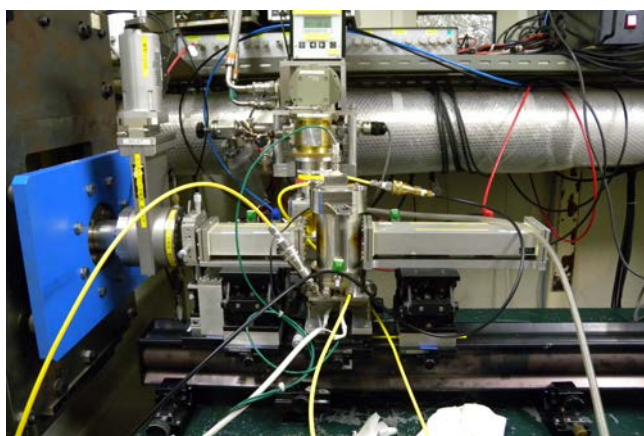


Figure 2.2. Schematic of XAFS measurements in BL-9C and BL-NW 10A.

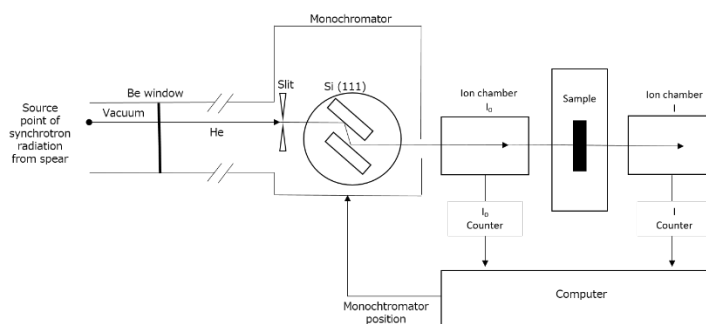


(a)

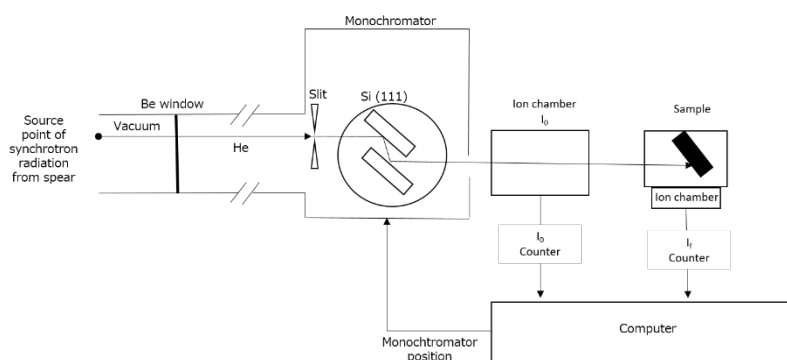


(b)

Figure 2.3. XAFS equipment in BL-9C (a) and BL-NW10A (b).



(a)



(b)

Figure 2.4. Experimental arrangement for XAFS measurement: transmission (a) and fluorescence (b).

2.2 DATA REDUCTION AND ANALYSIS

Outline of the data reduction and analysis technique are introduced in this section.

Steps in XAFS data analysis are as follows:

1. Convert measured intensities to $\mu(E)$ (figure 2.5). $\mu(E)$ is the energy dependence of the absorption coefficient.

2. Normalization to unit edge step.

3. Interpolation to k -space where k is wave number of photoelectrons.

4. Isolate the XAFS $\chi(k)$, the EXAFS function, is extracted from each measured spectrum using a standard procedure (Maeda, 1987). (figure 2.7)

5. k -weight the XAFS $\chi(k)$ and Fourier transform into R -space, where R -space represents the difference between the experimental data and calculated EXAFS interference function. (figure 2.8)

6. Inverse transform to isolate the shell data; this shell corresponds to the coordination shell.

7. Parameter refinements.

These steps are shown graphically in figure 2.5, 2.7 and 2.8. These figures are obtained from the data analysis of transmission XAFS of Zr K-edge in zircon.

Typical XAFS spectrum (figure 2.5) shows the absorption by the material as a function of the energy of the incident beam and is divided in two regions: XANES (X-ray absorption near edge structure) region (a few eV below to 100 eV above the absorption edge) and EXAFS (extended X-ray absorption fine structure) region (from 100 eV to as much as 1000 eV above the absorption edge). XANES features are attributed to single- and multiple scattering of the ejected photoelectron wave from the central

absorbing atom among its nearest and next-nearest neighbors. XANES is particularly sensitive to the geometrical arrangement of first and more distant neighbours around the absorber. EXAFS is due to constructive and destructive interference between the outgoing and backscattered photoelectrons. EXAFS can be analyzed to give information about distance between the absorber and its neighbours.

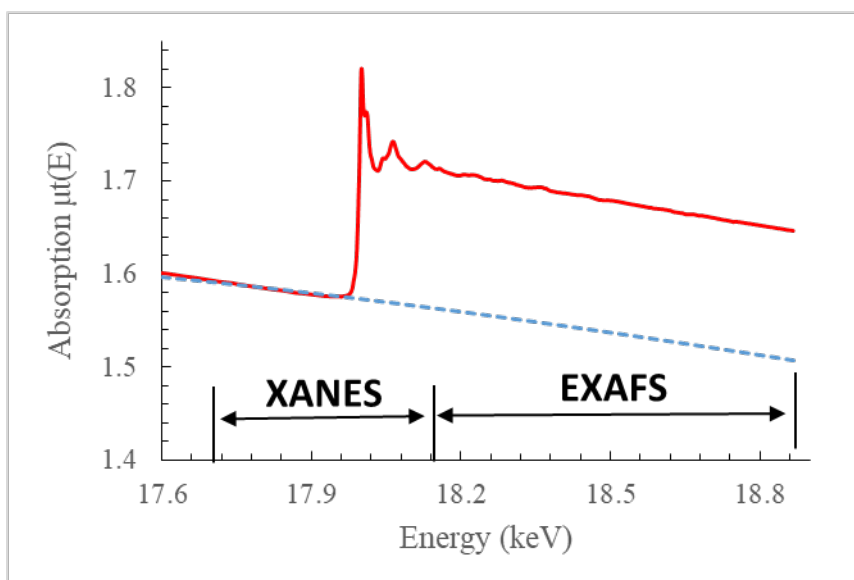


Figure 2.5. XAFS $\mu(E)$ for Zr in zircon. General outline of an X-ray absorption spectrum of an atom showing the XANES and EXAFS.

XANES is due to the transition from the inner shell to the unoccupied discrete level. XANES spectra are sensitive to hybridization of orbitals. The pre-edge feature, as shown in figure 2.6, has been observed the K-edge of transition metal compounds (Pandya and Koningsberger, 1991). This pre-edge is said to be an electric quadrupole transition from $1s$ to $3d$, whereas ordinary optical absorption is the electric dipole transition ($1s \rightarrow 2p$ or $2p \rightarrow 3s, 3d$) (Kawai, 2000). The origin of pre-edge feature in figure 2.6 is due to the electric dipole transition. The unoccupied p orbitals strongly hybridize with the d band for tetrahedral symmetry compounds as shown by group theory, where both p and d orbitals belong to the t_2 representation. Thus, the electric dipole transition is strongly observed at the energy of an empty d band. On the other hand, p and d orbitals never mix with each other for octahedral symmetry, where p orbital belongs to t_{2u} and d belongs to e_g and t_{2g} representations. Therefore, the p transition is observed at a different energy from the empty d band for octahedral symmetry compounds. The intensity and

energy shift of the pre-edge peak are good indices for fingerprinting the chemical environment in the compounds (Kawai, 2000; Yamamoto, 2008).

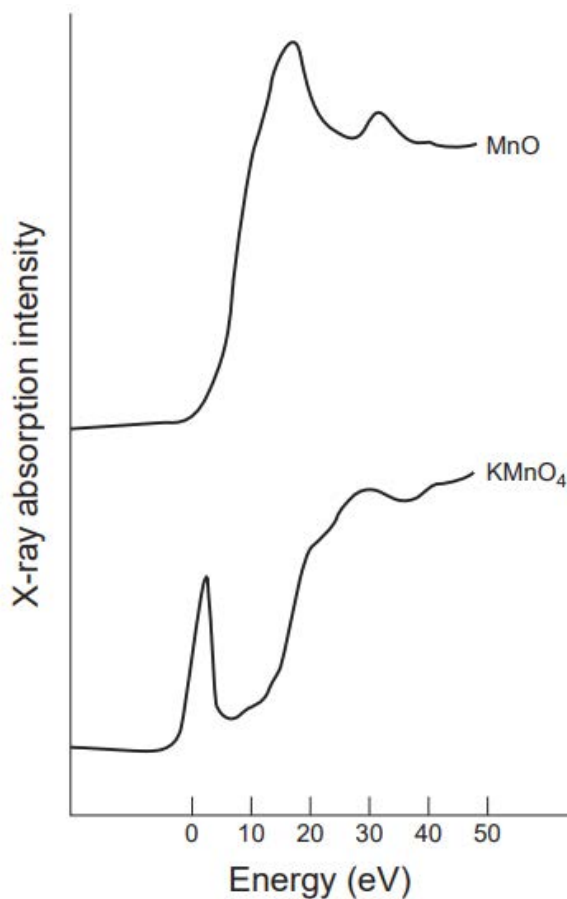


Figure 2.6. Mn K-edge XANES spectra of MnO (octahedral symmetry) and KMnO_4 (tetrahedral symmetry). Pre-edge peak is observed in the KMnO_4 spectrum (Pandya and Koningsberger, 1991).

The energy dependence of the absorption coefficient $\mu(E)$ in transmission mode XAFS measurement can be expressed as $\mu t(E) = \ln(I_0/I)$ where I_0 is the X-ray intensity incident on a sample, I is the X-ray intensity transmitted through a sample and t is a sample thickness.

The aim of data analysis of EXAFS is to determine the bond distance. Data analysis performed using the standard procedure (Maeda, 1987; Yoshiasa et al., 1999). EXAFS can be defined as the function $\chi(E)$ by

$$\chi(E) = \frac{\mu(E) - \mu_0(E)}{\Delta\mu_0(E)}, \quad (1)$$

where $\mu(E)$ is the experimental absorption coefficient and $\mu_0(E)$ is a smooth background function representing the absorption of isolated atom coefficient, and $\Delta\mu_0(E)$ is the measured jump in the absorption $\mu(E)$ at the threshold energy E_0 . In order to relate $\chi(E)$ to structure parameters, we need to convert the energy E into the modulus of the wave vector k of the photoelectron using the relation:

$$k = \sqrt{\frac{2m}{\hbar^2} (E - E_0)} = [0.262 \times (E - E_0)]^{1/2}, \quad (2)$$

where m is the mass of the electron, \hbar is Plack's constant divided by 2π , E is the kinetic energy of the photoelectron, and E_0 is the energy of the photoelectron at $k = 0$.

$\chi(k)$ is normalized using MacMaster coefficients according to the EXAFS workshop report (Lytle et al., 1989). In quantitative analyses we carried out the Fourier-filtering and a non-linear least-squares fitting by comparing the observed $\chi(k)_{\text{exp}}$ and calculated $\chi(k)_{\text{calc}}$. The EXAFS interference function, $\chi(k)$, is thus deduced as shown in figure 2.7 (a). Further, $\chi(k)$ is multiplied by a power of k^3 to compensate for the diminishing amplitudes at high k -values (figure 2.7b). The next step in the analysis is to separate the signals from sums of sine waves corresponding to the different shells of atoms using a Fourier filltering method in order that the number of fitting parameters are reduced. A Fourier transform of the data, $\Phi(R)$, is then performed

$$\Phi(R) = \sqrt{1/2\pi} \int_{k_{\min}}^{k_{\max}} W(k) k^3 \chi(k) \exp(-2ikR) dk. \quad (3)$$

$W(k)$ is a Hanning window function given by

$$W(k) = \frac{1}{2} \left[1 - \cos \left\{ \pi \left(\frac{k - k_{\min}}{k_{\max} - k_{\min}} \right) \right\} \right], \quad (4)$$

where k_{\min} and k_{\max} are the minimum and maximum values of k at which experimental data are obtained. Figure 2.8 shows experimental $\Phi(R)$ of the zircon. Derived $\Phi(R)$ exhibits peaks that correspond to the average frequency of the corresponding shell's EXFAS, which is related to coordination shell. The position of the peak is related to the atoms in the shell and the atomic number of the atoms in the shell. In figure 2.8, first peak around 1.6 Å and second peak around 3.2 Å represent Zr-O bond and Zr-Zr bond, respectively. Thus, the function of $\Phi(R)$ is analogous to a radial distribution function (Rehr et al., 1991; Stern et al., 1991).

We used the EXAFS formula with the cumulant expansion. Cumulants κ_n of a probability distribution are a set of quantities that provide an alternative to the moments of the distribution, up to the fourth order term (Ishii, 1992),

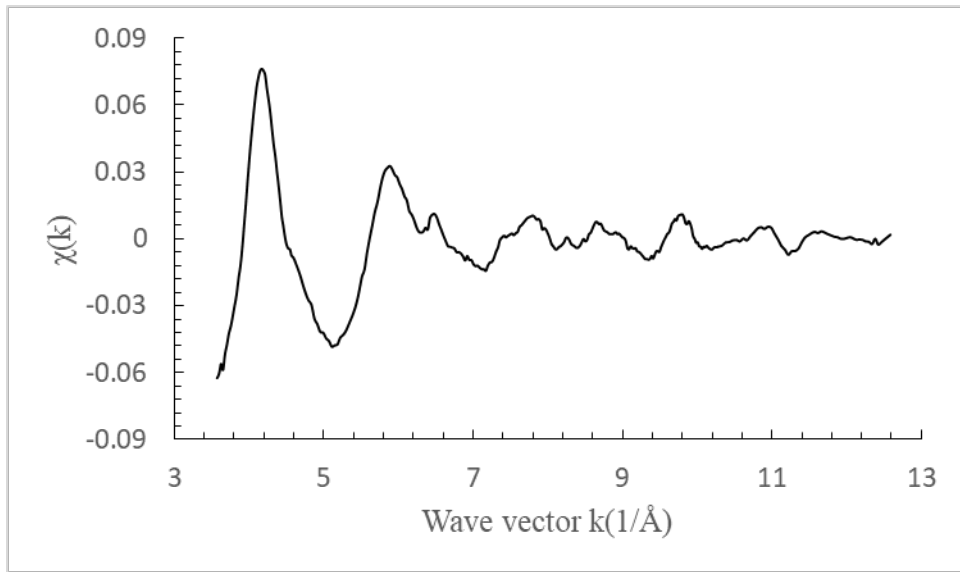
$$\chi(k) = \sum_B (N_B / k R_{AB}^2) |f_B(k; \pi)| \exp[-2R_{AB}/(k/\eta)] \times \exp[-2\sigma_2 k^2] \sin[2kR_{AB} + \psi_{AB}(k)] \quad (5)$$

where N_B is the coordination number of scattering atom B at a distance R_{AB} from the absorbing atom A , $|f_B(k; \pi)|$ is the backscattering amplitude of photoelectrons and $\psi_{AB}(k)$ are calculated using FEFF3 program (Rehr et al., 1991). σ_n denotes the n th cumulant. λ is the damping factor stemming from many-body effects. This damping factor is the analogue of the X-ray diffraction Debye-Waller factor, which is used to describe the attenuation of X-ray scattering caused by atomic thermal vibration. The mean free path λ of the photoelectron is assumed dependent on the wavenumber, $\lambda(k) = k/\eta$, where η is a constant. Analyses of the XAFS were performed using *XAFS93* program (Maeda, 1987), whose details are given by Yoshiasa et al. (1997). The single shell fitting is carried out for each nearest-neighbour distance. Because the third- and fourth-order terms in the cumulant expansion are negligible, the final refinement is performed in the harmonic model by the structural parameters R_{AB} , σ_2 , and η , where ΔE_0 is the difference between the theoretical and experimental threshold energies. A reliability of fit parameters,

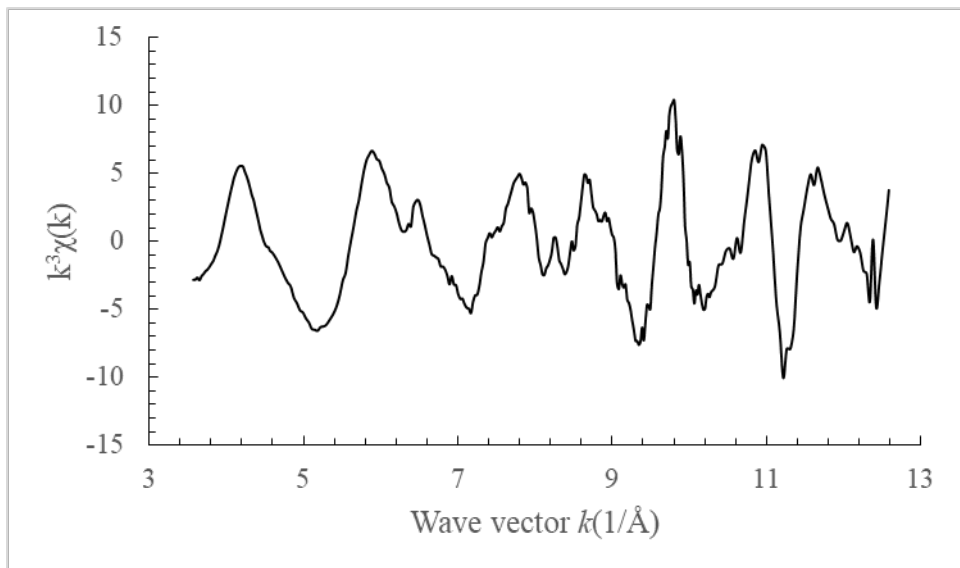
$$R = \sum |k_s^3 \chi_{exp}(k_s) - k_s^3 \chi_{calc}(k_s)| / k_s^3 \chi_{exp}(k_s), \quad (6)$$

between the experimental and calculated EXAFS functions less than 0.15 (in the following chapter 15%) is considered an indication that the model is correct.

In this doctor thesis, we investigate natural glass samples. In Wang et al. (2011, 2013), on the basis of ionic radius of four-coordinated Ti (0.42), five-coordinated Ti (0.51), six-coordinated Ti (0.61) and six-coordinated O (1.4) (Shannon 1976), coordination numbers of Ti in tektites were estimated from the sum of ionic radius of Ti and O. In the case of intermediate Ti-O distance between Ti(IV)-O and Ti(V)-O, Wang et al. (2011, 2013) represented the coordination number of Ti as a four and five. On the basis of this estimation, we represent the coordination number of each atom in the following chapter.



(a)



(b)

Figure 2.7. Experimental EXAFS interference function for Zr k-edge of zircon. (a) Isolated EXAFS $\chi(k)$ for Zr, (b) k -weighted EXAFS interference function.

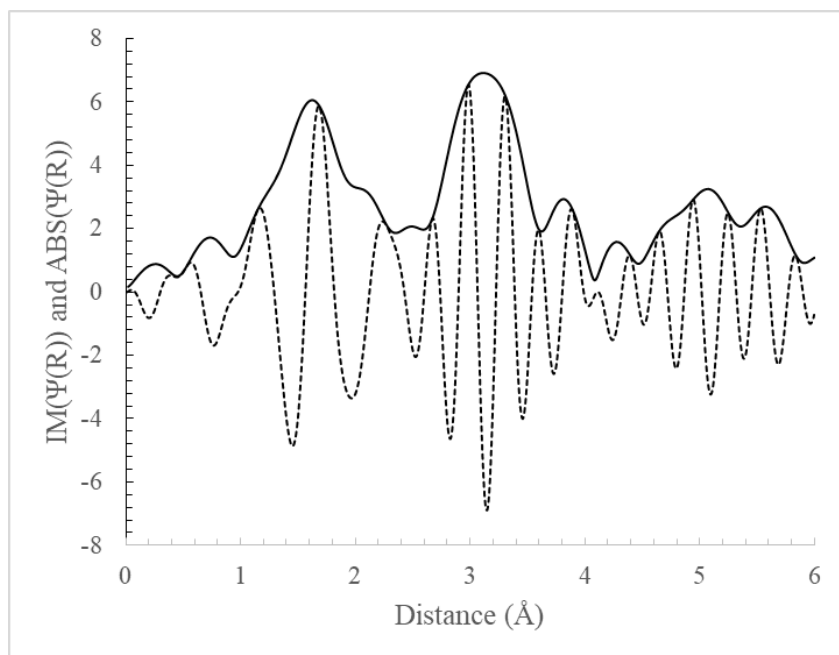


Figure 2.8. Magnitude of the Fourier transform of $k^3\chi(k)$ (solid line) from figure 2.7(b) together with imaginary part of Fourier transform (dashed line). No phase shift corrections are made.

Chapter 3
**Local structures of Zr in K-Pg
boundary sediments**

3.1. INTRODUCTION

In the general introduction (chapter 1.4), K-Pg boundary sediments (K-Pg sediments) was described. Powder XRD analysis showed that major Fe component of K-Pg sediments was goethite (figure 1.6); on the other hand, XAFS analyses of Fe and As showed that Fe component in K-Pg sediments was ferrihydrite-schwertmannite (Sakai et al., 2007; Miyano et al., 2016). XAFS analysis of K-Pg sediments provided essential information of local structures of Fe, which cannot be obtained by XRD. Previous local structure analyses for several elements in K-Pg sediments provide information about the sedimentation conditions of K-Pg sediments (Sakai et al., 2007; Guili et al., 2008; Okube et al., 2012; Miyano et al., 2016). However, since each local structure was changed by weathering and diagenesis, information about meteorite impact is difficult to obtain. Local structures of Zr in impact-related glasses recorded the condition of meteorite impact (chapter 1.7). Formation conditions of natural non-crystalline material can be estimated by XAFS method based on the local structure similarity between natural glass, zircon and baddeleyite (Tobase et al., 2015b). XANES and EXAFS studies of the local structures of Zr in K-Pg sediments are expected to provide more comprehensive data such as formation temperature, pressure and quenching history of the impact event. When impact-related materials such as micro-tektites and shocked quartz are observed in the sedimentary rocks, it is clear that the sedimentary rocks were produced by meteorite impact event. However, there is not always evidence of meteorite impact event in sediments and the history of meteorite can be lost because of weathering and alteration. Thus, it is necessary to find other traces of meteorite impact events. When an element in sediments maintains the local structures, which is estimated to be formed by meteorite impact, trace of meteorite impact event may be observed by local structure analyses. In this chapter we have examined whether the history at impact events was preserved in the local structures around Zr in K-Pg sediments. We discuss whether the local structures of Zr could be a proxy of meteorite impact.

3.2. SAMPLE AND EXPERIMENTS

The specimen of K-Pg boundary sediments was obtained from Stevns Klint in Denmark. Stevns Klint is a white chalk cliff located southeast of Store Huddinge on the Danish island of Zealand. Stevns Klint is one of the best exposed K-Pg boundary layer in the world.

The beam size of XAFS measurement can be changed by user and the selected beam size is 1mm×1mm. Analytical point of K-Pg sediments was the same as that studied by Sakai et al. (2007), Okube et al. (2012) and Miyano et al. (2016). In order to investigate the local structures around Zr atoms in K-Pg boundary sediments, we prepared several reference natural minerals and glasses such as zircon (ZrSiO_4), PbZrO_3 , SrZrO_3 , volcanic glasses (obsidian and pitch stone), tektite (indochinite) and impact glasses (suevite and Libyan desert glass).

3.3. RESULTS AND DISCUSSION

3.3.1. Radial distribution and local structures

The EXAFS $k^3\chi(k)$ functions were transformed into the RDFs for the Zr K-edge of K-Pg sediments and reference materials, as shown in figure 3.1. In order to obtain information on the structure parameters, we conducted parameter fitting with analytical EXAFS. The obtained structural parameters are summarized in table 3.1. Average Zr-O distance in K-Pg boundary sediments is 2.164 Å and the coordination number is in the range between 6 and 7. The Zr-O distance, coordination number and RDF of K-Pg boundary sediments are similar to those of rhyolitic volcanic glasses. The Zr-O distances and RDFs for other natural glasses were presented in Tobase et al. (2015b), as shown in chapter 1.7.

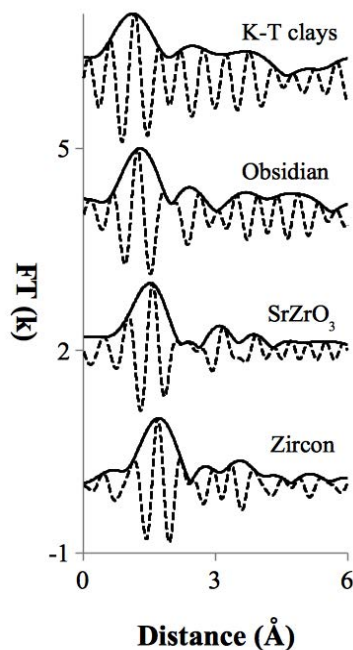


Figure 3.1. Fourier transforms of the Zr K-edge EXAFS oscillation function $k^3\chi(k)$. No phase shift corrections are made. The first nearest peaks correspond to Zr-O bonds. Solid line is the magnitude part, dotted line is the imaginary part of the spectra.

Table 3.1. Local structure parameters around Zr determined by XAFS. The expected bond distances with some offset of six-, seven and eight-coordinated Zr-O based on the Shannon ionic radii (1976) and chapter 2.

Sample	Coordination number	Zr-O distance (Å)	R-factor (%)
K-Pg sediments	6 and 7	2.164 (4)	3.6
Obsidian	6 and 7	2.171 (2)	0.5
SrZrO ₃	6	2.141 (3)	0.3
Zircon	8	2.226 (6)	0.3

3.2.2. XANES spectra of K-Pg boundary sediments and natural glasses

The zirconium XANES spectra in K-Pg boundary sediments and reference materials are shown in figure 3.2. Two main absorption edges are at 18.002 and 18.014 KeV. XANES spectrum of K-Pg sediments is similar to that of obsidian and tektites. This XANES pattern is clearly

different from those observed in zircon and baddeleyite (Mountjoy et al., 2000 and Tobase et al., 2015b). The Zr-O distance and RDF in K-Pg boundary sediments are similar to those in obsidian and tektites. Local structures in K-Pg sediments are similar to those in obsidian and tektites, from which we conclude that Zr in K-Pg sediments maintains glass-like local structures and records the thermal quenching history at meteorite impact of K-Pg boundary age. Information about local structures of Zr in K-Pg sediments differs from that of As, Zn, Ca, Fe, Ti and Mn in K-Pg sediments (Sakai et al., 2007; Okube et al., 2012; Miyano et al., 2016). The local structures of As, Zn, Ca, Ti, Fe and Mn in K-Pg sediments were affected by weathering and diagenesis, contrary to that of Zr in K-Pg sediments which is not changed from glass-like structure. We concluded that local structures of Zr may not be changed easily by weathering and diagenesis.

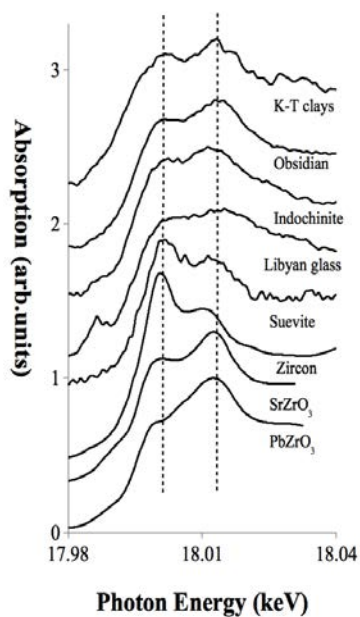


Figure 3.2. Experimental Zr K-edge XANES spectra of K-Pg sediments and reference materials. There are double peaks after threshold energy. One of the peaks at 18.0017 (1) KeV position of suevite is shown by dotted line for comparison purpose, the other peak at 18.0134 (1) KeV of K-Pg sediments is shown by a dashed line.

Figure 3.3 shows a detailed comparison of threshold energy for K-Pg

sediments, obsidian and SrZrO₃. We defined the threshold energy of Zr as the half height position from the highest peak. Threshold energy of K-Pg sediments is 2.0 eV lower than that of volcanic glasses. On the basis of the threshold energy shifts by 7.0~6.0 eV (Ressler et al., 2002), the total charge of Zr ions in K-Pg sediments is less than 4+ and can be estimated empirically as 3.8+~3.9+. Okube et al. (2005) observed a shift of the threshold energy to the lower side in Zr K-edge XANES spectra of SrZr_{0.9}Yb_{0.1}O_{3-δ} perovskite-type proton conductor at higher temperature. Yoshiasa et al. (2009) also observed a shift of the threshold energy to higher side in Zr K-edge XANES spectra in nano-size ZrO₂ particles at high pressure. Threshold energy of Zr elements depends on oxidation state, formation temperature and pressures. The shift of threshold energy of Zr XANES in K-Pg sediments suggests that local structures of Zr in K-Pg sediments were formed under high temperature-, low pressure- and low oxidation-conditions. Thus, Zr component of K-Pg sediments is estimated to be formed by accumulation of nano-glass material quenched in the space (Wang et al., 2013b). On the basis of the glass-like local structures of Zr in K-Pg sediments, the possibility of estimating a large meteorite impact event from the Zr local structure investigation arises. The local structure analysis of Zr may become a key factor for checking the occurrence of a meteorite impact in sedimentary rocks at the time of mass extinction.

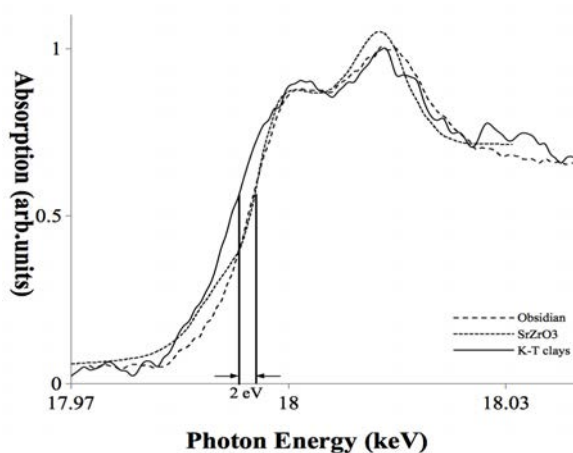


Figure 3.3. Detailed comparison for Zr K-edge XANES spectra of K-Pg sediments, obsidian and SrZrO₃.

Chapter 4
**Local structures of Ti in K-Pg
boundary sediments**

4.1. Introduction

In chapter 3 we have seen that the local structure analysis of Zr may become a key for checking a possibility of the meteorite impact in sedimentary rock at the time of mass extinction. However, because of the low Clarke of Zr, its abundance in sediments is not always sufficient to obtain reliable information. The higher Clarke of titanium makes it a more likely marker in sedimentary rocks. The analysis of the local structures of Ti in K-Pg boundary sediments may therefore become a key factor to evaluate the possibility of meteorite impact events, as for the case of Zr. This is the motivation for the study of the local structures of Ti atoms by Ti K-edge XAFS spectroscopy presented in this study.

Titanium occurs in a number of minerals of primary industrial importance, like the polymorphs of TiO_2 (rutile, anatase, brookite), titanite and ilmenite, widely distributed in the Earth's crust and lithosphere. Moreover, it is abundantly distributed in rocks, water bodies and soils. Titanium and zirconium belong to the same group in the periodic table of the elements, have close atomic sizes and chemical properties; they instead differ largely by their abundance, the respective Clarke being 0.66% and 0.01%. Gao et al. (2010) reports that rutile and zircon (ZrSiO_4) in eclogites are related to the fluid activity and thermic-history of ultra-high pressure metamorphism. The local structures of Ti and Zr in tektites are unique and bear records of the formation condition under high temperature (Wang et al., 2011; Tobase et al., 2015b). One may reasonably expect that the local structures of Ti in the sample remained essentially identical to that formed by the meteorite impact, as it was in the case for Zr.

Glass structure is affected by pressure and temperature conditions during the glass formation process (Stebbins and McMillan, 1989; Yarger et al., 1995). According to research on synthetic glass by Paris et al. (1994), Mysen and Neuville (1995), Farges et al. (1996b, c) and Farges and Brown (1997), four-coordinated Ti occurs under higher temperature and lower pressure. On the contrary, six-coordinated Ti (the most common coordination for titanium in oxides) occurs under lower temperature and

higher pressure. Wang et al. (2011, 2013a) reported the local structures of Ti in meteorite impact-related glasses (tektites and impact glasses) and volcanic glasses. In tektites, titanium is present in 4-, 5- and 6-fold average coordination, showing that tektites formed under variable conditions. Impact glasses and volcanic glasses have 5- and 6-fold coordinated titanium. The analysis of the local structures of Ti in K-Pg boundary sediments may bring information about ancient meteorite impacts. XANES and EXAFS studies of the local structures of Ti in K-Pg boundary sediments are expected to provide more comprehensive information such as formation temperature, pressure and quenching history on the impact.

As a reference, we used D-C boundary sediments (D-C sediments) collected in the Cat Co Cape on the Cat Ba Island, Hai Phong Province, northern Vietnam. By comparison between the Ti local structures of D-C sediments and those of other reference materials, we can estimate the formation process of D-C sediments. In addition to D-C sediments, we use a reference sediment from Gifu, Japan, which was not obtained from the boundary. Local structures of Ti in sediment from Gifu is expected to differ from boundary sediments, therefore, comparison of those in K-Pg sediments, D-C sediments and sediments from Gifu will provide the clearly difference of local structures. Formation condition of sediments can be obtained based on the local structure difference of Ti.

4.2. SAMPLE AND EXPERIMENTS

The sample of K-Pg boundary sediments used in this research was from Stevns Klint in Denmark. Analytical point of XAFS is the same as that in chapter 3. D-C sediments were collected from the lower part of Bed 116 at Loc. 01 described by Komatsu et al. (2012a, b, 2014), in the western part of Cat Co 3 Beach on Cat Ba Island, northeastern Vietnam. Half of the soils or more is composed by non-crystalline material. In order to study local structures of Ti atoms in K-Pg boundary clays, we prepared several reference titanium compounds which have characteristic Ti local structures (Wang et al., 2011, 2013): TiO₂-rutile, -anatase, -brookite,

perovskite (CaTiO_3), geikielite (MgTiO_3), tausonite (SrTiO_3), macedonite (PbTiO_3), tektites (moldavite brownish and moldavite green), impact glass (suevite and impactite), volcanic glass (obsidian and Kilauea volcanic glass (KVG)), pseudotachylite and sediment from Gifu, Japan.

4.3. RESULTS

4.3.1. XANES spectra of K-Pg boundary sediments, D-C sediments and reference materials

Figure 4.1 shows a comparison of Ti X-ray absorption near edge structure (XANES) spectra between K-Pg sediments and typical reference materials. XANES spectra reflect the local environments around target atoms. The XANES spectra in K-Pg boundary sediments, D-C boundary sediments and reference material are shown in figure 4.2. The main absorption peaks are shown by the dotted lines in figure 4.2. XANES spectrum of K-Pg sediments are similar to that of suevite, not those of rutile and anatase. On the other hand, D-C sediments are similar to those of anatase and obsidian. XANES spectrum of sedimentary rock from Gifu is the sum of the patterns of TiO_2 rutile and anatase.

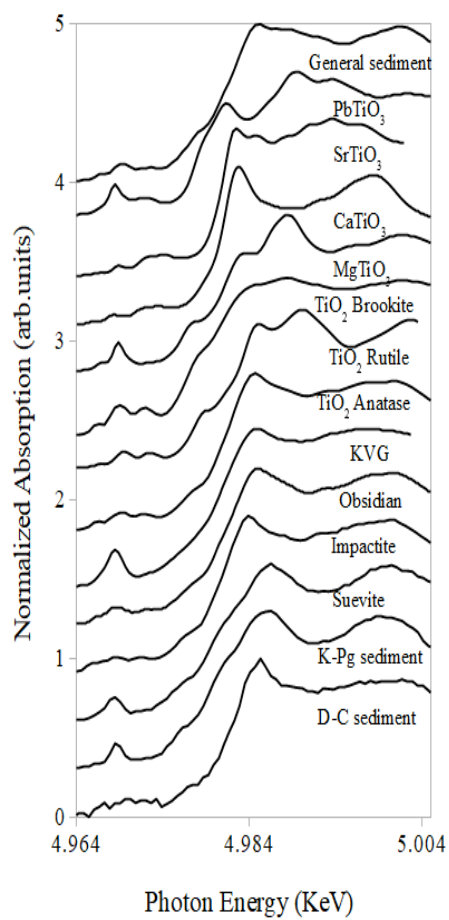


Figure 4.1. Experimental Ti K-edge XANES spectra of K-Pg sediments, D-C sediments and typical reference materials.

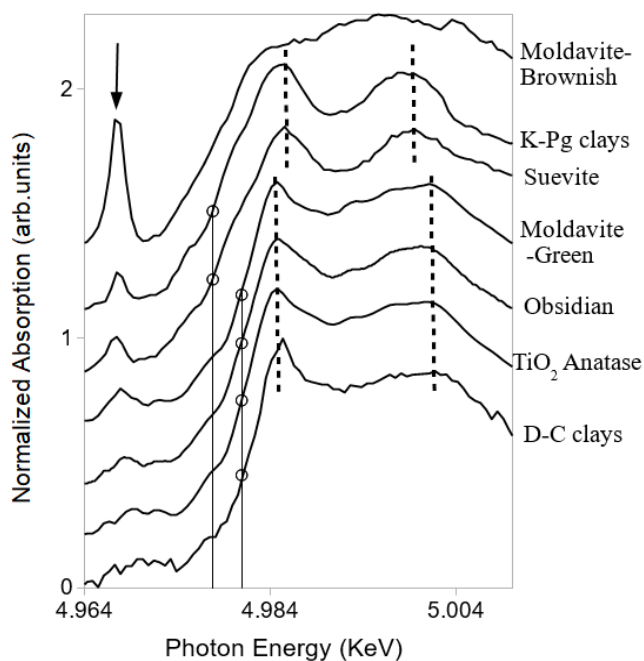


Figure 4.2. Detailed comparison of experimental Ti K-edge XANES spectra of K-Pg sediments, D-C sediments and reference materials. The highest peak position of K-Pg sediments at 4.9865 (1) KeV and that of D-C sediments at 4.9853 (1) KeV are shown by dotted line for comparison purpose. The shoulder peak which is shown by solid line and circle has different position and shape between K-Pg sediments and D-C sediments. The pre-edge peak is shown by an arrow.

The Ti pre-edges are located 18 ± 3 eV before the first absorption peak. The shape of pre-edge peak of Ti XANES spectra is strongly related to Ti local structures (Farges et al., 1996a, b, c; Hiratoko et al., 2013). Wang et al. (2011) reported that the pre-edge peak heights of tektites are 14-59%, the peak top being defined as 100%. The pre-edge peak intensities have negative correlation with Ti coordination number, whereas the pre-edge peak position have positive correlation (Farges et al., 1996a, b, c). The highest pre-edge peak in moldavite-brownish, where Ti is 4-coordinated, is 59%, whereas the lowest pre-edge peak in moldavite-green, where Ti is 6-coordinated, is 11%. The lowest photon energy of pre-edge in moldavite-brownish (4-coordinated Ti) is 4.9672 (1) KeV and the highest photon energy of pre-edge in anatase (6-coordinated Ti) is 4.9696 (1) KeV. These

trends are consistent with previous studies (Farges et al., 1996a, b, c; Farges and Brown, 1997). The pre-edge heights and energies for five-coordinated Ti materials fall between the values measured for the two other Ti coordinations (Farges et al., 1996a, b, c; Wang et al., 2013). The pre-edge features in XANES spectra of D-C sediments is weak and similar to that in anatase. In contrast, a sharp pre-edge peak is clearly observed in XANES spectra of K-Pg sediments. The normalized pre-edge intensity of K-Pg sediments is 16.5%, which is similar to that of suevite (15.6%) (five-coordinated Ti). Previous studies reported that the width of pre-edge peak full width at half-maximum (FWHM) is related to coordination number of Ti (Gregor et al., 1983; Yarker et al., 1986; Galois and Calas 1993; Wang et al., 2011). The value of FWHM in K-Pg sediments is 2.4, which is lower than in modavite-green (2.9), where Ti is six-coordinated Ti. On the basis of the height of pre-edge, the position of pre-edge and the width of FWHM, Ti atoms in K-Pg sediments is estimated to be five-coordinated.

4.3.2. Radial distribution and coordination environments

The EXAFS $k^3\chi(k)$ functions were transformed into the radial distribution functions (RDF) for the Ti K-edge of K-Pg sediments, D-C sediments and some reference materials, as shown in figure 4.3. The shape of the RDFs for K-Pg sediments and suevite are similar to the XANES spectra of these two samples in figure 4.2. On the other hand, in the case of D-C sediments, the shape of RDFs is similar to obsidian, whereas those for D-C sediments and perfectly crystallized anatase are different. The second and third nearest neighbour peaks in anatase clearly appear (arrow in figure 4.3), because the crystalline phase anatase has three-dimensional periodicity. On the other hand, those peaks in D-C sediments do not clearly appear. This means that three dimensional periodicity is not achieved in D-C sediments, indicating that Ti occupies cation sites in non- or poorly crystalline environments or phases.

Detailed structure parameters were obtained through parameter fitting with analytical EXAFS formulae (Maeda et al., 1987; Yoshiasa et al.,

1999). The results are summarized in table 4.1. As a reference, we have taken the Ti-O distances in crystalline compounds containing the corresponding coordination polyhedra for titanium (ECoN and weighted average distances computed with CHARDI2015: Nespolo & Guillot, 2016) as well as the sum of the effective ionic radii of Ti^{4+} and O^{2-} in Shannon (1976).

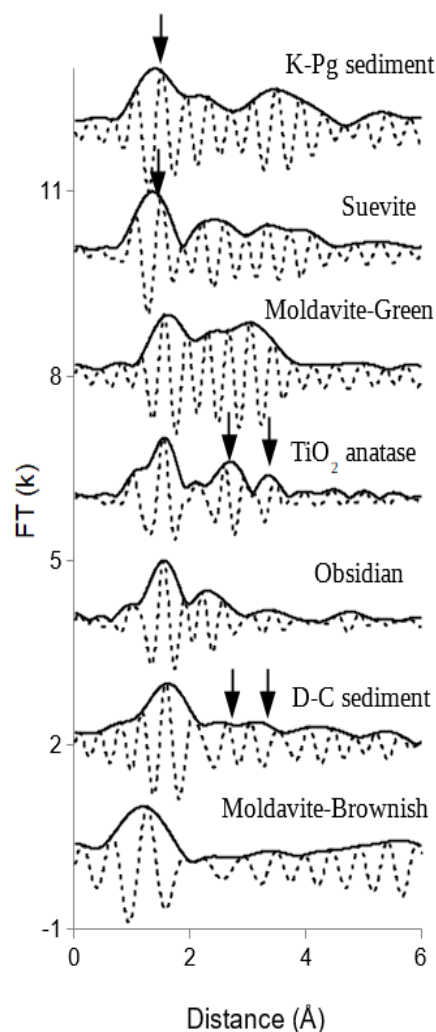


Figure 4.3. Fourier transforms of the Ti K-edge EXAFS oscillation function $k^3\chi(k)$. No phase shift corrections are made. The first nearest peaks correspond to Ti-O bonds. Solid line is the magnitude part, dotted line is the imaginary part of the spectra.

Table 4.1. Coordination environment parameters of Ti determined by XAFS. The coordination number is estimated by comparison between the experimental Ti-O distance and the weighted average distance in crystalline phases (anatase, potassium sodium titanate and barium orthotitanate for sixfold, fivefold and fourfold the coordination respectively).

Sample	Ti-O distance (Å)	Estimated coordination number	Weighted average distance in the reference	R-factor (%)
TiO ₂ (anatase)	1.979 (4)	6	1.955	0.7
Moldavite-Green	2.001 (4)	6	1.955	3.5
D-C sediments	1.979 (2)	6	1.955	0.3
Obsidian	1.969 (2)	6	1.955	0.9
K-Pg sediments	1.904 (5)	5	1.887	0.3
Suevite	1.887 (2)	5	1.887	2.5
Moldavite-brownish	1.817 (4)	4	1.802 – 1.819	6.3

For six-fold coordinated Ti (IV) we used anatase as reference (Horn et al., 1972), which presents four bonds at 1.934 Å and two bonds at 1.980 Å, resulting in slightly deformed octahedron (ECoN = 5.97) and weighted average distance 1.948 Å, which fits very well the sum of Shannon radii 1.955 Å. Fivefold coordination of Ti(IV) is relatively rare and often corresponds to highly distorted coordination polyhedra. As a reference, we have chosen potassium sodium titanite KNaTiO₃ (Werthmann and Hoppe, 1985), in which the coordination polyhedron titanium is less deformed, as shown by the ECoN value of 4.56, not too far from 5. The weighted average distance is 1.887 Å, which is somewhat longer than the sum of the Shannon radii, 1.86 Å but very close to the value found in suevite (table 4.1).

Finally, tetrahedral coordination for Ti(IV) in oxides is also rare and has been found in barium orthotitanate, Ba₂TiO₄, occurring in orthorhombic (α' : Guenter and Jameson, 1984) and monoclinic (β : Wu and

Brown, 1973) polymorphs. In the former, three almost regular tetrahedra (ECoN 3.99) have Ti-O weighted average distances 1.802, 1.818 and 1.819 Å respectively, in the latter (which has a unit cell volume about one third of the orthorhombic polymorph) a single almost regular tetrahedron (ECoN 3.97) has Ti-O weighted average distance 1.806 Å: these values are somewhat larger than the sum of Shannon radii, 1.77 Å.

The Ti-O average distances obtained by XAFS are shown in table 4.1. The value for anatase, for which the six-fold coordination is established from XRD data, is 1.979 Å, which is very close to the longer bonds reported above and a bit longer than the weighted average. The same value has been obtained for D-C boundary sediments, in which Ti (IV) is therefore evidently in six-fold coordination as well. On the other hand, in K-Pg boundary sediments the result is 1.904 Å, which is closer to the value for five-fold coordination, but a bit longer than that of suevite, 1.887 Å, in which Ti(IV) is considered five-fold coordinated as well. The Ti-O distance and RDF for the moldavites were presented in the Wang et al. (2011, 2013a): the green variety has Ti (IV) in six-fold coordination, the brownish variety in four-fold coordination.

4.4. DISCUSSION

It is generally assumed that the local structures of Ti in natural glasses are hardly influenced by weathering, and those in tektites bear information about the formation condition such as temperature, pressure and quenching rate (Wang et al., 2011, 2013a). On the basis of Ti-O distance obtained by EXAFS analysis, Ti atoms in K-Pg sediments are estimated to be five-coordinated. Pre-edge intensity, pre-edge position and FWHM also support this conclusion. Moreover, XANES and EXAFS spectra of K-Pg sediments show similar features to those of suevite, which also has five-coordinated Ti; the similarity of the spectra of these two materials indicates that Ti-local structures in K-Pg sediments were likely formed under conditions similar to those in which suevite forms. According to Engelhardt (1997), glassy suevite is formed under high temperature (900-1300 °C) and high pressure (45-60 GPa); if K-Pg sediments were formed under similar

conditions, as suggested by the similarity of the coordination environments, then a meteorite impact event can be considered a highly probable cause.

Figure 4.2 compares Ti K-edge XANES spectra of K-Pg sediments, D-C sediments and reference materials, from which appears a clear similarity of D-C sediments, anatase and obsidian. This similarity of XANES spectra indicates that the local structures around Ti in D-C sediments have volcanic glass or anatase structure. On the other hand, EXAFS spectra (figure 4.3) shows weak peaks for second and third neighbours in case of D-C sediments, which are absent in the case of obsidian but stronger for anatase. This indicates that the local structures of Ti in D-C sediments are intermediate between these two materials and suggests that the original glass-like local structures were changed to anatase-like local structures by devitrification, a well-known phenomenon in volcanic glass. In addition to the information of EXAFS spectra, shape of pre-edge feature of D-C sediments is considered to be related to devitrification. According to Wang et al. (2011, 2013a), most of natural glasses have single pre-edge, which is different from the shape of pre-edge of anatase. Based on the similarity of pre-edge in D-C sediments and that in anatase, devitrification in coordination environment of Ti in D-C sediments is also inferred. Anatase is known to crystallize first as a metastable phase from glass under high temperatures in the stability region of rutile: when the cooling rate is relatively slow or glass is affected by diagenesis, crystallization of anatase occurs (Yau et al., 1987; Penn and Banfield, 1999; Li and Ishigaki, 2002). In local structures of Ti in D-C sediments, the initial state may be considered to have disappeared by devitrification. The disappeared initial state of that in D-C sediments could be revealed by the XAFS analyses of Zr, since Zr local structures do not change by weathering and diagenesis (Tobase et al., 2015a). Tobase et al. (2015a) proposed the analyses of the local structures of Zr as a key for tracing records of meteorite impact; however the exploitation of Zr is limited by its low Clarke. Ti has a higher Clarke and is also more abundant in sedimentary rocks. Combining the information about the local structures of Ti and Zr, we can expect to

increase the reliability of the information obtained by XAFS, which may therefore become a new key factor for discussing the probability of a large meteorite impact as a cause of mass extinction.

Chapter 5

**Local structures of Ca, Fe, Ti and
Zr in Fusion crust of Tissint
meteorite**

5.1. INTRODUCTION

In chapter 1.5, a general introduction of SNC (shergottites, nahklites and chassignites) meteorites was presented. SNC meteorites were ejected by other meteorite impact on Mars and then SNC meteorites fell on Earth. Tektites were formed by the following process: mineral or rock on Earth melted by meteorite impact, the melt quenched in space and quenched melt fell back on Earth. In this thesis, Martian meteorites are regarded as “Martian tektite” based on the similarity of the formation process between Martian meteorites and tektites. In general, meteorites have fusion crust on the surface of their body. Fusion crusts experienced high temperature and rapid quench condition, are thin and are altered from the bulk of the meteorite. Formation process of Martian meteorites can be estimated from mineral of bulk of meteorite (Baziotis et al., 2013). The core and the fusion crust of the meteorite present a glass content. Several studies elucidated the environment of Mars from mineral inclusions of Martian meteorites (Romanek et al., 1994; Usui et al., 2010, 2012; Kounaves et al., 2014; Kurokawa et al., 2014). This knowledge can and should be complemented with information of meteorite impact event and condition of passage through the atmosphere that can be obtained from glass phases.

Detailed explanations of local structures of Ca, Fe, Ti and Zr were provided in chapters 1.6 and 1.7. The result of previous local structure analyses of Ca, Ti, Fe and Zr for glassy materials showed that local structures in glass phase reflect the formation conditions of each material. Therefore, local structures of these atoms in glass phase of meteorite also retains information about the formation conditions. Comparing the local structures between glass phase of meteorite and natural glasses, we estimate the formation conditions of meteorites.

5.2. SAMPLE AND EXPERIMENTS

In order to study the local structures around Ca, Ti, Mn and Fe atoms in the fusion crusts of Tissint meteorite (shergottite, Morocco), L5 chondrite (unnamed, North African), Dar al Gani 456 (L6 chondrite), millbillillie (Eucrite achondrite) and Allende (CV3 carbonaceous chondrite), we prepared several reference materials such as tektites,

impact glasses, volcanic glasses, zircon and baddeleyite. The Ca, Ti and Fe K-edge XAFS measurements were performed at beam line BL-9C, equipped with Si (111) double-crystal monochromator and Zr K-edge XAFS measurements were performed at beam line BL-NW10A, equipped with Si (311) double-crystal monochromator, of the Photon Factory, KEK, Tsukuba, Japan.

5.3. RESULTS AND DISCUSSION

Figure 5.1 shows XANES and EXAFS spectra of Ti in fusion crusts and reference material. Ti XANES spectra in each fusion crust have similar shape. Comparison with previous studies of the local structures of Ti in natural glasses (Wang et al., 2011, 2013a) shows that Ti XANES spectra of fusion glass are similar to that of Darwin glass. Detailed pre-edge features of Ti XANES of fusion crusts, such as pre-edge intensity and peak position, depend on the type of meteorite. This difference may originate in different formation conditions such as velocity and/or size of the meteorite. Local structures of Ti in fusion crust may convey a clue about the formation conditions of fusion crust.

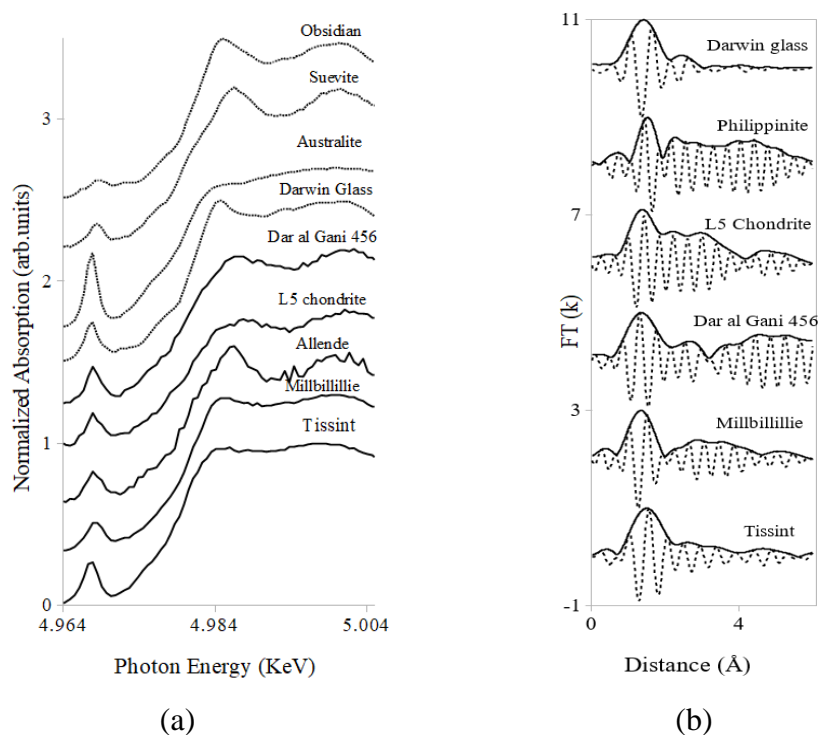


Figure 5.1. Experimental Ti XANES (a) and EXAFS (b) spectra in fusion crust and reference material. In figure 5.2 (a), solid line and dotted line show fusion crust and reference material, respectively.

Table 5.1. Structural parameters of Ti determined by EXAFS. Coordination number is estimated by Shannon ionic radii (Shannon, 1976).

Sample	Estimated Coordination number	Ti-O distance (Å)	R-factor (%)
Tissint	5 and 6	1.916 (4)	5.4
Millbillillie	5 and 6	1.921 (4)	2.5
L5chondrite	5	1.907 (1)	3.8
Dar al Gani	5	1.903 (1)	2
Darwin glass	5 and 6	1.963 (4)	0.2
Philippinite	5 and 6	1.921 (5)	2.7

Figure 5.2 shows XANES and EXAFS spectra of Zr in Tissint meteorite and reference material. The XANES and EXAFS spectra of Zr in the inner glass part of Tissint is similar to baddeleyite and fulgurite; in other words, the inner glass part of Tissint has baddeleyite-like Zr local structures. According to Tobase et al. (2015b), local structures of Zr can be classified as zircon-like, baddeleyite-like and glass-like types, as described in chapter 3. On the basis of local structure similarity between inner glass part of Tissint, fulgurite and baddeleyite, the formation temperature of inner glass part of Tissint should be similar to that of fulgurite and baddeleyite. Therefore, the formation temperature of the inner glass part of Tissint is estimated to be in the range 1680-2000 °C, which is in good agreement with the temperature (~2000°C) proposed by Baziotis et al. (2013). We conclude that the inner glass part of Tissint formed by meteorite impact on Mars.

On the other hand, the local structures of Zr in fusion crust of Tissint meteorite is similar to tektites (glass-like type) and suevite (zircon-type). In the Zr XANES spectra of fusion crusts a shoulder is observed around 18.0141 (1) KeV. According to Tobase et al. (2015b), glass-like Zr local

structures have characteristic second peak of Zr XANES around 18.014 KeV. Therefore, the shoulder observed in the Zr XANES spectra of fusion crusts suggests the occurrence of glass-like Zr local structures. From this, we conclude that the local structures of Zr in fusion crust of Tissint is of glass-type, rather than zircon-type. Kimura et al. (2003) showed that fusion crusts were formed from the bulk of meteorite when it experienced high temperature and low pressure during the passage into the atmosphere. During the formation of fusion crusts, baddeleyite-like Zr local structures in the inner part of Tissint changed to glass-like. The ZrO_2 - SiO_2 phase diagram suggests that the formation temperature of glass-like Zr local structures is higher than that of baddeleyite-like one. According to Tobase et al. (2015 a, b), glass-like Zr local structures is estimated to be formed in high temperature and rapid quenching conditions. A small shoulder around 18.1041 (1) KeV in Zr XANES spectra of fusion crusts suggests that local structures of Zr in fusion crusts change from the baddeleyite-like Zr in the surface of meteorite to the glass-like one during the passage into the atmosphere. Based on the information obtained from the Tissint meteorite, we suggest that the local structure analyses of Zr in the inner glass part and fusion crust part of meteorite may provide a clue to the condition of meteorite impact on Mars and the passage of the meteorites through the Earth atmosphere.

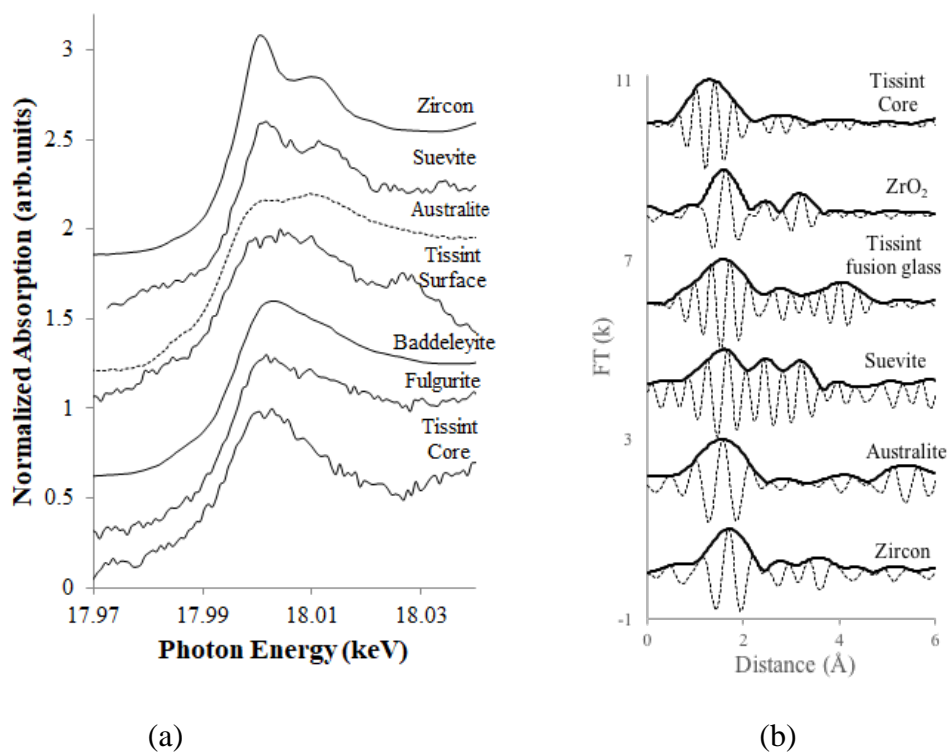


Figure 5.2. Experimental Zr XANES (a) and EXAFS (b) spectra in Tissint and reference materials. In figure 5.2 (a), XANES spectra in fusion crust and reference material are shown in solid line and dotted line, respectively.

Table 5.2. Structural parameters of Zr determined by EXAFS. Coordination number is estimated by Shannon ionic radii (Shannon, 1976).

Sample	Estimated	Zr-O distance (Å)	Zr-O distance (Å)	R-factor (%)
	Coordination number	by XRD	by XAFS	
Tissint Fusion glass	7.6	—	2.235 (2)	4.31
Tissint Core	7.2	—	2.209 (1)	10.4
ZrO ₂	7	2.04-2.24	2.193 (3)	6.11
Australite	7.5	—	2.215 (5)	0.14
Suevite	7.7	—	2.218 (4)	3.62
Zircon	8	2.13-2.26	2.226 (6)	0.26

The Ca XANES spectra and EXAFS spectra in meteorite fusion crusts are shown in figure 5.3. The Ca XANES spectra in meteorite fusion crust are unique and have various pre-edge and shoulder intensities. The pre-edge peak observed in Dar al Gani 456 has the highest intensity, which indicates that Ca site symmetry in Dar al Gani 456 is lower than that in other meteorites (Neuvill et al., 2004). On the other hand, on the basis of the pre-edge intensity, Ca site symmetry around Ca in millbillillie is higher than in other meteorites. The shapes of XANES spectra of the fusion crusts are similar to those of tektites (Tobase et al., 2013), although the detailed shapes are different, especially in the shoulder intensity. This intensity is affected by the silicon contents (Neuvill et al., 2004); a decrease of shoulder intensity indicates that Si content in fusion is lower, due to volatilization of Si at fusion crust during the passage into the atmosphere. Structural parameters of Ca in fusion crust obtained from EXAFS spectra are shown in table 5.3. The Ca-O distances in meteorite fusion crust are 2.40-2.45 Å, which are similar but slightly longer than those in tektites. The XANES and EXAFS spectra of fusion crusts suggest the latter experienced high temperature and high pressure similar to the formation conditions of tektites. The difference of local structures of Ca in fusion crusts and tektites should come from volatilization of volatile component during the passage in the atmosphere.

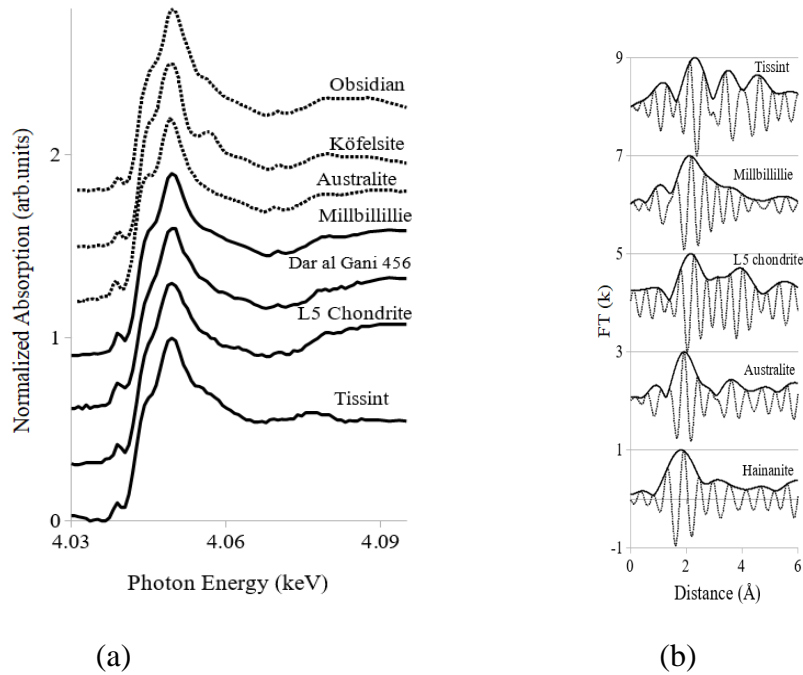


Figure 5.3 Experimental Ca XANES (a) and EXAFS (b) spectra in fusion crusts and tektites. In figure 5.3 (a), solid line and dotted line show fusion crust and reference material, respectively.

Table 5.3 Structural parameters of Ca determined by EXAFS.

Sample	Estimated coordination number of Ca	Ca-O distance (Å)	R-factor (%)
Tissint	7	2.397 (9)	2.4
Millbillillie	7	2.427 (18)	0.8
L5 Chondrite	7.5	2.445 (10)	0.4
Hainanite	7	2.400 (19)	0.1
Australite	7	2.419 (23)	1.6

Figure 5.4 shows Fe XANES and EXAFS spectra in fusion crust and reference material. The Fe XANES spectra of fusion crusts are different from any other impact-related glasses (Wang et al., 2013b). Main Fe absorption edge energy and threshold energy reflect oxidation state of Fe (Okudera et al., 2012). Threshold energy of target atom is defined as the maximum peak position in the dXANES (described in chapter 1.5) profile (figure 5.4b). Threshold energies at 7119.21 (1) eV of each fusion crust

are higher than that of moldavite-green which is produced under lower oxidation conditions and lower than that of impact glasses which are produced under normal oxidation conditions such as the surface of Earth. Threshold energy of fusion crust indicates that it was formed at high altitude in the atmosphere.

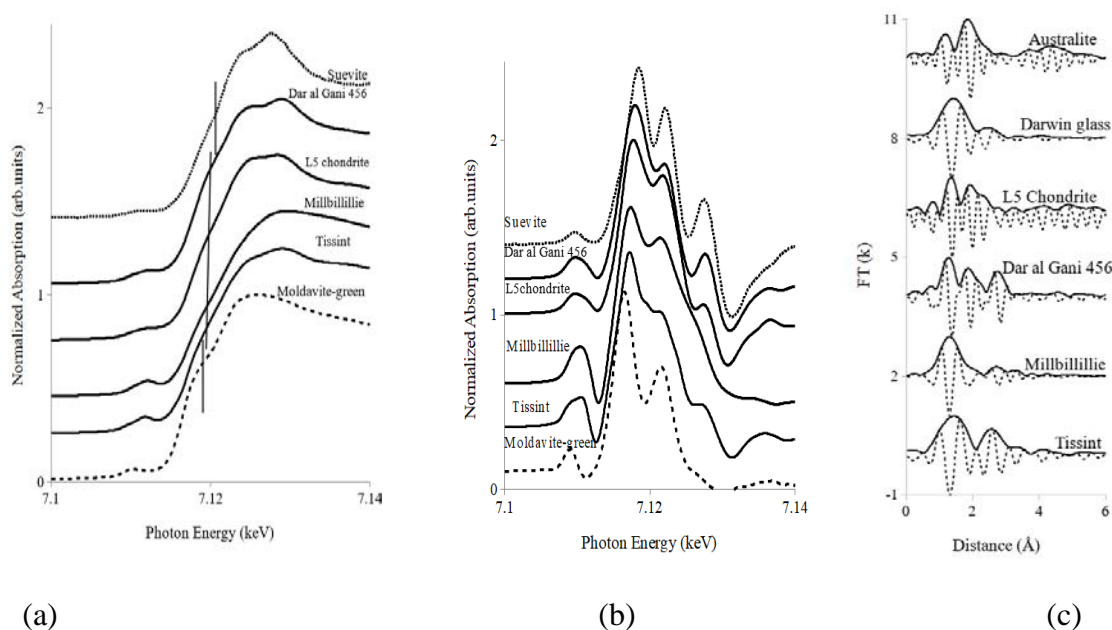


Figure 5.4. Experimental Fe XANES (a), dXANES (b) and EXAFS (c) spectra in fusion crust and reference material. In figure 5.4 (a), XANES spectra in fusion crust, tektites and natural glasses are shown by solid a line, dashed line and dotted line, respectively. Vertical line (a) shows threshold energy of fusion crust.

Table 5.4. Structural parameters of Fe determined by EXAFS.

Sample	Estimated coordination number of Fe	Fe-O distance (Å)	R-factor (%)
Tissint	6	1.996 (20)	0.1
Dar al Gani 456	6	2.016 (17)	0.7
Millbillillie	5	2.057 (11)	0.5
L5 chondrite	5	2.086 (12)	9.4
Darwin Black	6	2.001 (13)	0.1
Moldavite-Green	6	2.029 (10)	0.1

Chapter 6

**High temperature diffraction
experiments and phase diagram in
the system $\text{ZrO}_2\text{-SiO}_2$**

6.1. INTRODUCTION

ZrSiO₄, zircon, is a refractory mineral that melts incongruently into ZrO₂ + SiO₂ at the 1673(±10) °C. The phase diagram of the SiO₂-ZrO₂ system was proposed by Buttermann and Foster (1967). In the SiO₂-ZrO₂ system, a two liquids immiscibility gap was proposed between 2250 °C and 2430 °C by Curtis and Sowman (1953), although the origin of these data was uncertain. The existence of two immiscible liquids has not been reported in Toropov and Galakov (1956). In general, it is considered that the existence of two liquid phases disappears at high temperature due to severe thermal motion. The experimental coexistence of two liquids was not confirmed in the literature.

Zircon is the oldest identified mineral formed at the initial stage of the Earth's crust activity. The oldest zircon found from Mt Narryer and Jack hills, Western Australia, was formed 3.9-4.4 billion years ago (Compston and Pidgeon 1986; Maas et al., 1991). Zircon is an important refractory material due to its low coefficient of thermal expansion, high thermal shock resistance, resistant to weathering; it is also an important rock mineral. Zircon showed specific structure change under high pressure, high temperature and shocked compression conditions (Liu, 1979; Mashimo et al., 1983; Kusaba et al., 1983; Subbarao et al., 1990; Murgic et al., 1992; Kaiser et al., 2008). In shock experiments a phase transition was observed from zircon to the scheelite-type structure under static pressure (Reid and Ringwood, 1969) and shock induced condition (Kusaba et al., 1983). A systematic trend in the thermal expansion coefficients was explained performing high temperature experiment (Subbarao et al., 1990). Natural zircons are affected by metamictization which is caused by radioactive decay of, mainly, U and Th atoms substituting Zr in the structure. Mursic et al. (1992) reported recrystallization phenomena from metamict zircon at high temperature. Because zircon is resistant to weathering and records structure changes under extreme conditions, clues to the extreme environment in the history of the Earth such as meteorite impacts may be obtained from investigating the structure changes at higher

temperature and the phase relationship in the high temperature region of the $\text{SiO}_2 - \text{ZrO}_2$ system.

ZrO_2 , baddeleyite, is one of the major components of modern ceramic materials such as super ionic conductors. Its high-temperature polymorphs, tetragonal and cubic ZrO_2 , have been extensively studied and used by the industry. Recently, phase transitions of ZrO_2 under high pressure has gathered much interest in both material and geophysical researches (Ohtaka et al., 1991, 2001, 2005; Leger et al., 1993; Yashima et al., 1996; Bouvier et al., 2002). ZrO_2 is monoclinic at ambient conditions. At ambient pressure, two high-temperature phases of ZrO_2 have been found; namely a tetragonal structure, space group-type $P4_2/nmc$, and a cubic fluorite-type structure, space group-type $Fm\bar{3}m$. The investigation of high-pressure polymorphism of ZrO_2 is also important for its geophysical implications. There is no recent report on detailed structural analysis on pure ZrO_2 nor on the temperature dependence of unit cell volume near the transition point from the tetragonal to the cubic phase.

In this chapter, we report results of high-temperature X-ray diffraction and dissolution experiments of ZrSiO_4 and ZrO_2 powder to confirm the phase diagram. As ZrO_2 has an extremely high melting point (2715 °C), the difficulties at high temperatures lead to problems in selecting suitable container materials that avoid contamination effects. The structural analysis of glass with high solidification points has advanced significantly with the invention of the levitation technique (Kohara and Suzuya, 2001; Kohara et al., 2007), especially in combination with diffraction techniques. A two-dimensional imaging plate detector was used for short-time observations; diffraction data in a wide area were projected in one dimensional for Rietveld analysis, as large-grain growth occurred at high temperatures. IP detector is high sensitive to X-ray and used for rapid collection of full powder diffraction patterns. Imaging plate detector has been used extensively for high-temperature powder diffraction (Mezouar et al., 2002). The cell parameters and cell volumes of ZrSiO_4 and ZrO_2 were investigated by means of in situ observation using laser heating and

synchrotron radiation. Pure ZrO_2 sintered spheric samples were heated up to 2710 °C. The phase diagram will be proposed based on high temperature diffraction experiments and quantitative chemical analyses of quench glass for melted ZrSiO_4 sample obtained in the interval 1700-2400 °C.

6.2. SAMPLES AND EXPERIMENTS

6.2.1. Sample preparation

We used ZrSiO_4 and ZrO_2 powder reagents of 99% purity powders (Furu-uchi Chem. Ltd). For diffraction experiments, the pure ZrSiO_4 powder, pure ZrO_2 powder, ZrSiO_4 -platinum mixture and ZrO_2 -platinum mixture were used, where the weight ratio of mixed platinum powder was 20%. The pure powders and mixtures were pressed into cylindrical shape and sintered at 1400-1550 °C for 24 hours. The sintered samples were shaped into a sphere with a diameter of 2 mm.

6.2.2. High-temperature diffraction experiments using laser heating and levitation technique

High-temperature angular dispersive diffraction experiments of ZrSiO_4 and ZrO_2 were carried out at the BL04B2 beamline at the SPring-8 synchrotron radiation facility, using the laser heating and aerodynamic levitation technique as shown in figure 6.1 (Kohara and Suzuya, 2001; Kohara et al., 2007). The energy of the incident X-rays was 61.4 KeV. Each diffraction was measured within about 3 minutes to avoid grain growth at high temperature. A two-dimensional IP detector was used and diffraction profiles in wide azimuth angle were projected onto one dimension for Reitveld analysis. Using a Rietveld analysis program (Izumi et al., 1987), we simulated powder diffraction pattern of each specimen. The sample was set in a shallow nozzle where it was aerodynamically levitated. The levitated sample was then heated by a 100-W CO_2 laser. The temperature of the sample was monitored by a two-colour pyrometer. The temperature was calibrated using the melting temperature of ZrO_2 (2715 °C) and Al_2O_3 (2072(10) °C). Platinum was also used for temperature calibration for diffraction experiments in the medium

temperature range. The unit-cell parameters and volumes of pure ZrSiO_4 and tetragonal and cubic ZrO_2 were determined as a function of temperature using a laser heating technique.

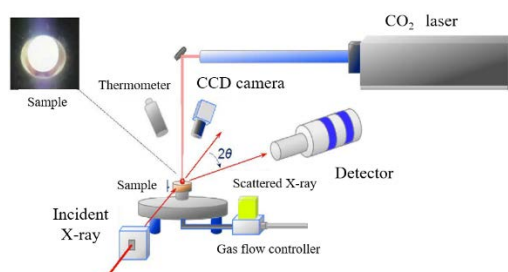


Figure 6.1. Schematic of laser heating gas flow experiment in Spring-8, BL04B2.

6.2.3. Preparation of quenched sample and chemical analyses, XAFS analyses

Quenched glass samples for ZrSiO_4 melt were prepared using the same high-temperature laser heating and gas flow technique in Spring-8, BL04B2. This experiment was carried out by non-container method. After heating, the glass samples were obtained by dissolving and maintaining the target temperature for 3-5 minutes and quenching to room temperature. The temperatures were changed from 1700 to 2400 °C in steps of 100 °C.

Quantitative analyses of quenched glass samples were carried out by a JEOL SEM JSM-7001F scanning electron microscope (15 kV, 1.0 nA) and an Oxford energy dispersive X-ray spectrometry (EDS) INCA SYSTEM energy dispersive X-ray analyzer. The total quantitative values were close to 100% and total values between 101% and 97% are used as analysis values. The total quantitative value of detected Zr and Si atoms is analyzed as ZrO_2 and SiO_2 , respectively. The electron beam size for EDS analyses is 1 μm . When analytical region of sample is close to the beam size, the influence of fluorescent X-ray from the surrounding component may occur.

XAFS method was described in chapter 2. XAFS analyses were performed by transmission mode in PF NW10A, KEK, Tsukuba.

6.3. RESULTS AND DISCUSSION

6.3.1. Temperature dependence of cell parameters and phase transition in ZrSiO₄ and ZrO₂

The cell parameters, thermal expansion and c/a ratio for ZrSiO₄ (space group-type $I4_1/amd$ and $Z=4$) and tetragonal ZrO₂ (space group-type $P4_2/nmc$ and $Z=2$) are obtained under high temperature. Discontinuous change in cell parameters for ZrSiO₄ is not observed (figures 6.2, 6.3 and 6.4). The c/a ratio for ZrSiO₄ increases with increasing temperature (figure 6.5). The thermal expansion coefficient in the a -axis direction is smaller than that in the c -axis direction. The increase rates of the volumes of ZrSiO₄ and ZrO₂ is 0.11 and 0.13 $\text{\AA}^3/_{100^\circ\text{C}}$, respectively. The thermal expansion coefficient along the a -axis in ZrSiO₄ is especially small. Unit cell parameters for ZrO₂ have discontinuous change (figures 6.6 and 6.7). Thus, ZrSiO₄ and ZrO₂ have different thermal expansion characteristics. It can be inferred that the two-phase sintered material is probably weak against thermal stress.

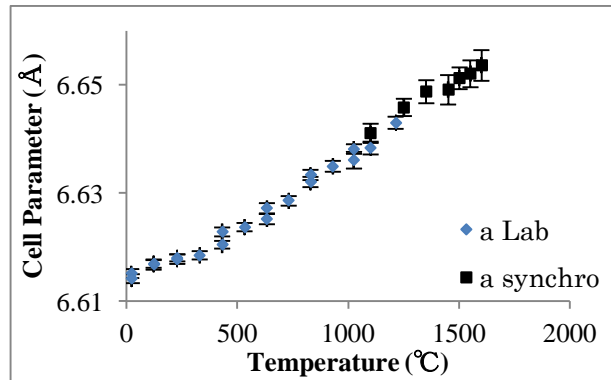


Figure 6.2. Temperature dependence of cell parameter a for ZrSiO₄.

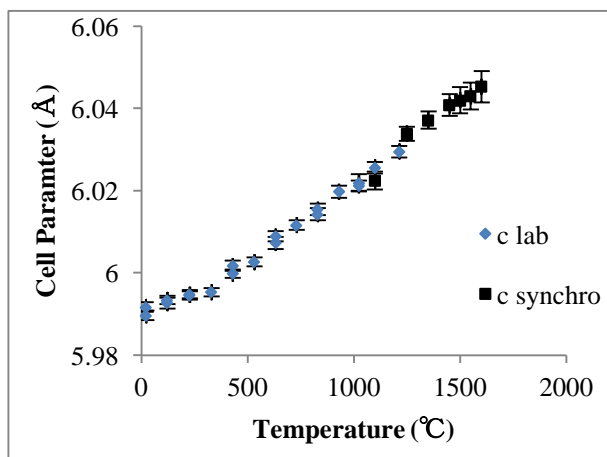


Figure 6.3. Temperature dependence of cell parameter c for ZrSiO_4 .

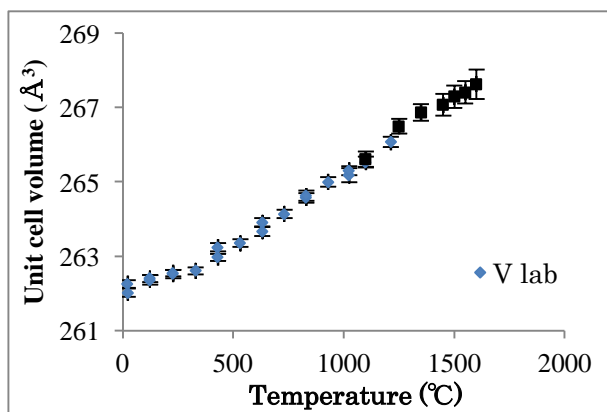


Figure 6.4. Temperature dependence of unit cell volume for ZrSiO_4 .

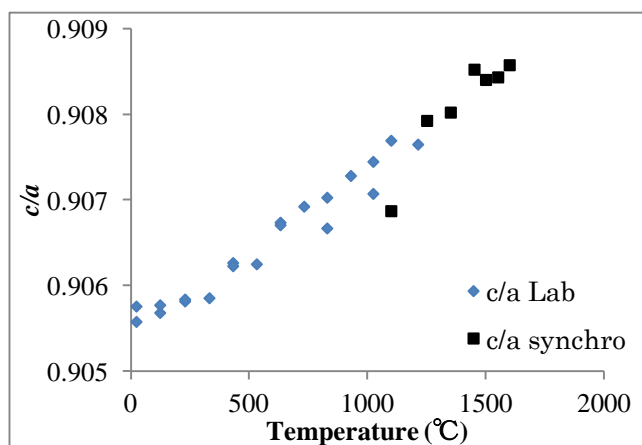


Figure 6.5. Temperature dependence of c/a ratio for ZrSiO_4 .

The transition temperature of ZrO_2 from the tetragonal phase to the cubic phase is specified between 2430 and 2540 °C (figures 6.6, 6.7 and

6.8). A precursor phenomenon for the transition becomes clear from around 2200 °C (figures 6.6, 6.7 and 6.9). Thermal expansion coefficient of the a -axis increases and contraction of the unit cell parameter of c -axis occurs around 2200 °C (figures 6.6 and 6.7). Unit cell volume shows a discontinuity at the transition point from the monoclinic to the tetragonal phase. This is the reason why the monoclinic-tetragonal phase boundary has a negative slope on the P-T phase diagram (Ohtaka et al., 2005). On the contrary, no clear unit cell volume change was observed at the transition point from the tetragonal to the cubic phase. We propose from this observation that the phase boundary from the tetragonal to the cubic phase does not have a negative slope on the P-T diagram, contrary to the P-T diagram of ZrO_2 proposed so far. In situ high-pressure and high-temperature experiments (Ohtaka et al., 2005) revealed that the tetragonal phase is stable up to the melting temperature below 12.5 GPa and there is no cubic phase in the high-temperature regime. The stoichiometric ZrO_2 does not take a cubic structure up to the melting temperature under high pressure. On the contrary to high pressure, the tetragonal to cubic phase boundary most probably has a positive slope under atmospheric pressure.

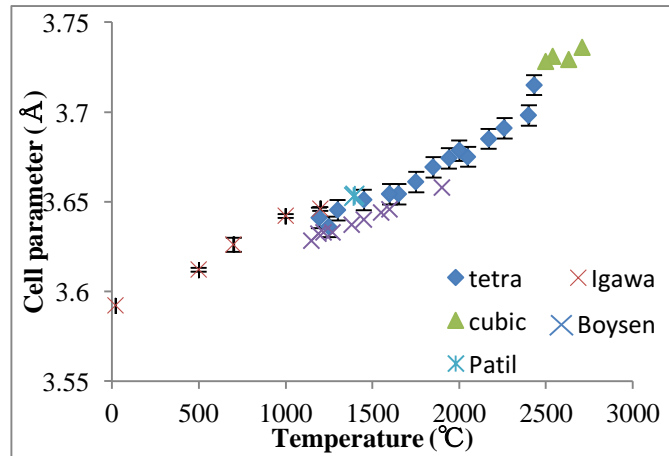


Figure 6.6. Temperature dependence of cell parameter a for pure ZrO_2 . (\diamond) and (\triangle) in tetragonal and cubic phase of ZrO_2 , respectively. Other data is used from previous study of ZrO_2 (Patil and Subbrao, 1969; Boysen and Frey, 1991; Igawa and Ishii, 2001).

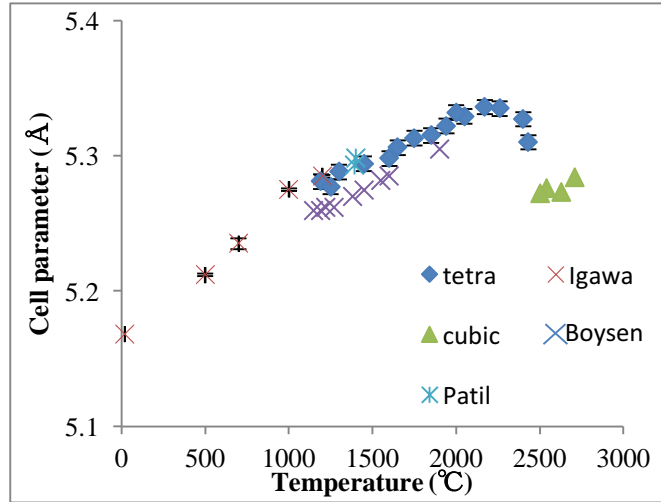


Figure 6.7. Temperature dependence of cell parameter c for pure ZrO_2 . (\diamond) and (\triangle) is tetragonal and cubic phase of ZrO_2 , respectively. Other data is used from previous study of ZrO_2 (Patil and Subbrao, 1969; Boyesen and Frey, 1991; Igawa and Ishii, 2001).

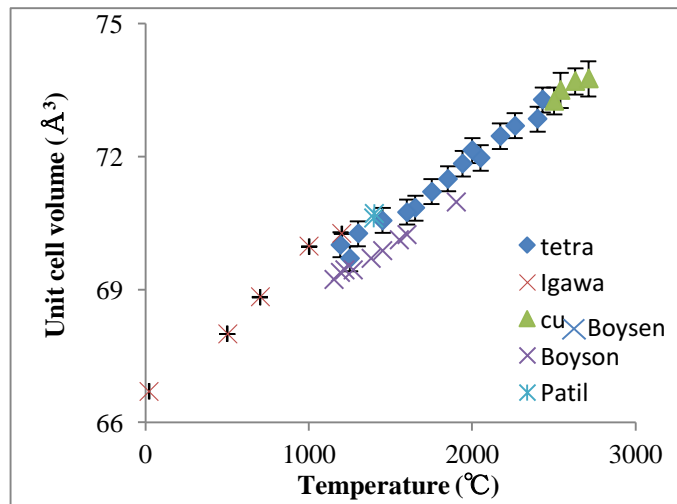


Figure 6.8. Temperature dependence of unit cell volume for pure ZrO_2 . (\diamond) and (\triangle) in tetragonal and cubic phase of ZrO_2 , respectively. Other data is used from previous study of ZrO_2 (Patil and Subbrao, 1969; Boyesen and Frey, 1991; Igawa and Ishii, 2001).

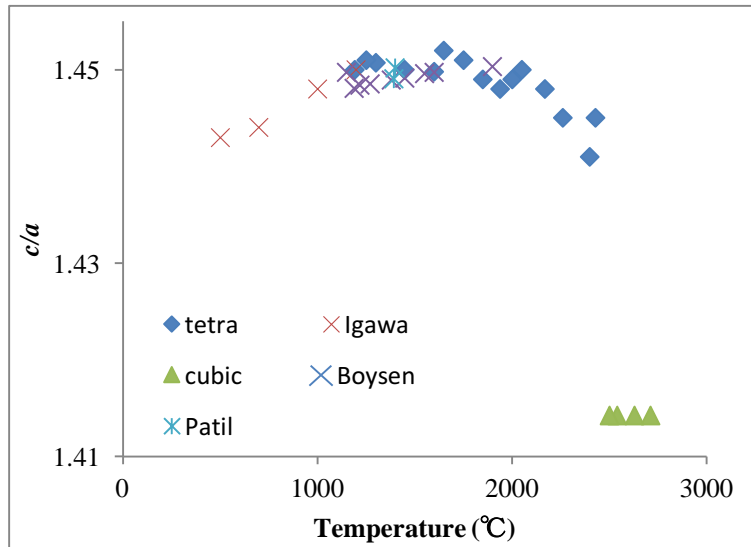


Figure 6.9 Temperature dependence of c/a ratio for pure ZrO_2 . (\diamond) and (\triangle) in tetragonal and cubic phases of ZrO_2 , respectively. Other data are taken from previous study of ZrO_2 (Patil and Subbrao, 1969; Boysen and Frey, 1991; Igawa and Ishii, 2001).

6.3.2. Chemical composition and phase diagram in the ZrO_2 - SiO_2 system

A SEM image of the sample quenched from 1800 °C is shown in figure 6.10. The volume ratio of glass is relatively low in the lower temperature region after melting of zircon, whereas the volume ratio of ZrO_2 crystals is relatively high. The glass regions in the samples were less than 10 μm in width (figure 6.11). As described in the experimental part, the electron beam size for EDS analysis is 1 μm . The X-ray excitation region of the analytical point is larger than the beam size. Since the size of many measured points are around 5 μm , the influence of fluorescent X-ray from the surrounding ZrO_2 gives a higher content of ZrO_2 than the real value, depending on the location. The analytical ratio of $SiO_2/(ZrO_2+SiO_2)$ at each temperature is shown in table 6.1. The analytical ratios are added in the phase diagram of Buttermann and Foster (1967) reproduced in figure 6.12. The analytical value with the highest Si content at each temperature below 2200 °C is consistent with the liquidus curve. Considering the

reaction time of solid and liquid and the effect of X-ray fluorescence from the surrounding ZrO_2 , almost the same liquidus curve can be drawn between 1700 and 2200 °C. At 2300 and 2400 °C, we could not observe any liquid immiscible area. The highest Si contents in glass are 53.3 and 49.1% for samples quenched from 2300 and 2400 °C, respectively, except for one outlier at 88.4%. Both values of 53.3 and 49.1% are in the alleged two liquid immiscible area. The liquidus line in our phase diagram is basically consistent with the phase diagram proposed by Buttermann and Foster (1967) without the two liquids immiscible region. The Si content of 88.4% seems anomaly high. This analytical point lies on the rim nearest the surface of the sample where bubbles formed by volatilization of SiO_2 are observed in the glass quenched from 2300 °C (figure 6.12). A local inhomogeneity in composition near the surface of glass and bubble texture were observed in the sample quenched from 2300 °C.

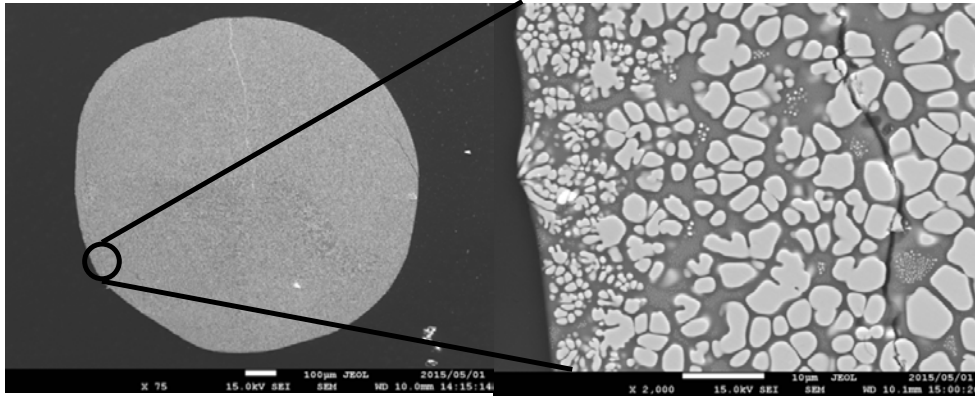


Figure 6.10. SEM image of the quenched glass sample from $ZrSiO_4$ melt at 1800 °C. Dark areas are glass and bright areas are ZrO_2 crystals.

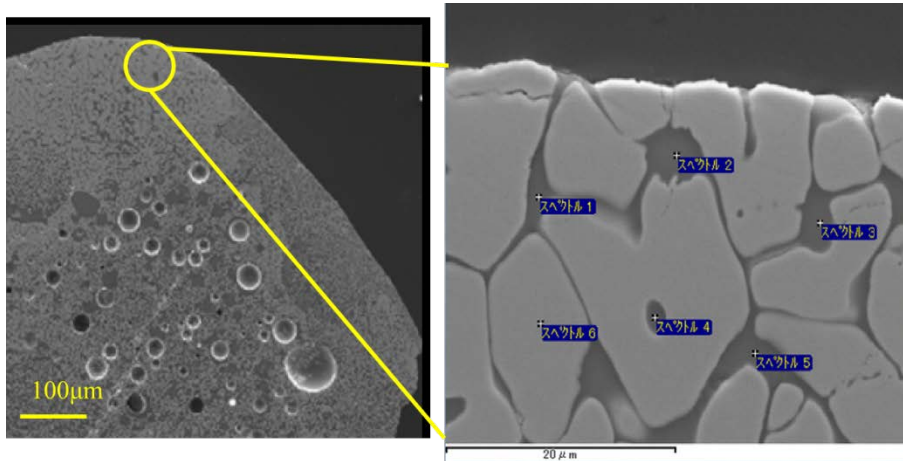


Figure 6.11. SEM image of sample quenched from 2300 °C. The arrow shows an analytical point with anomaly high Si content (88.4%), which lies on the rim nearest the surface of sample. Bubbles formed probably by volatilization of SiO₂ are observed in the glass quenched.

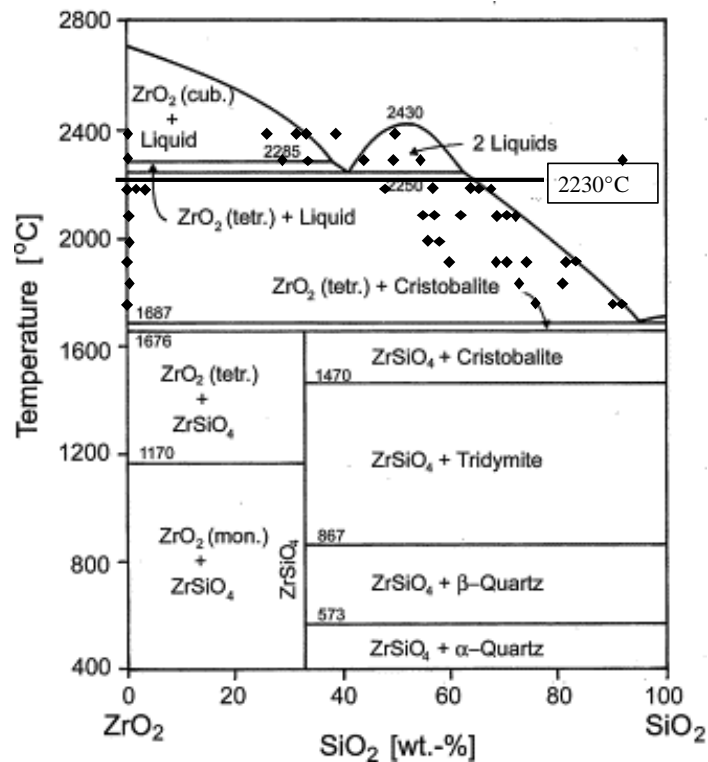


Figure 6.12. the SiO₂-ZrO₂ phase diagram proposed by Buttermann and Foster (1967). Vaporization temperature of SiO₂ (2230 °C) is shown in horizontal line. Each ◆ represents chemical composition of quenched glass.

Table 6.1. The $\text{SiO}_2/\text{ZrSiO}_4$ ratio of sample in each temperature. These ratios are obtained from same samples in each temperature. Difference of ratio of $\text{SiO}_2/(\text{ZrO}_2 + \text{SiO}_2)$ is estimated to be affected from fluorescent X-ray from the surrounding component because the size of the electron beam for EDS is larger than grain size.

Temperatures ($^{\circ}\text{C}$)	Ratio of $\text{SiO}_2/(\text{ZrO}_2+\text{SiO}_2)$ (%)							
2400	49.1	38.6	32.7	31.9	28.0	0.0	0.0	
2300	44.0	47.6	53.3	88.4	48.3	33.2	29.8	
2200	67.3	49.9	64.0	66.5	58.0	3.5	1.0	
2100	70.4	73.6	66.7	71.5	63.9	75.6	69.9	
2000	60.2	59.2	0.0					
1900	71.0	73.9	61.3	81.1	76.7	76.7	82.6	
1800	72.1	81.0	0.0	0.0				
1700	90.6	91.4	78.8					

The volatilization temperature of SiO_2 is 2230°C . It is probable that the vaporization of SiO_2 component affects the quenched glass composition at temperatures above 2230°C ; we could not confirm the existence of the two liquids immiscible region. Therefore, vaporized SiO_2 component of the sample was estimated to move from the inner to the outer side and be trapped in there. At temperatures above 2230°C , heterogeneity in liquid due to the evaporation of the SiO_2 component will occur and will depend on the experimental methods. The previously reported two liquid immiscibility gap in the temperature range of $2250\text{-}2430^{\circ}\text{C}$, which is higher than vaporization temperature of SiO_2 , may have been the reflect of compositional fluctuations in glass due to volatilization of SiO_2 component from liquid. We propose a new $\text{ZrO}_2\text{-SiO}_2$ phase diagram (figure 6.13), which is redrawn on the basis of the data of tetragonal-cubic ZrO_2 transition point and chemical analyses of quenched glass.

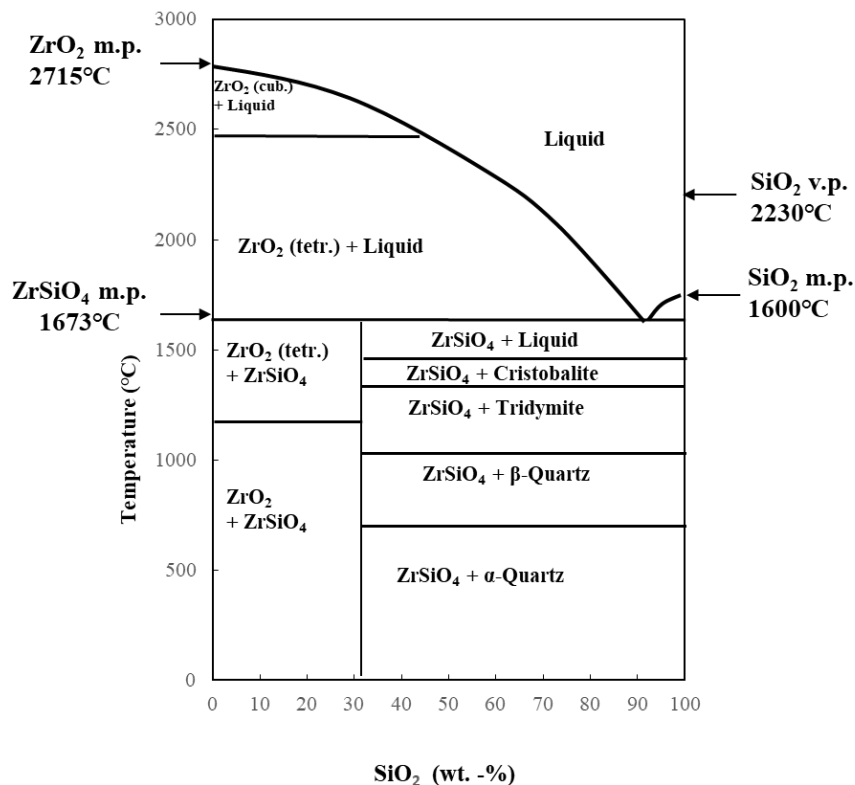
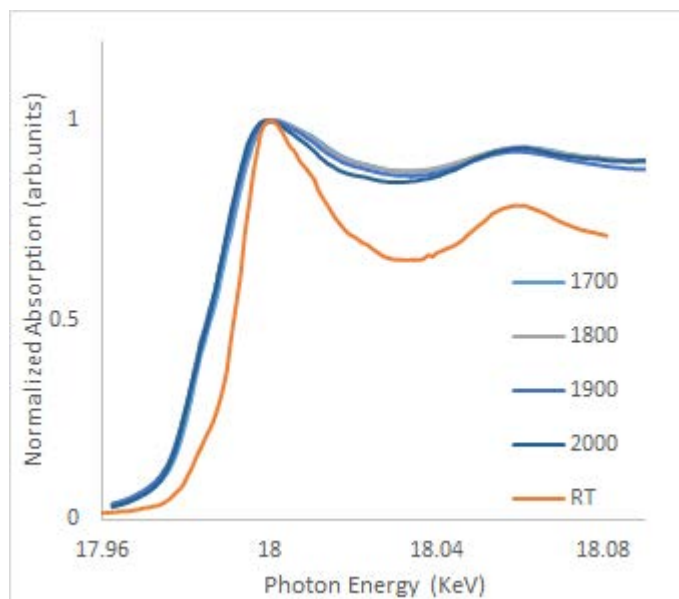


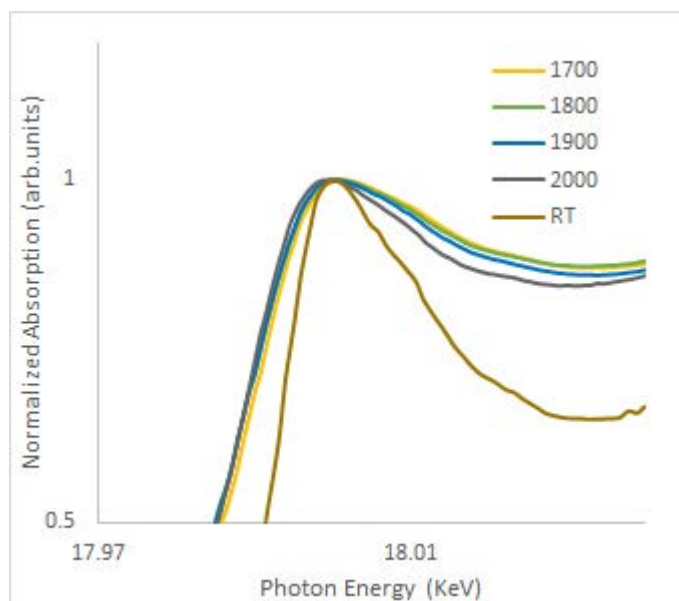
Figure 6.13. Proposed phase diagram in the system of $\text{SiO}_2\text{-ZrO}_2$. m.p. is the melting point and v.p. is the vaporization point.

6.3.3. XAFS analyses of the quenched sample

Figure 6.14 (a) and (b) show K-edge XANES spectra of zircon sample quenched from high temperature. These spectra are similar to those in baddeleyite (Tobase et al., 2015b), indicating that quenched zircon is decomposed into ZrO_2 and SiO_2 at 1700°C . Figure 6.14 (b) shows that the main peak of Zr XANES spectra slightly shifts to low energy at higher temperature. Similar phenomena were observed $\text{Sr}_{0.9}\text{Yb}_{0.1}\text{ZrO}_3$ in the middle temperature region (Okube et al., 2005). Main peak shift of XANES spectra of Zr also occurs of high temperature. Moreover, main peak shift was observed at high pressure (Yoshiasa et al., 2009). High temperature and high pressure XAFS measurements show that the local structures of Zr records information about formation conditions such as temperature and pressure.



(a)



(b)

Figure 6.14 XANES spectra of Zr in quenched zircon of room temperature and 1700 to 2000 °C.

Chapter 7

Temperature dependence pre-edge peak intensities in XANES spectra

7.1. INTRODUCTION

XANES spectra provide information about the coordination environment around an X-ray absorbing atom such as coordination number and disorder of local structure. The pre-edge peaks appear at the K-edge of transition metal elements (Groot et al., 1989) and these peaks are located several eV before the main absorption edge. The pre-edge features of transition elements are related to the coordination number, oxidation state and to the site symmetry of the absorbing atom (Yamamoto, 2008).

Temperature dependencies of the pre-edge peak intensity were observed in various compounds (Bridges et al., 2000; Durmeyer et al., 2010; Hashimoto et al., 2007; Hiratoko et al., 2013; Sato et al., 2005). Hiratoko et al. (2013) quantified linear dependence of Ti pre-edge peak features in a variety of compounds over a large temperature range. It is known that the A1 and A2 peaks in rutile-type TiO₂ show clear temperature dependence, while there is no temperature dependence for the A3 peak (Durmeyer et al., 1990, 2010). The temperature dependence of pre-edge peaks in the Ti K-edge XANES spectra had different tendencies, which is also due to the harmonic thermal vibration (Farges et al., 1996a, b, c). A sufficient comparative study and detailed interpretation of the temperature dependence of pre-edge peak intensity over a wide temperature region has yet to be conducted for several transition metal oxides.

Several XANES studies have been carried out to investigate the mechanism of ferroelectric-dielectric phase transition in BaTiO₃ and PbTiO₃ (Balzarottie et al., 1980; Miyanaga et al., 2002; Ravel and Stern, 1995; Sato et al., 2005; Sicron et al., 1994; Yoshiasa et al., 2016). Many researchers (Balzarottie et al., 1980; Miyanaga et al., 2002; Ravel and Stern, 1995; Sato et al., 2005; Sicron et al., 1994; Yoshiasa et al., 2016) clarified that the Ti ion occupies an off-center position of the distorted TiO₆ octahedral site; the geometrical distortion in the tetragonal phase decreases with increasing temperature and the A2 pre-edge peak intensity decreases characteristically. These results showed that the A2 pre-edge peak intensity in ferroelectric phase depends on the degree of distortion around the Ti atoms. Investigations of other titanium compounds showed

that the intensities of pre-edge peak are sensitive to slight changes in the asymmetry of Ti coordination sphere (Pillep et al., 1997; Waychunas, 1987).

In this chapter, we will quantify the behavior of each metal pre-edge peak in transition metal oxides (Sc_2O_3 , TiO_2 , VO_2 , Cr_2O_3 , MnO , Mn_2O_3) over a large temperature range and investigate how the intensity of pre-edge peak changes with temperature. According to Yamamoto (2008), pre-edge features of XANES spectra are sensibly affected by dipole and quadrupole transitions, as described in chapter 2. Here we will show that the temperature dependence of pre-edge peak intensities for $1s \rightarrow t_{2g}$ can be classified into the TiO_2 rutile- or anatase-types. Investigation of the changes of the pre-edge peak features can provide detailed information of temperature dependence of XANES spectra. We emphasize from the observation of temperature dependence that the difference peak D positions obtained from the difference between higher and lower temperature of XANES spectra represent the transition energies rather than the simple pre-edge peaks. Changes in pre-edge features of Ti XANES spectra are sensitive to coordination number of Ti. In the previous chapter, local structure analyses of Ti in tektite, K-Pg sediments and Martian meteorite could provide information about formation conditions of each material. Small differences in the XANES spectra bear significant information about the formation conditions of the samples: it is therefore of paramount importance to improve the accuracy of XANES analysis. Quantification of pre-edge peak in transition metal oxides can improve the accuracy of XANES analysis.

7.2. EXPERIMENTAL METHODS

We used the same specimens of TiO_2 rutile and anatase already described in chapter 4 and by Hiratoko et al (2013). All other specimens [Sc_2O_3 (99.9%), VO_2 (99.5%), Cr_2O_3 (99.9%), MnO (99.9%), $\alpha\text{-Mn}_2\text{O}_3$ (99.9%),] were commercial chemicals (Furu-uchi Chemical Co. Ltd). Appropriate amounts of fine-powder sample and boron nitride powder were mixed and pressed into pellets of <0.2 mm in thickness and 10.0 mm

in diameter. Adjusting sample content allowed all samples to show edge-jumps of 0.7 ($\Delta\mu d$), where μ is the linear absorption coefficient and d is the sample thickness. The Sc, Ti, V, Cr and Mn K-edge XANES were measured in transmission mode at beamlines BL-9C of the Photon Factory in the High Energy Accelerator Research Organization (KEK), Tsukuba, Japan. X-ray absorption measurements in the temperature range 300–900 (5) K were performed under a helium atmosphere.

In order to clarify temperature dependence in pre-edge peaks, we plotted the difference spectrum between the low temperature spectrum (400K) and the high temperature ones (500 to 800 K). In the low temperature experiment (50 to 320 K), we plotted the difference spectrum between lower temperature spectrum (50 K) and higher temperature ones (100 to 320 K). We found the existence of an energy point where the intensity does not change with temperature near each absorption edge for all samples. This point should be called the absorption intensity invariant point (AIIP) because it is not influenced by the temperature (Hiratoko et al., 2013). An arrow indicates the AIIP in the figure 7.1. The physical meaning of AIIP will be regarded as extension of EXAFS baseline. Using the AIIP peak intensity as a standard point, it is possible to present a quantitative comparison for the pre-edge peaks in various compounds in a wide temperature range. We normalized the spectrum intensity for the AIIP of all samples and compared the temperature dependence of the XANES pre-edge peaks among the samples. The AIIP-based normalization allows the elimination of errors caused by the reference point itself changing with temperature. XANES amplitudes at energies higher than the AIIP dampen with increasing temperature as a result of Debye–Waller type effects (Hiratoko et al., 2013). The AIIP standardization is effective when comparing the temperature dependence of absolute intensity in the XANES spectra.

7.3. RESULT AND DISCUSSION

7.3.1. AIIP-based normalization and Temperature dependence of XANES features

AIIP is observed near each absorption edge for all samples. Figure 7.1 shows an example of Cr K-edge XANES spectrum of Cr_2O_3 at 400 - 800K (AIIP energy: 6005.3 eV) and the difference between the spectrum at 400K and those at higher temperatures (600K-800K). XANES amplitudes are clearly seen to damp at energies higher than the AIIP owing to the Debye-Waller effect at higher temperature; the line displays a sinusoidal attenuation. Conversely, amplitudes increase with temperature at energies lower than the AIIP with several peaks in the difference spectra. Figures 7.2-7.7 show the pre-edge region in XANES spectra for each sample and the difference spectra between the lowest and those of higher temperatures. The energy positions of D1 and D2 peaks are obtained from the difference spectra between the low- and high- temperature spectra (lower section of each figure).

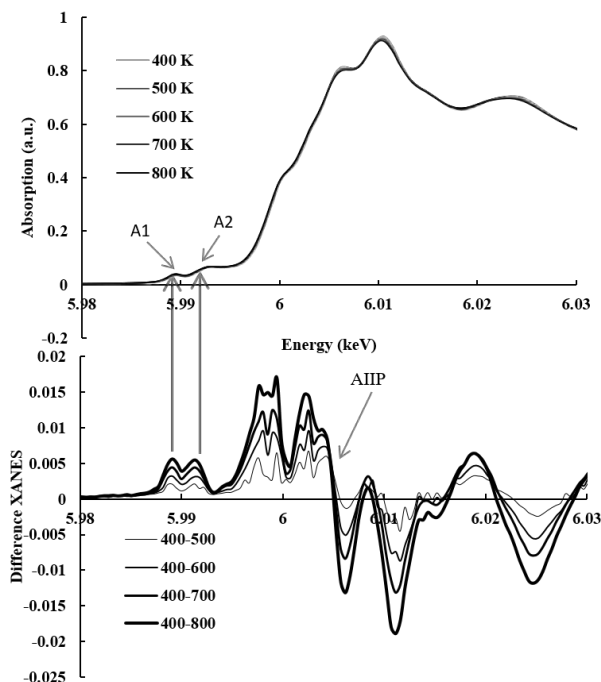


Figure 7.1. Cr K-edge XANES spectra of Cr_2O_3 at various temperature.

7.3.1.1. Temperature dependence in Sc_2O_3 and TiO_2

Figure 7.2 shows the Sc K-edge XANES spectra of Sc_2O_3 at various

temperatures. Two clear pre-edge peaks are observed. We labeled them as A1 and A2 in each peak of pre-edge region. A1 peak is assigned to the transition $1s \rightarrow 3d$ state by Bart (1986). The intensity of A2 pre-edge peak shows large temperature dependence while temperature dependence of A1 pre-edge peak is not observed.

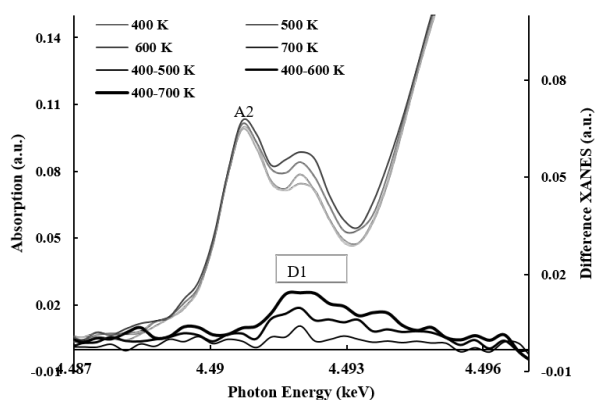


Figure 7.2. Sc K-edge XANES spectra of Sc_2O_3 at various temperature.

Figures 7.3a and 7.3b represent the Ti K-edge XANES spectra in anatase and rutile at 400-800 K and the difference between the spectrum at 400 K and those at higher temperatures (500-800 K). The A3 pre-edge peak shows no temperature dependence and the difference spectra have no magnitude in both compounds. This tendency is similar to the A1 peak in Sc_2O_3 . It is important to notice that the zero value position in the difference spectra and A3 peak position are not identical. In both anatase and rutile, the pre-edge peak positions of A2 and A3 are clearly different from the peak positions of the difference spectra. We labeled them as D1 and D2 in the figure. The features of the difference spectra for rutile and anatase are similar despite the difference of each pre-edge feature in XANES spectrum. The D2 positions correspond to the down concavity of spectrum between A2 and A3 peaks. Hiratoko et al. (2013) reported that the A2 pre-edge peaks in both compounds indicate different temperature dependence. The peaks from transitions can be separated by calculating the difference spectra. The true temperature dependence of the transition to each orbital is obtained from the difference spectra. Although the shape of A2 pre-edge peak in rutile differs from that in anatase, D1 pre-edge

peak and its temperature dependence in rutile are similar. The origin of the peak shift of XANES spectra of Ti in TiO₂ rutile and anatase can be explained by the peak position and increase of D1 peak in the difference spectra.

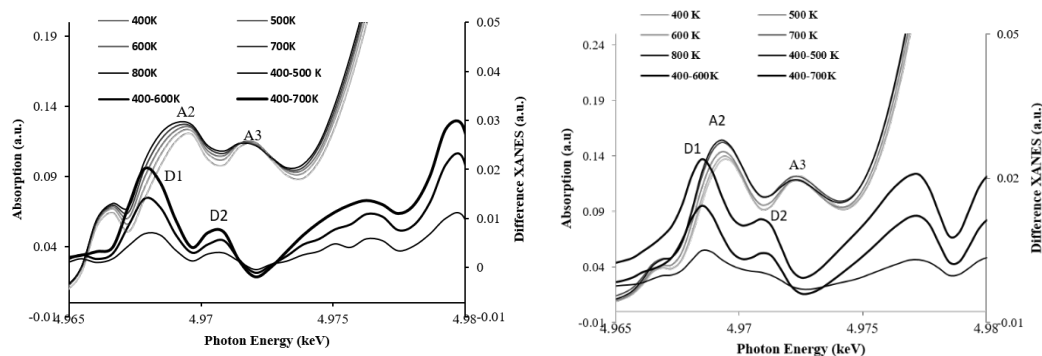


Figure 7.3. Ti K-edge XANES spectra of TiO₂ anatase (a) and rutile (b) at various temperature.

7.3.1.2. Pre-edge features and phase transition in VO₂

Figure 7.4a and 7.4b show the vanadium K-edge XANES spectra of VO₂ monoclinic phase at 50-250 K and of VO₂ tetragonal phase at 400K-700 K. VO₂ undergoes structural phase transitions from monoclinic to tetragonal at 340 K. There is a clear change in the pre-edge shape between the monoclinic and tetragonal phases (Figs 7.4a and 7.4b). Pre-edge peaks are observed in both phases with temperature dependences. In figure 7.4, the comparison of the edge structure with the calculated density state of the conduction band of VO₂ tetragonal phase (Bianconi, 1982; Gupta et al., 1977) allows us to assign A1 peak at 5467 eV to the 1s→t_{2g} transition. Absorption intensity of A2 peak in the low temperature monoclinic phase decreases discontinuously at transition point, but no energy shift of this peak is observed between monoclinic and tetragonal phases. The A1 peak is also assigned to the 1s→t_{2g} transition in monoclinic phase (Gupta et al., 1977). The features of the difference spectra of both low and high temperature phases are different, though one clear peak is observed in XANES spectrum. We label the peaks in the difference spectra in the low temperature phase as D1 and D2. The A1 peak top energies in both phases are different from the D1 or D2 peak top energies.

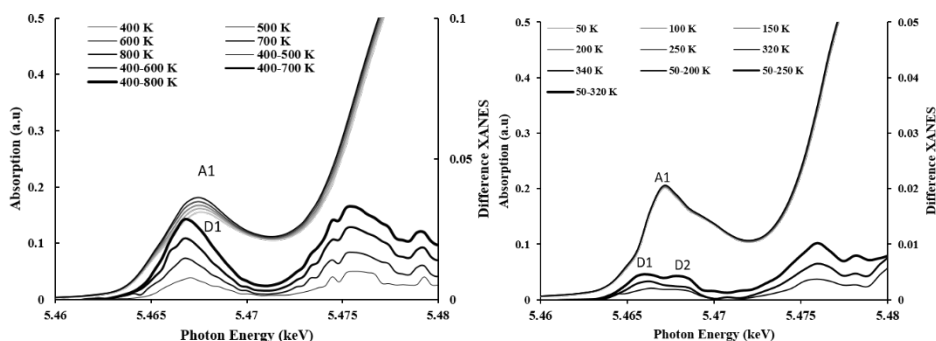


Figure 7.4. V K-edge XANES spectra of VO₂ tetragonal (a) and monoclinic (b) phases at various temperature.

7.3.1.3. Temperature dependence in Cr₂O₃, Mn₂O₃ and MnO

Figure 7.5 shows that the Cr K-edge XANES spectra of Cr₂O₃ at various temperatures. The A1 initial pre-edge peak is taken to correspond to a transition to the lowest unoccupied molecular orbital. The A1 and A2 peaks are assigned to $1s \rightarrow t_{2g}$ transition and to $1s \rightarrow e_g$ transition, respectively by Grunes (1983). Both A1 and A2 peaks in Cr₂O₃ have the same temperature dependences though peak heights are different. The energy positions of D1 and D2 peaks, which are obtained from the difference spectra between the low temperature spectra and the high temperature ones, are different from the peak tops of the pre edge peak A1 and A2 position and are located just before the peak top in the XANES spectra.

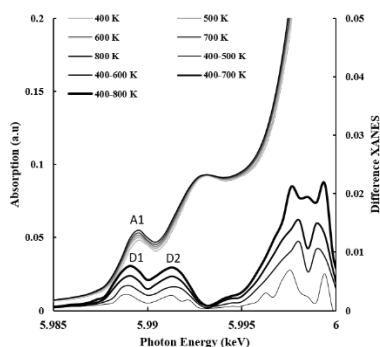


Figure 7.5. Cr K-edge XANES spectra of Cr₂O₃ at various temperature.

Figures 7.6 and 7.7 show that the Mn K-edge XANES spectra of Mn₂O₃ and MnO are at different temperatures. S1 represents the pre-shoulder.

Clear pre-edge peak is not observed but several peaks were distinguishable in the difference spectra between the low- and high- temperature spectra. Peaks are obtained by the temperature dependence of the pre-shoulder and the energy value of the electron orbit can be determined.

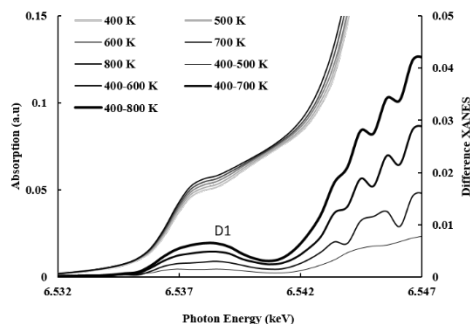


Figure 7.6. Mn K-edge XANES spectra of Mn_2O_3 at various temperature.

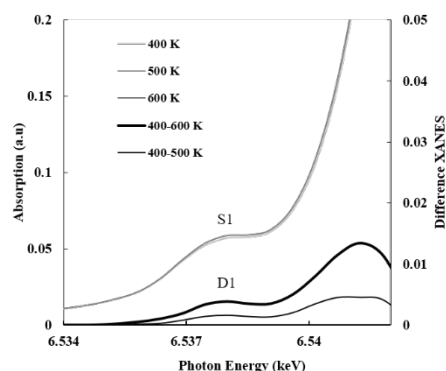


Figure 7.7. Mn K-edge XANES spectra of MnO at various temperature.

7.3.2. Increase of pre-edge intensity and gradient against temperature.

7.3.2.1. Temperature gradient for pre-edge peak intensity A.

Since AIIP-based normalization can eliminate errors due to the fact that the reference point itself changes with temperature, it is possible to compare the intensities of different compounds. Figure 7.8 shows the absorption intensity of pre-edge peak or pre-shoulder in the metal K-edge XANES spectra vs temperature (i.e. A2 peak in Sc_2O_3 , A2 peak in TiO_2 , A1 peak in VO_2 , A1 peak in Cr_2O_3 , S1 in Mn_2O_3 and S1 in MnO).

Table 7.1 shows the energy and temperature gradient of peak intensity for the pre-edge peak, pre-shoulder and D difference peak in each

compound. The A1 peak in VO₂ tetragonal phase and the A2 peak in Sc₂O₃ have temperature gradient of 0.0071 (3) and 0.0048 (3) (intensity/100K), respectively. The gradient is similar to A2 of TiO₂ rutile that is assign to 1s→t_{2g} transition. On the other hand, A1 pre-edge peak of VO₂ monoclinic phase has the same temperature dependence as A2 peak in TiO₂ anatase. The difference in the temperature dependence of the pre-edge peak of monoclinic and tetragonal phase should indicate that the vibrational character is changed by difference in local coordination environments. The rate of increase of A2 pre-edge peak intensity in Sc₂O₃, A2 in TiO₂ rutile and A1 in VO₂ tetragonal phase are large compared with the rest of the samples. Although the height of A1 peak in VO₂ monoclinic phase is obviously higher than those for A1 in VO₂ tetragonal phase and for A2 in Sc₂O₃, the temperature gradient of A1 in VO₂ monoclinic phase is clearly low, like A2 in TiO₂ anatase. Temperature dependence of the pre-edge peak is not directly related to pre-edge peak heights. Large temperature gradients are seen in low peak intensities.

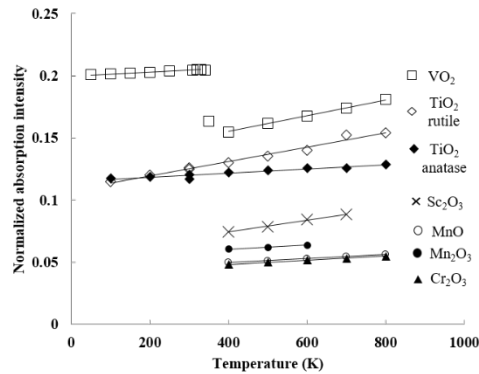


Figure 7.8. Temperature dependence of normalized absorption intensity of pre-edge peak or pre-shoulder in the metal K-edge for several samples (i.e. A2 peak in Sc₂O₃, A2 peak in TiO₂, A1 peak in VO₂, A1 peak in Cr₂O₃, S1 in Mn₂O₃ and S1 in MnO). Pre-edge peak intensity of A2 in TiO₂ at lower temperature (<300 K) is from Hiratoko et al. (2013).

The temperature dependence of transition to each orbital is different. Temperature dependence is not observed in the pre-edge peak for 1s→e_g transition. The temperature dependence is permitted only in the pre-edge

peaks assigned to the $1s \rightarrow t_{2g}$ transition. Pre-edge intensity is mainly due to the electric dipole-transition which is the dominant effect of an interaction of an electron in an atom with the electromagnetic field, and corresponds to the A3 peak in XANES spectra of rutile (Yamamoto 2008). A3 peak has no temperature dependence. A large temperature dependence occurs in the mixture of the quadrupole and dipole transitions which corresponds to the A2 peak in XANES spectra of rutile (Yamamoto 2008). Quadrupole is part of a multipole expansion. The hybridizations of 3d orbital with p orbital between cation and oxygen are important in each compound. Hiratoko et al. (2013) succeeded in the quantitative study of temperature dependence of pre-edge peaks intensity in various titanium compounds. There were two kinds of temperature dependence in pre-edge peaks that are assigned to a mixture of the quadrupole and dipole transitions (rutile- and anatase-type). The gradient of the A2 peak intensity for TiO_2 rutile is similar to the gradient of A1 in VO_2 tetragonal phase and A2 in Sc_2O_3 . There is a possibility that high pre-edge peaks with a large gradient in Sc_2O_3 and VO_2 are composed of the same transitions in TiO_2 rutile. The transition is a mixture of the quadrupole and dipole transitions.

Table 7.1. Slope and energy of peak intensity for the A pre-edge and D difference peaks in each compound.

compounds	Peak label	Energy (eV)	Slope of peak intensity for A or D peak (intensity/100K)	Number of 3d electrons
Sc ₂ O ₃	A2 and D1	4491.97 (1)	0.0048 (3)	0
	A2	4969.27 (1)	0.0063 (3)	
TiO ₂ rutile	D1	4968.47 (1)	0.0074 (3)	0
	D2	4970.87 (1)	0.0035 (3)	
TiO ₂ anatase	A2	4969.65 (1)	0.0016 (3)	0
	D1	4967.85 (1)	0.0067 (3)	
	D2	4970.85 (1)	0.0025 (3)	
VO ₂ tetragonal	A1	5467.05 (1)	0.0069 (3)	1
	D1	5466.68 (1)	0.0071 (3)	
VO ₂ monoclinic	A1	5467.05 (1)	0.0015 (3)	1
	D1	5466.31 (1)	0.0015 (3)	
	A1	5989.53 (1)	0.0016 (3)	
Cr ₂ O ₃	D1	5989.08 (1)	0.0018 (3)	3
	D2	5991.32 (1)	0.0017 (3)	
Mn ₂ O ₃	S1 and D1	6537.99 (1)	0.0014 (3)	4
MnO	S1 and D2	6537.99 (1)	0.0017 (3)	5

7.3.2.2. Temperature gradient for D peaks in different spectra and deformation vibration.

It is known that the pre-edge peak intensity usually increases linearly with increasing temperature by harmonic thermal vibration (Hiratoko et al., 2013). On the other hand, the negative peaks in the difference spectra were identified and observed only in the Ti and Zr K-edges for para- and ferro-electric PbZrO₃, PbTiO₃ and BaTiO₃ (Balzarottie et al., 1980; Miyanaga et al., 2002; Ravel and Stern, 1995; Sato et al., 2005; Sicron et al., 1994; Yoshiasa et al., 2016). The decrease of pre-edge peak intensity is due to the shift from the off-center position of the Ti and Zr atom in the oxygen octahedron. Deformation vibration (bending mode) in thermal

vibration also affects the temperature dependence of peak intensity. The correlation between the pre-edge peak intensity and the mean square relative Displacement (MSRD) would not be observed because the MSRD of EXAFS Debye-Waller factor influences mainly stretching vibration.

Many materials have been studied using pre-edge peaks in XANES (Farges et al., 1996a, b, c; Briges et al., 2000; Miyanaga et al., 2002; Sato et al., 2005; Yamamoto, 2008; Hiratoko et al., 2013). The temperature gradients for A2 peak in XANES spectra of anatase and rutile are 0.0016 (3) (intensity/100K) and 0.0063 (3) (intensity/100K), respectively. The correct slope of each D peak is shown in table 7.1. The temperature gradients for D1 peak in anatase and rutile are 0.0067 and 0.0074 (intensity/100K), respectively. It is important to show that the D1 transition with the large temperature dependence exist in anatase. The peak top position for pre-edge peaks in XANES does not always represent the true energy for independent transition to orbital because several transitions to orbitals overlapped with similar energies. The D peak energy position which is determined by the difference spectra represents one of the true energies for the transition to independent orbital. The temperature dependence of the pre-edge peak intensity depends not only on the characteristics of the electron orbital but also on the difference in overlapping of the electron orbitals.

Chapter 8
General Conclusions

In this Ph.D thesis, local structural analyses for Ti and Zr in meteorite related materials were performed. High temperature laser heating and gas flow experiments on zircon were also performed to observe structural changes at high temperature.

Threshold energy in XANES spectra are affected by valence state of target atoms (Okudera et al., 2012; Wang et al., 2013). Okube et al. (2005) and Yoshiasa et al. (2009) showed that threshold shift in Zr XANES spectra are estimated to occur at high temperature or high pressure. The threshold energy of Zr XANES spectrum in K-Pg sediments is lower than that in volcanic glasses which formed in normal oxidation conditions. Therefore, local structures of Zr in K-Pg sediments are estimated to be formed under high temperature, high pressure and lower oxidation conditions. Local structures of Zr in K-Pg sediments is similar to glass-type local structures. The local structures of Zr in K-Pg sediments did not reveal influence of diagenesis or weathering. Thus, the local structures of Zr in K-Pg sediments maintain the glass environment and the formation conditions of meteorite impact. The local structure analysis of Zr may become a key factor for checking the possibility of the meteorite impact in sedimentary rock at the time of mass extinction. However, abundance of Zr in sediments is not always sufficient to obtain reliable information about the local structures of Zr. The higher Clarke of titanium makes it a more likely marker in sedimentary rocks. Local structures of Ti in K-Pg sediments are similar to those in impact glass and tektite. Therefore, local structures of Ti in K-Pg sediments also maintain a record of the glass structure which was formed by meteorite impact. Consequently, the local structure analysis of Ti may also become a key factor to evaluate meteorite impact events. As reference, local structure analysis of Ti in D-C boundary sediments were performed, which turned out to be similar to those in anatase and obsidian. This similarity indicates that initial obsidian-like local structures was devitrified to anatase-like local structures by diagenesis and weathering. Since the local structures of Zr are not changed by weathering and diagenesis, combination of the information about the coordination environments of Ti and Zr allows a higher reliability for the

estimation of meteorite impact event.

Comparison of local structure analyses of Ca, Ti and Fe between Martian meteorite of Tissint and other meteorites revealed that local structures of each atom in the fusion crust part have common glass-like local structures. The shoulder intensity of Ca XANES spectra have positive correlation with Si content (Neuville et al., 2004). Since shoulder intensity of Ca XANES spectra in fusion crust is clearly lower than in the other glasses, vaporization of SiO₂ component is confirmed in fusion crust during the passage through the atmosphere. Threshold energies of Fe XANES spectra in fusion crusts are lower than those in volcanic glasses which were formed on the surface of Earth, and are higher than those in tektites which were formed at the space (Wang et al., 2013b). Therefore, fusion crust is estimated to be formed under high altitude of atmosphere. Local structures of Ti in fusion crust have common structure with those in tektites; however, pre-edge features and first main peak intensity differ from those of each meteorite fusion crust. This slight difference may come from the size of meteorite and angle of entry in the atmosphere. The local structures of Zr in fusion crust of Tissint meteorite are similar to those in tektite and suevite, those in fusion crust of Tissint have glass-like local structures, whereas, local structures of Zr in inner glass part of Tissint is similar to baddeleyite and fulgurite. Based on the formation temperature of fulgurite (Saikia et al., 2008) and on the ZrO₂-SiO₂ phase diagram (Butterman and Foster, 1967), formation temperature of the inner glass part of Tissint is estimated to be in the range 1680-2000 °C. This result is consistent with the formation temperature of Tissint (~2000°C) proposed by Baziotis et al. (2013). Inner glass part of Tissint is estimated to be formed by large meteorite impact on Mars. Fusion crust of Tissint was formed during the passage through the atmosphere, when baddeleyite-like part vitrified. Comparison between inner glass part and fusion crust part of meteorite gives clues for estimation of the condition of meteorite impact on Mars and passage of meteorite through the atmosphere.

In order to confirm structural changes of Zr at high temperature, heating experiments of zircon were performed by gas flow and laser

heating. During heating, powder X-ray diffraction experiments were performed for ZrSiO_4 and ZrO_2 to confirm their structure changes. Before phase transition of ZrO_2 from tetragonal to cubic, precursor phenomena were observed above 2200 °C. Chemical composition analyses by SEM for quenched sample confirmed that evaporation of the SiO_2 component was by the occurrence of SiO_2 rich region around the rim close to the surface of the sample at temperatures above 2230 °C. We succeeded to redraw the ZrO_2 - SiO_2 phase diagram, based on SEM analyses. Local structure analyses of Zr in zircon quenched from high temperatures show main peak shift to lower energy side in ZrO_2 at higher temperature.

As shown in chapter 4 and 5, pre-edge features of Ti XANES spectra provide information about the formation conditions of natural glasses. In order to confirm the structural changes in XANES spectrum, middle temperature (room temperature to 800K) XAFS experiments were performed. The XANES spectra can be investigated by using the absorption intensity invariant point (AIIP) normalization. The energy position of the difference peak, D-peak, is obtained from the difference spectrum between the low- and high- temperature XANES spectra. There are two kinds of temperature dependence of pre-edge peak intensity (rutile and anatase types). The true temperature dependence of transition to each orbit is obtained from the difference spectrum. The D-peak energy position determined by the difference spectrum represents one of the true energies for the transition to independent orbital. Based on middle temperature XAFS experiment in 3d transition-metal oxide compounds, investigation of pre-edge intensity can provide detailed structure information such as the thermal vibration.

The local structure changes in Zr and Ti are observed by XAFS method in natural meteorite related glasses. Local structures obtained by high accuracy XAFS analyses of transition metal elements in sedimentary rocks, glass phase in meteorites and meteorite impact related glasses, may provide information about the formation conditions. In the future, we will consider the local structure difference of Zr and Ti between fusion crust and inner part of other meteorites from Mars and the moon.

Reference

- Alvarez, L.W., Alvarez, W., Asaro, F. and Michel, H.V. (1980), Extraterrestrial cause for Cretaceous- Tertiary extinction, *Science* 208, 1095-1108.
- Amelin, Y.V. (1998), Geochronology of the Jack Hills detrital zircons by precise U-Pb isotope dilution analysis of crystal fragments, *Chemical Geology*, 146, 25-38.
- Amelin, Y., Lee, D. C., Halliday, A. N. and Pidgeon, R. T. (1999), Nature of the Earth's earliest crust from hafnium isotopes in single detrital zircons, *Nature*, 399, 252-255.
- Artemieva, N., Pierazzo, E. and Stöffler, D. (2002), Numerical modeling of tektite origin in oblique impacts: Implication to Ries-Moldavites strewn field, *Bulletin of Czech Geological Survey*, 77, 303-311.
- Balta, J.B., Sanborn, M., McSween H.Y.J. and Wadhwa, M. (2013), Magmatic history and parental melt composition of olivine-phyric shergottite LAR 06319: Importance of magmatic degassing and olivine antecrysts in Martian magmatism, *Meteoritics and Planetary Science*, 48, 1359-1382.
- Balta, J.B., Sanborn, M., Udry, A., Wadhwa, M. and McSween H.Y.J. (2015), Petrology and trace element geochemistry of Tissint, the newest shergottite fall, *Meteoritics and Planetary Science*, 50, 63-85.
- Balzarottie, A., Comin, F., Incoccia, L., Piacentini, M., Mobilio S. and Savioa, A. (1980), K-edge absorption of titanium in the perovskites SrTiO₃, BaTiO₃ and TiO₂, *Solid State Communications*, 35, 145-149.
- Bart, J.C.J. (1986), Near-Edge X-Ray Absorption Spectroscopy in Catalysis, *Advances in Catalysis*, 34, 203.
- Barnes, V.E. and Barnes, M.A. (1973), *Tektites*. Stroudsburg: Dowden, Hutchison, and Ross Inc. 445p.
- Baziotis, I.P., Liu, Y., DeCarli, P.S., Melosh, H.J., McSween, H.Y., Bodnar, R.J. and Taylo, L.A. (2013), The Tissint Martian meteorite as evidence for the largest impact excavation, *Nature Communications*, 4, 1404.
- Becker R.H. and Pepin, R.O. (1984), The case for a martian origin of the

shergottites: nitrogen and noble gases in EETA 79001, *Earth and Planetary Science Letters*, 69, 225-242.

Belza, J., Goderis, S., Smit, J., Vanhaecke, F., Baert, K., Terryn, H. and Claeys, P. (2015), High spatial resolution geochemistry and textural characteristics of 'microtektite' glass spherules in proximal Cretaceous–Paleogene sections: Insights into glass alteration patterns and precursor melt lithologies, *Geochimica et Cosmochimica Acta*, 152, 1-38.

Belza, J., Goderis, S., Montanari, A., Vanhaecke, F. and Claeys, P. (2017), Petrography and geochemistry of distal spherules from the K-Pg boundary in the Umbria-Marche region (Italy) and their origin as fractional condensates and melts in the Chicxulub impact plume, *Geochimica et Cosmochimica Acta*, 202, 231-263.

Beran, A. and Koeberl, C. (1997), Water in tektites and impact glass by Fourier-transformed infrared spectrometry, *Meteoritics and Planetary Sciences*, 32, 211-216.

Bianconi, A. (1982), Multiplet splitting of final-state configurations in x-ray-absorption spectrum of metal VO₂: Effect of core-hole-screening, electron correlation, and metal-insulator transition, *Physical Review B*, 26, 2741.

Bigham, J.M., Carlson, L. and Murad, E. (1994), Schwertmannite, a new iron oxyhydroxy-sulphate from Pyhasalmi, Finland, and other localities, *Mineralogical Magazine*, 58, 641-648.

Blum J.D., Chamberlain, C.P., Hingston, M.P., Koeberl, C., Marin, L.E., Schuraytz, B.C. and Sharpton, V.L. (1993), Isotopic comparison of K/T boundary impact glass with melt rock from the Chicxulub and Manson impact structures, *Nature*, 325-327.

Boctor N.Z., Meyer, H.O.A. and Kullerud, G. (1976), Lafayette meteorite: Petrology and opaque mineralogy. *Earth and Planetary Science Letters*, 32, 6.

Bogard, D.D., Nyquist, L.E. and Johnson, P. (1984), Noble gas contents of shergottites and implications for the Martian origin of SNC meteorites, *Geochimica et Cosmochimica*, 48, 1732-1739.

Bogard, D., Hörz, F. and Stöffler, D. (1988), Loss of radiogenic argon

- from shocked granitic clasts in suevite deposits from the Ries Crater, *Geochimica et Cosmochimica Acta*, 52, 2639-2649.
- Bohor, B.F., Morreski, P.J., Ford, E.E. (1987), Shocked Quartz in the Cretaceous-Tertiary Boundary clays: Evidence for a Global Distribution, *Science*, 236, 705-709.
- Bridges, F., Booth, C. H., Kwei, G. H., Neumeier J. J. and Sawatzky, G. A. (2000), Temperature dependent changes of the Mn 3*d* and 4*p* nads near T_c in colossal magnetoresistance systems: XANES study of $La_{1-x}Ca_xMnO_3$, *Physical Review B*, 61, 9237.
- Bohor, B.F., Ford, E.E., Modreski, P.J. and Triplehorn, D.M. (1984), Mineralogic Evidence for an Impact Event at the Cretaceous-Tertiary Boundary, *Science*, 224, 867-869.
- Bondar', V.V., Lopatin, S.I. and Stolyarova, V.L. (2005), High-Temperature Thermodynamic Properties of the Al_2O_3 - SiO_2 System, *Inorganic Materials*, 41, 434-441.
- Bouvier, P., Godlewski, J. and Lucazeau, G. (2002), A Raman study of the nanocrystallite size effect on the pressure-temperature phase diagram of zirconia grown by zirconium-based alloys oxidation, *Journal of Nuclear Materials*, 300, 118-126.
- Bowring, S.A. and Williams, I.S. (1999), Priscoan (4.00-4.03) orthogneisses from northwestern Canada, *Contribution to Mineralogy and Petrology*, 134, 3-16.
- Boysen, H. and Frey, F. (1991), Neutron Powder Investigation of the Tetragonal to Monoclinic Phase Transformation in Undoped Zirconia, *Acta Crystallographyca*, B47, 881-886.
- Bralower, T.J., Paull, CK. and Leckie, R.M. (1998), The Cretaceous-Tertiary boundary cocktail: Chicxulub impact triggers margin collapse and extensive sediment gravity flows, *Geology*, 26, 331-334.
- Brett, R. (1967), Metallic spherules in impactite and tektite glasses, *The American Mineralogist*, 52, 721-733.
- Butterman, W.C. and Foster, W.R. (1967), Zircon stability and the ZrO_2 - SiO_2 phase diagram, *American Mineralogist*, 52, 880-885.
- Chao, E.C.T. (1993), Comparison of the Cretaceous-Tertiary boundary

impact events and the 0.77-Ma Australian tektite event; relevance to mass extinction, U.S. Geological Survey Bulletin, 2050.

Claeys, P., Casier, J. and Margolis, S.V. (1992), Microtektites and mass extinctions: Evidence for a late devonian asteroid impact, *Science*, 257, 1102-1104.

Claoué-Long, J.C., Jones, P.J. and Roberts, J. (1992), The age of the Devonian-Carboniferous boundary, *Annales de la Société géologique de Belgique*, 115, 531-549.

Compston, W. and Pidgeon, R. T. (1986), Jack Hills, evidence of more very old detrital zircons in Western Australia, *Nature*, 321, 766-769.

Curtis, C.E. and Sowman, H.G. (1953), Investigation of the Thermal Dissociation, Reassociation and Synthesis of Zircon, *Journal of The American Ceramic Society*, 36, 190-198.

Dalrymple G.B. and Ryder, G. (1993), $^{40}\text{Ar}/^{39}\text{Ar}$ age spectra of Apollo 15 impact melt rocks by laser step- heating and their bearing on the history of lunar basin formation, *Journal of Geophysical Research*, 98, 13085-13095.

Dickin, A.P. and Jones, N.W. (1983), Isotopic evidence for the age and origin of pitchstones and felsites, Isle of Eigg, NW Scotland, *Journal of the Geological Society*, 140, 691-700.

Drits, V.A., Lindgreen, H., Sakharov, B.A., Jakobsen, H.J. and Zviagina, B.B. (2004), The detailed structure and origin of clay minerals at the Cretaceous/Tertiary boundary, Stevns Klint (Denmark), *Clay Minerals*, 39, 367-390.

Durmeyer, O., Beaurepaire, E., Kappler, J. P., Brouder, Ch. and Baudelet, F. (2010), TiK XANES in superconducting LiTi_2O_4 and related compounds, *Journal of Physics: Condensed Matter*, 22, 125504.

Durmeyer, O., Kappler, J. P., Beaurepaire, E., Heintz, J. M. and Drillon, M. J. (1990), Temperature dependence of the pre-edge structure in the Ti K-edge x-ray absorption spectrum of rutile, *Journal of Physics Condensed Matter*, 2, 6127-6136.

Elizabeth, A.C., Hargreaves, M.D., Kee, Matthew T., Pasek, P.A. and Edwards, H.G.M. (2010), Raman spectroscopic study of a fulgurite,

Philosophical Transactions of the Royal Society, 368, 3087-3097.

Elkins-tanton, L.T., Aussillous, P., Bico, J., Quere, D. and Bush, J.W.M. (2003), A laboratory model of splash-form tektites, *Meteoritics and Planetary Science*, 38, 1331-1340.

Engelhardt, V.W. (1997), Suevite breccia of the Ries impact crater, Germany: Petrography, chemistry and shock metamorphism of crystalline rock clasts, *Meteoritics and Planetary Science*, 32, 545-554.

Engelhardt, V.W., Luft, E., Arndt, J., Schock, H. and Weiskirchner, W. (1987), Origin of moldavite, *Geochimica et Cosmochimica Acta*, 51, 1425-1433.

El Goresy, A., Chen, M., Gillet, P., Dubrovinsky, L., Graup, G. and Ahuja, R. (2001), A natural shock-induced dense polymorph of rutile with α -PbO₂ structure in the suevite from the Ries crater in Germany, *Earth and Planetary Science Letters*, 192, 485-495.

El Goresy, A., Wopenka, B., Chen, M. and Kurat, G. (1997), The SAGA of maskelynite in Shergotty, *Meteoritics and Planetary Science*, 32, 1.

Farges, F., Brown, G.E., and Rehr, J.J. (1996a), Coordination chemistry of Ti (IV) in silicate glasses and melts: I. XAFS study of titanium coordination in oxide model compounds, *Geochimica et Cosmochimica Acta*, 60, 3023-3038.

Farges, F., Brown, G.E., Navrotsky, A., Gan, H., and Rehr, J.J. (1996b), Coordination chemistry of Ti (IV) in silicate glasses and melts: II, Glasses at ambient temperature and pressure, *Geochimica et Cosmochimica Acta*, 60, 3039-3053.

Farges, F., Brown, G.E., Navrotsky, A., Gan, H., and Rehr, J.J. (1996c), Coordination chemistry of Ti (IV) in silicate glasses and melts: III. Glasses and melts from ambient to high temperatures. *Geochimica et Cosmochimica Acta* 60, 3055-3065.

Farges, F., Brown, G.E. (1997), Coordination chemistry of titanium (IV) in silicate glasses and melts: IV. XANES studies of synthetic and natural volcanic glasses and tektites at ambient temperature and pressure, *Geochimica et Cosmochimica Acta*, 61, 1863-1870.

Fink, J.H. (1983), Structure and emplacement of a rhyolitic obsidian flow:

Little Glass Mountain, Medicine Lake Highland, northern California (USA), *Geological Society of America Bulletin*, 94, 362-380.

Floran, R.J., Prinz, M., Hlava, R.F., Keil, K., Nehru, C.E. and Hinthorne, J.R. (1978), The Chassigny meteorite: a cumulate dunite with hydrous amphibole-bearing melt inclusions, *Geochimica et Cosmochimica Acta*, 42, 1213-1229.

Fortey, R. (1999), *Life: A Natural History of the First Four Billion Years of Life on Earth*. Vintage, 238–260. Froude, D.O., Ireland, T.R., Kinny, P.D., Williams, I.S., Compston, W., Williams, I. R. and Myers, J. S. (1983), Ion microprobe identification of $4,100 \pm 4,200$ Myr-old terrestrial zircons, *Nature*, 304, 616-618.

Friedman, I., Smith, R.L. and Long, W.D. (1966), Hydration of Natural Glass and Formation of Perlite, *Geological Society of America Bulletin*, 77, 323-328.

Gao, C., Liu, Y., Zong, K., Hu, Z. and Gao, S. (2010), Microgeochemistry of rutile and zircon in eclogites from the CCSD main hole: Implication for the fluid activity and thermo-history of the UHP metamorphism. *Lithos*, 115, 51-64.

Galoisy, L. and Calas, G. (1993), Structural environment of nickel in silicate glass/melt systems: Part 1. Spectroscopic determination of coordination states, *Geochimica et Cosmochimica Acta*, 57, 3613-3626.

Genge, M.J. and Grady, M.M. (1999), The fusion crusts of stony meteorite: Implications for the atmospheric reprocessing of extraterrestrial materials, *Meteoritics and Planetary Science*, 34, 341-356.

Genge, M.J. (2006), Igneous rims on micrometeorites, *Geochimica et Cosmochimica Acta*, 70, 2603-2621.

Glass, B.P. (1984), Tektites, *Journal of Non-Crystalline Solids*, 67, 333-344.

Glass, B.P. (1990), Tektites and Microtektites: key facts and inference, *Tectonophysics*, 171, 393-404.

Giuli, G., Paris, E., Pratesi, G., Koeberl, C. and Cipriani, C. (2003), Iron oxidation state in the Fe-rich layer and silica matrix of Libyan Desert Glass: A high-resolution XANES study, *Meteoritics and Planetary Science*,

38, 1181-1186.

Gilmour, I. and Anders, B.B. (1989), Cretaceous–Paleogene boundary event: Evidence for a short time scale, *Geochimica et Cosmochimica Acta*, 53, 503-511.

Greggor, R.B., Sandstrom, D.R., Wong, J. and Schultz, P., (1983), Investigation of TiO₂-SiO₂ glasses by X-ray absorption spectroscopy, *Journal of non-crystalline solids*, 55, 27-43.

Grimm, R.E. and McSween, H.Y.J. (1982), Numerical simulation of crystal fractionation in shergottite meteorites, *Journal of Geophysical Research*, 87, 385-392.

Groot, F. M., Grioni, M., Fuggle, J. C., Ghijsen, J., Sawatzky, G. A. and Petersen, H. (1989), Oxygen 1s x-ray-absorption edges of transition-metal oxides, *Physical Review B*, 40, 5715.

Grunes, L. A. (1983), Study of the K-edge of 3d transition metals in pure and oxide form by x-ray-absorption spectroscopy, *Physical Review B*, 27, 2111.

Gupta, M., Freeman, A. J. and Ellis, D. E. (1977), Electronic structure and lattice instability of metallic VO₂, *Physical Review B*, 24, 4406.

Guenter, J.R. and Jameson, G.B. (1984), Orthorhombic barium orthotitanate, α' -Ba₂TiO₄, *Acta Crystallographica*, C40, 207-210.

Guili, G., Paris, E., Pratesi, G., Koeberl, C. and Cipriani, C. (2003), Iron oxidation state in the Fe-rich layer and silica matrix of Libyan Desert Glass: A high-resolution XANES study, *Meteoritics and Planetary Science*, 38, 1181–1186.

Guili, G., Eeckhout, S.G., Koeberl, C., Pratesi, G. and Paris, E. (2008), Yellow impact glass from the K/T boundary at Beloc (Haiti): XANES determination of Fe oxidation state and implications for conditions, *Meteoritics & Planetary Science*, 43, 981-986.

Guili, G., Eeckhout, S.G., Paris, E., Koeberl, C. and Pratesi, G. (2005), Iron oxidation state in impact glass from the K/T boundary at Beloc, Haiti, by high-resolution XANES spectroscopy, *Meteoritics and Planetary Science*, 40, 1575-1580.

Harvey, R.P. and McSween, H.Y.J. (1996), A possible high-temperature

origin for the carbonates in the martian meteorite ALH84001, *Nature*, 382, 49-51.

Hashimoto, T., Yoshiasa, A., Okube, M., Okudera, H. and Nakatsuka, A. (2007), Temperature dependence of XANES spectra for ATiO_3 , A_2TiO_4 and TiO_2 compounds with structural phase transitions, *AIP Conference Proceedings*, 882, 428–430.

Head, J. N., Melosh, H. J. and Ivanov, B. A. (2002), Martian meteorite launch: high-speed ejecta from small craters, *Science*, 298, 1752–1756.

Hildebrand, A.R., Penfield, G.T., Kring, D.A., Pilkington, M., Camargo, A.Z., Jacobsen, S.B. and Boynton, W.V. (1991), Chicxulub Crater: A possible Cretaceous/Tertiary boundary impact crater on the Yucatán Peninsula, Mexico, *Geology*, 19, 867-871.

Hiratoko, T., Yoshiasa, A., Nakatani, T., Okube, M., Nakatsuka, A. and Sugiyama, K. (2013), Temperature dependence of pre-edge features in Ti K-edge spectra for ATiO_3 (A =Ca and Sr), A_2TiO_4 (A= Mg and Fe), TiO_2 rutile and TiO_2 anatase, *Journal of Synchrotron Radiation*, 20, 641- 643.

Hoppe, R. (1970), The Coordination Number – an “Inorganic Chameleon”. *Angewandte Chemie International Edition* 9: 25-34.

Hoppe, R. (1979), Effective coordination numbers (ECoN) and mean fictive ionic radii (MEFIR). *Zeitschrift für Kristallographie - Crystalline Materials*, 150, 23-52.

Howard, K.T. (2011), Volatile enhanced dispersal of high velocity impact melts and the origin of tektites, *Proceedings of Geologists’ Association*, 122, 363-382.

Igawa, N. and Ishii, Y. (2001), Crystal Structure of Metastable Tetragonal Zirconia up to 1473 K, *Journal of the American Ceramic Society*, 84, 1169-1171.

Irving, A. J., Kuehner S.M., Tanaka, R., Herd, C.D.K., Chen, G., and Lapen, T.J. (2012), The Tissint depleted permafic olivine-phyric shergottite: petrologic, elemental and isotopic characterization of a recent martian fall in Morocco. 43rd LPSC.

Ishii, T. (1992), Note on the K extended X-ray absorption fine-structure Debye-Waller factor, *Journal of Physics: Condensed Matter*, 4, 8029-8034.

- Izett, G.A. (1991), Tektites in Cretaceous-Tertiary boundary rocks on Haiti and their bearing on the Alvarez impact extinction hypothesis, *Journal of Geophysical Research*, 96, 20879-20905.
- Izumi, F., Asano, H., Murata, N. and Watanabe, N. (1987), Rietveld analysis of powder patterns obtained by TOF neutron diffraction using cold neutron sources, *Journal of Applied Crystallography*, 20, 416-418.
- Jones, T.S., Kimura, S. and Muan, A. (1967), Phase Relations in the System FeO-Fe₂O₃-ZrO₂-SiO₂, *Journal of The American Ceramic Society*, 50, 137-142.
- Kaiser, A., Lobert, M. and Telle, R. (2008), Thermal stability of zircon, *Journal of the European Ceramic Society*, 28, 2199-2211.
- Kawai, J. (2000), Absorption Techniques in X-ray Spectrometry, *Encyclopedia of Analytical Chemistry*, R.A. Meyers (Ed.) 13288-13315.
- Kimura, M., Chen, M., Yoshida, Y., El Goresy, A. and Ohtani, E. (2003), Back-transformation of high-pressure phases in a shock melt vein of an H-chondrite during atmospheric passage: Implications for the survival of high-pressure phases after decomposition, *Earth and Planetary Science*, 217, 141-150.
- Kober, B., Pidgeon, R. T. and Lippolt, H. J. (1989), Single-zircon dating by step-wise Pb-evaporation constrains the Archean history of detrital zircons from the Jack Hills, Western Australia, *Earth and Planetary Science Letters*, 91, 286-296.
- Koeberl, C. (1992), Water content of glasses from the K/T boundary, Haiti: Indicative of impact origin, *Geochimica Cosmochimica Acta*, 56, 4329-4332.
- Koeberl, C. and Sigurdsson, H. (1992), Geochemistry of impact glasses from the K/T boundary in Haiti: Relation to smectites, and a new type of glass, *Geochimica Cosmochimica Acta*, 56, 2113-2129.
- Koeberl, C., Sharpton V.L., Schuraytz, B.C., Shirey, S.B., Blum, J.D. and Marin, L.E. (1994), Evidence for a meteoritic component in impact melt rock from the Chicxulub structure, *Geochimica Cosmochimica Acta*, 58, 1679-1684.
- Kohara, S. and Suzuya, K. (2001), High-Energy X-ray Diffraction of

Disordered Materials in High-Energy X-ray Diffraction Beamline BL04B2 at SPring-8, The Japanese Society for Synchrotron Radiation Research, 14, 365-375, in Japanese.

Kohara, S., Itou, M., Suzuya, K., Imamura, Y., Sakurai, Y., Ohishi, Y. and Takata, M. (2007), Structural studies of disordered materials using high-energy x-ray diffraction from ambient to extreme conditions, *Journal of Physics: Condensed Matter*, 19, 50.

Komatsu, T., Takashima, R., Naruse, H., Phuong, T.H., Dang, T.H., Nguyen, D.P., Dinh, C.T., Ho, T.C., Tran, T.V., Kato, S. and Maekawa, T. (2012a), Devonian-Carboniferous transition in the Pho Han Formation on Cat Ba Island, northeastern Vietnam, *Journal of the Geological Society of Japan*, 118, V-VI.

Komatsu, T., Takashima, R., Phuong, T.H., Dang, T.H., Nguyen, D.P., Nguyen, H.H., Kato, S., Hirata, K. and Maekawa, T. (2012b), Devonian to Carboniferous transitional beds on Cat Ba Island, northeastern Vietnam—a preliminary assessment, *Acta Geoscientica Sinica supplement*, 1, 33-38.

Komatsu, T., Kato, S., Hirata, K., Takashima, R., Ogata, Y., Oba, M., Naruse, H., Ta, H.P., Nguyen, D.P., Dang, T.H., Doan, N.T., Nguyen, H.H., Sakata, S., Kaiho, K. and Konigshof, P. (2014), Devonian-Carboniferous transition a Hangenberg Black Shale equivalent in the Pho Han Formation on Cat Ba Island, Northeastern Vietnam, *Palaeogeography, Palaeoclimatology, Palaeoecology*, 404, 30-43.

Kounaves, S.P., Carrier, B.L., O'Neil, G.D., Stroble, S.T. and Claire, M.W. (2014), Evidence of martian perchlorate, chlorate, and nitrate in Mars meteorite EETA79001: Implications for oxidants and organics, *Icarus*, 229, 206-213.

Kurokawa, H., Sato, M., Ushioda, M., Matsuyama, T., Moriwaki, R., Dohm, J.M. and Usui, T. (2014), Evolution of water reservoirs on Mars: Constraints from hydrogen isotopes in martian meteorites, *Earth and Planetary Science Letters*, 394, 179-185.

Kring, D.A. and Boynton, W.V. (1991), Altered spherules of impact melt and associated relic glass from the K/T boundary sediments in Haiti, *Geochimica et Cosmochimica Acta*, 55, 1737-1742.

- Kusaba, K., Syono, Y., Kikuchi, M. and Fukuoka, K. (1985), Shock behavior of zircon: phase transition to scheelite structure and decomposition, *Earth and Planetary Science Letters*, 72, 433-439.
- Leger, J., M., Tomaszewski, P., E., Atouf, A., and Pereira, A., S. (1993), Pressure-induced structural phase transitions in zirconia under high pressure, *Physical Review B*, 47, 14075-14083.
- Liu, L. (1979), High pressure phase transformation in baddeleyite and zircon, with geophysical implications, *Earth and Planetary Science Letters*, 44, 390-396.
- Lofgren, G. (1971), Experimentally Produced Devitrification Textures in Natural Rhyolitic Glass, *Geological Society of America Bulletin*, 82, 111-124.
- Longhi, J. and Pan, V. (1987), The parent magmas of the SNC meteorites, *Proceedings of the 19th Lunar and Planetary Science Conference*, 451-464.
- Lytle, F.W. and Gregor, R.B. (1988), Discussion of x-ray-absorption near-edge structure: Application to Cu in the high-Tc superconductors $\text{La}_{1.8}\text{Sr}_{0.2}\text{CuO}_4$ and YBa_2CuO_7 , *Physical Review B*, 37, 1550-1562.
- Lytle, F.W., Sayers, D.E. and Stern, E.A. (1989), Report of the International Workshop on Standards and Criteria in X-ray Absorption Spectroscopy, *Physica B*, 158, 701-722.
- Maas, R., Kinny, P.D., Williams, I.S., Froude, D.O. and Compston, W. (1992), The Earth's oldest known crust: A geochronological and geochemical study of 3900-4200 Ma old detrital zircons from Mt. Narryer and Jack Hills, Western Australia, *Geochimica et Cosmochimica Acta*, 56, 1281-1300.
- Maeda, H. (1987), Accurate bond length determination by EXAFS method. *Journal of Physical Society of Japan* 56, 2777-2787.
- Martínez-Ruiz, F., Ortega-Huertas, M., Palomo-Delgado, I. and Smit, J. (2002), K-T boundary spherules from Blake Nose (ODP leg 171B) as a record of the Chicxulub ejecta deposits, *Geological Society of London, special publications* 183, 149-161.
- Manuel, D., Cabaret, D., Brouder, C., Sainctavit, P., Bordage, A. and Trcera, N. (2012), Experimental evidence of thermal fluctuations on the

x-ray absorption near-edge structure at the aluminium K edge, *Physical Review B*, 85, 224108.

Mashimo, T., Nagayama, K. and Sawaoka, A. (1983), Shock Compression of Zirconia ZrO_2 and Zircon $ZrSiO_4$ in the Pressure Range up to 150 GPa, *Physics and Chemistry of Minerals*, 9, 237-247.

McKeown, D.A., Muller, I.S., Buechelle, A.C. and Pegg, I.L. (1999), X-ray absorption studies of the local environment of Zr in high-zirconia borosilicate glasses, *Journal of Non-Crystalline Solids*, 258, 98-109.

McPherson, D., Pye, L.D., Fréchette, V.D. and Tong, S. (1984), Microstructure of natural glasses, *Journal of Non-Crystalline Solids*, 67, 61-79.

McSween Jr, H.Y., Jarosewich, E. (1983), Petrogenesis of the Elephant Moraine A79001 meteorite: Multiple magma pulses in the shergottite parent body, *Geochimica et Cosmochimica Acta*, 47, 1501-1513.

McSween Jr, H.Y., Stolper, E.M., Taylor, L.A., Muntean, R.A., O'Kelley, G.D., Eldridge, J.S., Biswas, S., Ngo, H.T., Lipschutz, M.E. (1979), Petrogenetic relationship between Allan Hills 77005 and other achondrites, *Earth and Planetary Science Letters*, 45, 275-284.

Medkeff, J. and Rundkvist, M. (2008), Fire in the sky, *Skeptic*, 14.3, 65-67.

Melosh, H.J. and Ivanov, B.A. (1999), Impact crater collapse, *annual Review of Earth Planetary Sciences*, 27, 385-415.

Mezouar, M., Faure, P., Crichton, W., Rambert, N., Sitaud, B., Bauchau, S. and Blattmann, G. (2002), Multichannel collimator for structural investigation of liquids and amorphous materials at high pressures and temperatures, *Review of Scientific Instruments* 73, 3570.

Mittlefehldt, D.W., Lindstrom, D.J., Lindstrom, M.M. and Martinez, R.R. (1997), Lithology A in EETA79001-Product of impact melting on Mars (abstr). *Lunar Planetary Science XXVIII*, 961-962.

Miyanaga, T., Diop, D., Ikeda, S. and Kon, H. (2002), Study of the Local Structure Changes in $PbTiO_3$ by Pb L III EXAFS, *Ferroelectrics*, 206, 407.

Miyano, Y., Yoshiasa, A., Tobase, T., Isobe, H., Hongu, H., Okube, M., Nakatsuka, A. and Sugiyama, K. (2016), Weathering and precipitation

after meteorite impact of Ni, Cr, Fe, Ca and Mn in K-Pg boundary clays from Stevns Klint, *Journal of Physics: Conference Series* 712, 012097.

Mountjoy, G., Pickup, D. M., Wallidge, G. W., Holland, M. A., Newport, R. J. and Smith, M. E. (2000), Changes in the Zr environment in zirconia-silica xerogels with composition and treatment as revealed by Zr K-edge XANES and EXAFS, *Physical Chemistry Chemical Physics*, 2, 2455-2460.

Mursic, Z., Vogt, T. and Frey F. (1992), High-Temperature Neutron Powder Diffraction Study of $ZrSiO_4$ up to 1900 K, *Acta Crystallographica*, B48, 584-590.

Myers, J. S. in *Early Precambrian Processes*, 143-154 (Geological Society of London Special Publication No. 95, 1995).

Mysen, B. and Neuville, D. (1995), Effect of temperature and TiO_2 content on the structure of $Na_2Si_2O_5$ - $Na_2Ti_2O_5$ melts and glass, *Geochimica et Cosmochimica Acta*, 59, 325-342.

Neuville, D.R., Cormier, L., Flanck, A.M., Briois, V. and Massiot, D. (2004), Al speciation and Ca environment in calcium aluminosilicate glasses and crystals by Al and Ca K-edge X-ray absorption spectroscopy, *Chemical Geology*, 213, 153-163.

Nespolo, M. and Guillot, B. (2016), CHARDI2015: Charge Distribution analysis of non-molecular structures, *Journal of Applied Crystallography*, 49, 317-321.

Officer, C.B. and Drake, C.L. (1985), Terminal Cretaceous environmental events, *Science*, 227, 1161-1167.

Ohtaka, O., Andraut, D., Bouvier, P., Schultz, E. and Mezouar, M. (2005), Phase relations and equation of state of ZrO_2 to 100 GPa, *Journal of Applied Crystallography*, 38, 727-73.

Ohtaka, O., Fukui, H., Kunisada, T., Fujisawa, T., Funakoshi, K., Utsumi, W., Irifune, T., Kuroda, K. and Kikegawa, T. (2001), Phase relations and equations of state of ZrO_2 under high temperature and high pressure, *Physical Review B*, 63, 174108.

Ohtaka, O., Yamanaka, T., Kume, S., Ito, E. and Navrotsky, A. (1991), Stability of Monoclinic and Orthorhombic Zirconia: Studies by High-Pressure Phase Equilibria and Calorimetry, *Journal of the American*

Ceramic Society, 74, 505-509.

Okube, M., Sasaki, S., Yoshiasa, A., Wang, L., Nakatani, T., Hongu, H., Murai, K., Nakatsuka, A. and Miyawaki, R. (2012), Local structure of Zn in Cretaceous-Tertiary boundary clay from Stevns Klint, *Journal of Mineralogical and Petrological Sciences*, 107, 192-196.

Okube, M., Yoshiasa, A., Yashima, M., Ohuchi, K., Ishimura, T., Numako, C. and Koto, K. (2005), XAFS study of the Perovskite-Type Proton Conductor $\text{SrZr}_{0.9}\text{Yb}_{0.1}\text{O}_{3-\delta}$, *Physica Scripta*, 115, 375-377.

Okudera, H., Yoshiasa, A., Murai, K., Okube, M., Takeda, T. and Kikkawa, S. (2012), Local structure of magnetite and maghemite and chemical shift in Fe K-edge XANES, *Journal of Mineralogical and Petrological Science*, 107, 127-132.

Ondik, H. and McMurdie, H.F. (1998), Editors. *Phase Diagrams for Zirconium + Zirconia Systems*. pp. 35-38. Ohio: The American Ceramic Society.

Osinski, G.R., Grieve, R.A.F. and Spary, J.G. (2004), The nature of the groundmass of surficial suevite from the Ries impact structure, Germany, and constraints on its origin, *Meteoritics and Planetary Science*, 39, 1655-1683.

Pandya, K.I., Koningsberger, D.C. (1991), X-ray Absorption Fine Structure Spectroscopy, *Analysis of Microelectronic Materials and Devices*, eds. M. Grasserbauer, H.W. Werner, Wiley, Chichester, 637-655, 1991.

Paris, E., Dingwell, D.B., Seifert, F.A., Mottana, A. and Romano, C. (1994), Pressure-induced coordination change of Ti in silicate glass: a XANES study, *Physics and Chemistry of Minerals*, 21, 520-525.

Patil, R.N. and Subbrao, E.C. (1969), Axial thermal expansion of ZrO_2 and HfO_2 in the range room temperature to 1400 °C, *Journal of Applied Crystallography*, 2, 281-288.

Pavlik, R.S. and Holland, H.J. (2001), Thermal Decomposition of Zircon Refractories, *Journal of American Ceramic Society*, 84, 2930-2936.

Penn, R.L. and Banfield, J.F. (1999), Formation of rutile nuclei at anatase (112) twin interfaces and the phase transformation mechanism in

nanocrystalline titania, *American Mineralogist*, 84, 871-876.

Pillep, B., Fröba, M., Phillips, M. L. F., Wong, J., Stucky, G.D. and Behrens, P. (1997), XANES spectroscopic study of the electronic structure of Ti in KTiOPO_4 and some of its isomorphous compounds, *Solid State Communication*, 103, 203-207.

Price, N.A., Johnson, S.E., Gerbi, C.C. and West, D.P. (2012), Identifying deformed pseudotachylite and its influence on the strength and evolution of a crustal shear zone at the base of the seismogenic zone, *Tectonophysics*, 518-521, 63-83.

Raup, D. and Sepkoski Jr, J. (1982), Mass extinctions in the marine fossil record, *Science*, 215, 1501–1503.

Rampino, M.R. and Reynolds, R.C. (1983), Clay mineralogy of the Cretaceous-Tertiary boundary clay. *Science* 219: (4584), 495-498.

Sakai, S., Yoshiasa, A., Arima, H., Okube, M., Numako, C. and Sato, T. (2007), XAFS Study of As in KT Boundary Clays, *AIP Conference Proceedings* 882, 274.

Ravel, B. and Stern, E.A. (1995), Local disorder and near edge structure in titanate perovskites, *Physica B*, 208-209, 316-318.

Rehr, J.J., Musture de Lson, J., Zabinsky, S.I. and Ablers, R.C. (1991), Theoretical X-ray absorption fine structure standards, *Journal of the American Chemical Society*, 113, 5135-5140.

Reid, A.F. and Ringwood, A.E. (1969), Newly observed high pressure transformation in Mn_3O_4 , CaAl_2O_4 , and ZrSiO_4 , *Earth and Planetary Science Letters*, 6, 205-208.

Reimold, W.U. (1995), Pseudotachylite in impact structures-generation by friction melting and shock brecciation?: A review and discussion, *Earth Science Reviews*, 39, 247-265.

Reinhart, J.S., (1958), Impact effects and tektites, *Geochimica et Cosmochimica Acta*, 39, 247-265.

Ressler, T., Wienold, J., Jentoft, R., E. and Neisius, T. (2002), Bulk Structural Investigation of the Reduction of MoO_3 with Propene and the Oxidation of MoO_2 with Oxygen, *Journal of Catalysis*, 210, 67-83.

Romanek, C.S., Grady, M.M., Wright, I.P., Mittlefehldt, D.W., Socki, R.A.,

Pillinger, C.T. and Gibson Jr, E.K. (1994), Record of fluid-rock interactions on Mars from the meteorite ALH84001, *Nature*, 372, 655-657.

Ross, C.S. and Smith, R.L. (1955), Water and Other Volatiles in Volcanic Glasses, *American Mineralogist*, 40, 1071-1089.

Saikia, B.J., Parthasarathy, G., Sarmah, N.C. and Burua, G.D. (2008), Fourier-transform infrared spectroscopic characterization of naturally occurring glassy fulgurites. *Bulletin of Material Science*, 31, 2, 155-158.

Sakai, S., Yoshiasa, A., Arima, H., Okube, M., Numako, C. and Sato, T. (2007), XAFS Study of As in KT Boundary Clays. *AIP Conference Proceedings* 882, 274.

Sato, K., Miyanaga, T., Ikeda, S. and Diop, D. (2005), XAFS study of Local Structure Change in Perovskite Titanates, *Physica Scripta*, 115, 359-361.

Schmitz, B. (1992), Chalcophile elements and Ir in continental Cretaceous-Paleogene boundary clays from the western interior of the USA, *Geochimica et Cosmochimica Acta*, 56, 1695-1703.

Sepkoski Jr, J.J. (1996), Patterns of Phanerozoic extinction: a perspective from global data bases. In: Walliser, O.H. (Ed.), *Global Events and Event Stratigraphy in the Phanerozoic*. Springer, Berlin, pp. 35-51.

Shannon R.D. (1976), Revised Effective Ionic Radii and Systematic Studies of Interatomic Distances in Halides and Chalcogenides. *Acta Crystallographica A*32: 751-767. Sharpton V. L., Darlymple, G.B., Martin, L. E., Ryder, G., Schuraytz, B. C. and Urrutia-Fucugauchi, J. (1992), New links between the Chicxulub impact structure and the Cretaceous/Tertiary boundary, *Nature*, 359, 819-821.

Sheffer, A.A., Dyar, M.D. and Sklute, E.C. (2006), Lightning strike glasses as an analog for impact glasses: ^{56}Fe Mössbauer spectroscopy of fulgurite, *Lunar and Planetary Science XXXVII*: 2009.

Sicron, N., Ravel, B., Yacoby, Y., Stern, E. A., Dogan, F. and Rehr, J.J. (1994), Nature of the ferroelectric phase transition in PbTiO_3 , *Physical Review B*, 50, 13168-13180.

Sigurdsson, H., D'Hondt, S., Arthur, M.A., Bralower, T.J., Zachos, J.C.,

- van Fossen, M., Channell, E.T. (1991a), Glass from the Cretaceous/Tertiary boundary in Haiti, *Nature*, 349, 482-487.
- Sigurdsson, H., Bonte, P., Turpin, L., Chaussidon, M., Metrich, N., Steinberg, M., Pradel, P., D'Hondt, S. (1991b), Geochemical constraints on source regions of Cretaceous/Tertiary impact glasses, *Nature*, 353, 839-842.
- Simon, S.B., Papike, J.J. and Beauchamp, R.H. (1986), Shock metamorphism and petrography of the Shergotty achondrite, *Geochimica et Cosmochimica Acta*, 50, 889-903.
- Smit, J., Montanari, A., Swinburne, N.H.M., Alvarez, W., Hildebrand, A.R., Margolis, A.R., Claeys, P., Lowrie, W., Asaro, F. (1992), Tektite-bearing, deep-water clastic unit at the Cretaceous-Tertiary boundary in northeastern Mexico, *Geology*, 20, 99-103.
- Smith, J.V. and Hervig, R.L. (1979), Shergotty meteorite: Mineralogy, petrology and minor elements, *Meteoritics*, 14, 121-142.
- Stähle, V. (1972), Impact glasses from the suevite of the Nördlinger Ries, *Earth and Planetary Science Letters*, 17, 275-293.
- Stauffer, M.R. and Butler, S.L. (2010), The Shapes of Splash-Form Tektites: Their Geometrical Analysis, Classification and Mechanics of Formation, *Earth Moon Planets*, 107, 169-196.
- Stebbins, J.F. and McMillan, P. (1989), Five- and six- coordinated Si in $K_2Si_4O_9$ glass quenched from 1.9 GPa and 1200 °C, *American Mineralogist*, 74, 965-968.
- Stern, E.A., Līvņš, P. and Zhang, Z. (1991), Thermal vibration and melting from a local perspective, *Physical Review B*, 43, 8850-8860.
- Stöffler, D., Ostertag, R., Jammes, C., Pfannschmidt, P., Sen Gupta, P.R., Stöffler, D., Keil, K. and Edward, R. D. S. (1991), Shock metamorphism of ordinary chondrites, *Geochimica et Cosmochimica Acta*, 55, 3845-3867.
- Stolper, E.M. and McSween, H.Y.J. (1979), Petrology and origin of the shergottite meteorites, *Geochimica et Cosmochimica Acta*, 43, 1475-1498.
- Stözer, D. and Wagner, G.A. (1971), Fission track ages of North American tektites, *Earth and Planetary Science Letters*, 10, 435-440.
- Subbarao, E.C., Agrawal, D.K., McKinstry, H.A., Sallese, C.W. and Roy,

- R. (1990), Thermal Expansion of Compounds Zircon Structure, *Journal of American Ceramic Society*, 73, 1246-1252.
- Strong, C.P., Brooks, R.R., Wilson, S.M., Reeves, R.D., Orth, C.J., Mao, X.Y., Quintana, L.R. and Anders, E. (1987), A new Cretaceous–Paleogene boundary site at Flaxbourne River, New Zealand: Biostratigraphy and geochemistry, *Geochimica et Cosmochimica Acta*, 51, 2769-2777.
- Subbarao, E.C., Agrawal, D.K., McKinstry, H.A., Sallese, C.W. and Roy, R. (1990), Thermal Expansion of Compounds Zircon Structure, *Journal of American Ceramic Society*, 73, 1246-1252.
- Swindle, T.D., Caffee, M.W. and Hohenberg, C.M. (1986), Xenon and other noble gases in shergottites, *Geochimica et Cosmochimica Acta*, 50, 1001-1015.
- Swisher, C. C., Grajales-Nishimura, J. M., Montanari, A., Margolis, S. V., Claeys, P., Alvarez, W., Renne, P., Cedillo-Pardo, E., Murrasse, F. J-M. R., Curtis, G. H., Smit, J. and McWilliams, M. O. (1992), Coeval $^{40}\text{Ar}/^{39}\text{Ar}$ Ages of 65.0 Million years ago from Chicxulub Crater Melt Rock and Cretaceous-Tertiary Boundary Tektites, *Science*, 257, 954-958.
- Thaisen, K.G. and Taylor, L.A. (2009), Meteorite fusion crust variability, *Meteoritics and Planetary Science*, 44, 871-878
- Thorpe O.W. and Thorpe, R.S. (1984), The distribution and sources of archaeological pitchstone in Britain, *Journal of Archaeological Science*, 11, 1-34.
- Toppani, A. and Libourel, G. (2003), Factors controlling compositions of cosmic spinels: Application to atmospheric entry conditions of meteoritic materials, *Geochimica et Cosmochimica Acta*, 67, 4621-4638.
- Treiman, A.H. (1989), Complex petrogenesis of the Nakhla (SNC) meteorite: Evidence from petrography and mineral chemistry, *Proceeding of Lunar and Planetary Science Conference*, 20, 273-280.
- Treiman, A.H. (1993), The parent magma of Nakhla (SNC) meteorite, inferred from magmatic inclusions, *Geochimica et Cosmochimica Acta*, 57, 4753-4767.
- Treiman, A.H. (1995), A petrographic history of martian meteorite ALH84001: Two shocks and ancient age, *Meteoritics*, 30, 294-302.

- Treiman, A.H. and Sutton, S.R. (1992) Petrogenesis of the Zagami meteorite: Inferences from synchrotron X-ray (SXRF) microprobe and electron microprobe analyses of pyroxenes, *Geochimica et Cosmochimica Acta*, 56, 4059-4074.
- Tobase, T., Wang, L., Yoshiasa, A., Okube, M., Nakatani, T., Hayasaka, Y. and Isobe H. (2013), XAFS study on Ca local structure in natural glasses and tektite, *Journal of Physics: Conference Series*, 430, 012070
- Tobase, T., Yoshiasa, A., Wang, L., Hiratoko, T., Hongu, H., Okube, M. and Sugiyama, K. (2015a), XAFS study of Zr in Cretaceous-Tertiary boundary clays from Stevns Klint, *Journal of Mineralogical and Petrological Science*, 110, 88-91.
- Tobase, T., Yoshiasa, A., Wang, L., Hongu, H., Isobe, H. and Miyawaki, R. (2015b) XAFS study on the zirconium local structures in tektites and natural glasses. *Journal of Mineralogical and Petrological Sciences*, 110, 1-7.
- Toropov, N.A. and Galakhov, F.Y. (1956), Liquefaction in the System ZrO_2-SiO_2 , *Akademiia nauk SSSR. Izvestiia. Seriiia khimicheskaiia*, 2, 158-161.
- Tsukimura, K. and Nakazawa, H., (1994), Research Proposal of the Materials Formed on the Earth's surface, *Journal of Mineral Society Japan*, 23, 77-81 in Japanese.
- Tuffen, H., James, M.R., Castro, J.M. and Schipper C.I. (2013), Exceptional mobility of an advancing rhyolitic obsidian flow at Cordón Caulle volcano in Chile, *Nature Communications*, 4, 2709.
- Usui, T., Sanborn, M., Wadhwa, M. and McSween, H.Y. (2010), Petrology and trace element geochemistry of Robert Massif 04261 and 04262 meteorites, the first examples of geochemically enriched lherzolitic shergottite, *Geochimica et Cosmochimica Acta*, 74, 7283-7306.
- Usui, T., Alexander, C.M., Wang, J., Simon, J.I. and Jones, J.H. (2012), Origin of water and mantle–crust interactions on Mars inferred from hydrogen isotopes and volatile element abundances of olivine-hosted melt inclusions of primitive shergottites, *Earth and Planetary Science Letters*, 357–358, 119-129.
- Walker, D., Kirkpatrick, R.J., Longhi, J. and Hays, J.F. (1976),

Crystallization history of lunar picritic basalt sample 12002: Phase equilibria and cooling rate studies, *Geological Society of America Bulletin*, 87, 646-656.

Wang, L., Yoshiasa, A., Okube, M. and Takeda, T. (2011), Titanium local structure in tektite probed by X-ray absorption fine spectroscopy, *Journal of Synchrotron Radiation*, 18, 885-890.

Wang, L., Yoshiasa, A., Okube, M., Nakatani, T., Hayasaka, Y., and Isobe, H. (2013a), Local structure of Titanium in natural glasses probed by X-ray absorption fine structure, *Journal of Physics: Conference Series*, 430, 012121.

Wang, L., Yoshiasa, A., Okube, M., Hiratoko, H., Hu, Y., Arima, H. and Sugiyama, K. (2013b), Local structure of iron in tektites and natural glasses: An insight through X-ray absorption fine structure spectroscopy, *Journal of Mineralogical Petrological Science*, 108, 288-294.

Wasson, J. T. and Wetherill, G. W. (1979), Dynamical chemical and isotopic evidence regarding the formation locations of asteroids and meteorites, *Asteroids*, 926-974.

Waychunas, G. A. (1994), Synchrotron radiation XANES spectroscopy of Ti in minerals: Effects of Ti bonding distances, Ti valence, and site geometry on absorption edge structure, *American Mineralogist*, 72, 1987, 89.

Weincke, H.H. (1978), Chemical and mineralogical examination of the Nakhla achondrite, *Meteoritics*, 13, 660-664.

Werthmann, R. and Hoppe, R., (1985), Ein neues einfaches Titanat: KNaTiO_3 , *Zeitschrift für anorganische und allgemeine Chemie*, 523, 54-62.

White, R.V. and Saunders, A.D. (2005), Volcanism, impact and mass extinction: incredible or credible coincidences? *Lithos*, 79, 299-316.

Wiens, R.C., Becker, R.H. and Pepin, R.O. (1986), The case for a martian origin of the shergottites, II. Trapped and indigenous gas components in EETA 79001 glass, *Earth and Planetary Science Letters*, 77, 149-158.

Wilde, S. A. and Pidgeon, R. T. (1990), in 3rd International Archaean Symposium (Perth), *Excursion Guidebook*, 82-95.

Wright, A.C., Desa, J.A.E., Weeks, R.A., Sinclair, R.N. and Bailey, D.K.

- (1984), Neutron diffraction studies of natural glasses, *Journal of Non-Crystalline Solids*, 67, 35-44.
- Wu, K.K. and Brown, I.D. (1973), The crystal structure of α -barium orthotitanate, α -Ba₂TiO₄, and the bond strength-bond length curve of Ti-O, *Acta Crystallographica B*29, 2009-2012.
- Yamamoto, T. (2008), Assignment of pre-edge peaks in K-edge x-ray absorption spectra of 3d transition metal compounds: electric dipole or quadrupole?, *X-ray Spectrometry*, 37, 572-584.
- Yarger, J.L., Diefenbacher, J., Smith, K.H., Wolf, G.H., Poe, B. and McMillan, P.F. (1995), Al³⁺ coordination changes in high pressure aluminosilicate liquids, *Science*, 270, 1964-1967.
- Yashima, M., Kakihana, M. and Yoshimura, M. (1996), Metastable-stable phase diagrams in the zirconia-containing systems utilized in solid-oxide fuel cell application, *Solid State Ionics*, 86-88, 1131-1149.
- Yau, Y.C., Peacor, D.R., Essene, E.J. (1987), Authigenic anatase and titanite in shales from the Salton Sea geo thermal field, *Neues Jahrbuch für Mineralogie, Monatshefte*, 441-452.
- Yoshiasa, A., Koto, K., Maeda, H. and Ishii, T. (1997), The mean-square relative displacement and displacement correlation functions in tetrahedrally and octahedrally coordinated ANB8-N crystals, *Japanese Journal of Applied Physics*, 36, 781-784.
- Yoshiasa, A., Nagai, T., Ohtaka, O., Kamishima, O. and Shimomura, O. (1999), Pressure and temperature dependence of EXAFS Debye-Waller factors in diamond-type and white-tin-type germanium, *Journal of Synchrotron Radiation*, 6, 43-49.
- Yoshiasa, A., Arima, H., Okube, M., Fukui, H., Nakatsuka, A., Katayama, Y. and Ohtaka, O., (2009), High-pressure XAFS study of bulk and nano size ZrO₂ particles, *Journal of Physics: Conference Series*, 190, 012119.

Acknowledgement

I am sincerely grateful for the assistance for everybody supported me. I would like to thank for several reasons.

First of all, I grateful to my supervisor Prof. Dr. Massimo Nespolo (Lorraine University), who gave me advice on theoretical crystallography. He invited me in France and supported all of the research and life in France. I was influenced by his sincere attitude towards research. Without his passionate, precise advise and his help, my Ph.D thesis is never finished.

I would like to express my appreciation for my other supervisor Prof. Dr. Akira Yoshiasa (Kumamoto University), who gave me advice every time and introduced me to local structural science. He gave me a lot of opportunities for scientific experience such as attendance at international conference and study abroad.

I appreciate Prof. Dr. Tadao Nishiyama, Prof. Dr. Toshiaki Hasenaka and Prof. Dr. Hiroshi Isobe (Kumamoto University) for their helpful discussion on my Ph.D. work.

I am grateful to Prof. Dr. Kazumasa Sugiyama, Dr. Maki Okube and Dr. Hiroshi Arima (Tohoku University) for writing paper, experiment in KEK, PF and XRD experiment in Tohoku University.

I am grateful to Dr. Osamu Ohtaka (Osaka University), Dr. Ken-ichi Funakoshi (CROSS) for help at high temperature experiment in SPring-8, critical comment and advice for analysis of XRD experiment. I wish to express my gratitude to Prof. Dr. Masami Kanzaki, Prof. Dr. Xianyu Xue (Okayama University), Dr. Keisuke Hatada (Toyama University) for giving me opportunity to study in their laboratories.

I would like to mention great labmates in Department of Earth Science. Fruitful discussion with members in the department are greatly appericiated. Especially, I wish thank Dr. Tomotaka Nakatani, Dr. Ling Wang, Dr. Tatsuya Hiratoko, Ai Koganemaru, Makoto Tokuda, Satoshi Jinnouchi and Yumiko Miyano. I am also grateful to Hibiki Eguchi, Yousuke Moribe, Hideto Yamasaki, Genki Ishimaru and Ukyo Nishi. They gave motivation for study. I enjoyed wonderful research life thanks to them.

This work was supported by a Research Fellowships of the Japan Society for the Promotion of Science and TOBITATE ryugaku Japan.

I am deeply grateful to my family for their kindness.